



BILINGUAL  
PUBLISHING CO.  
Pioneer of Global Academics Since 1984

# Journal of Atmospheric Science Research

---

Volume 5 • Issue 3 • July 2022 ISSN 2630-5119(Online)



## Editor-in-Chief

**Dr. Qiang Zhang**

Beijing Normal University, China

**Dr. José Francisco Oliveira Júnior**

Federal University of Alagoas (UFAL), Maceió, Alagoas, Brazil

**Dr. Jianhui Bai**

Institute of Atmospheric Physics, Chinese Academy of Sciences, China

## Editorial Board Members

Alexander Kokhanovsky, Germany	Pallav Purohit, Austria
Fan Ping, China	Pardeep Pall, Canada
Svetlana Vasilivna Budnik, Ukraine	Service Opore, Canada
S. M. Robaa, Egypt	Donglian Sun, United States
Daniel Andrade Schuch, Brazil	Jian Peng, United Kingdom
Nicolay Nikolayevich Zavalishin, Russian Federation	Vladislav Vladimirovich Demyanov, Russian Federation
Isidro A. Pérez, Spain	Chuanfeng Zhao, China
Lucille Joanna Borlaza, France	Jingsong Li, China
Che Abd Rahim Bin Mohamed, Malaysia	Suleiman Alsweiss, United States
Mengqian Lu, China	Ranis Nail Ibragimov, United States
Sheikh Nawaz Ali, India	Raj Kamal Singh, United States
ShenMing Fu, China	Lei Zhong, China
Nathaniel Emeka Urama, Nigeria	Chenghai Wang, China
Thi Hien To, Vietnam	Lichuan Wu, Sweden
Prabodha Kumar Pradhan, India	Naveen Shahi, South Africa
Tianxing Wang, China	Hassan Hashemi, Iran
Zhengqiang Li, China	David Onojiede Edokpa, Nigeria
Haider Abbas Khwaja, United States	Maheswaran Rathinasamy, India
Kuang Yu Chang, United States	Zhen Li, United Kingdom
Wen Zhou, China	Anjani Kumar, India
Mohamed El-Amine Slimani, Algeria	Netrananda Sahu, India
Xiaodong Tang, China	Aisulu Tursunova, Kazakhstan
Perihan Kurt-Karakus, Turkey	Hirdan Katarina de Medeiros Costa, Brazil
Anning Huang, China	Masoud Rostami, Germany
Olusegun Folarin Jonah, United States	Barbara Małgorzata Sensuła, Poland

Volume 5 Issue 3 • July 2022 • ISSN 2630-5119 (Online)

# Journal of Atmospheric Science Research

**Editor-in-Chief**

Dr. Qiang Zhang

Dr. José Francisco Oliveira Júnior

Dr. Jianhui Bai



**BILINGUAL  
PUBLISHING CO.**

Pioneer of Global Academics Since 1984



## Contents

### Articles

- 1 Asymmetric Mean Annual Temperature Wavelets Surface Air Layer of Berlin for 1701–2021**  
Peter Mazurkin
- 10 Significant Improvement in Rainfall Forecast over Delhi: Annual and Seasonal Verification**  
Kuldeep Srivastava
- 26 Experimental Simulation of Red Sprites in a Laboratory**  
Victor Tarasenko Nikita Vinogradov Evgenii Baksht Dmitry Sorokin
- 52 To the Question of the Assessment of Ecological Comfort of the Climate**  
Elena S. Andreeva Sergey S. Andreev Anna A. Parshina

### Review

- 37 The Evil Couple: Illegal Mining in Water Bodies and Climate Change: A Case Study of Ghana**  
Victor Adjei Elijah Foh Amaning Isaac Tettey Adjokatse

ARTICLE

# Asymmetric Mean Annual Temperature Wavelets Surface Air Layer of Berlin for 1701–2021

Peter Mazurkin \* 

Volga State University of Technology, Yoshkar-Ola, the Republic of Mari El, Russia

---

ARTICLE INFO

*Article history*

Received: 30 April 2022

Revised: 14 June 2022

Accepted: 20 June 2022

Published: 8 July 2022

---

*Keywords:*

Berlin

Mean annual temperature

1701–2021

Wavelets

Forecast

---

ABSTRACT

The regularities of the dynamics of the average annual temperature of Berlin from 1701 to 2021 are revealed. A total of 65 wavelets were received. The temperature has a high quantum certainty, and the change in the average annual temperature of Berlin was identified by a model that contains only two components for prediction. The basis of the forecast at 320 years makes it possible to look into the future until the year 2340. The forecast confirms the conclusions made in the CMIP5 report on global warming. With an increase in the number of components in the model up to five, the forecast is possible only until 2060. Therefore, the model with only two components is workable. The trend is characterized by a modified Mandelbrot equation showing exponential growth with a high growth rate of 1.47421. The wave equation also has an amplitude in the form of the Mandelbrot law (in mathematics, the Laplace law, in biology, the Zipf-Pearl law, in econometrics, the Pareto law), when the exponential growth activity is equal to 1. For 1701, the period of oscillation was  $2 \times 60.33333 \approx 120.7$  years. By 2021, the period decreased and became equal to 87.6 years. The trend is such that by 2340 the period of oscillation will decrease to 30.2 years. Such an increase in fluctuations indicates an imbalance in climate disturbances in temperature in Berlin. For Berlin, the last three years are characterized by sharp decreases in the average annual temperature from 11.8 °C to 10.5 °C, i.e. by 12.4% in 2021. Therefore, the forecast is still unstable, as a further decrease in the average annual temperature of Berlin in the near future may change the picture of the forecast.

## 1. Introduction

In the 21st century, global average temperatures are very likely to exceed the maximum levels recovered over the past 784,000 years. Based on temperature data from

eight glacial cycles, the results provide an independent validation of current CMIP5 warming projections <sup>[1]</sup>. However, if the temperature decreased during the ice ages, then why should the forecasts in different regions of the Earth be the same? In any case, the influence of the warm

---

\*Corresponding Author:

Peter Mazurkin,

Volga State University of Technology, Yoshkar-Ola, the Republic of Mari El, Russia;

Email: [kaf\\_po@mail.ru](mailto:kaf_po@mail.ru)

DOI: <https://doi.org/10.30564/jasr.v5i3.4674>

Copyright © 2022 by the author(s). Published by Bilingual Publishing Co. This is an open access article under the Creative Commons Attribution-NonCommercial 4.0 International (CC BY-NC 4.0) License. (<https://creativecommons.org/licenses/by-nc/4.0/>).

upper layers of the atmosphere over the Atlantic should affect the slow increase in the average annual temperature not only in the territory of Central England <sup>[2]</sup>, but also at the continental meteorological station of Berlin.

Monthly and annual temperature differences and their changes were considered, for example, in article Ding J., et al. <sup>[3]</sup> on the Tibetan plateau and its environs for 1963–2015.

The earth warmed at an unprecedented rate during the 1980s and 1990s, and the rapidity of the warming coincided with a 65-year cycle. The observed trends in global average surface temperature up to one-third of the warming at the end of the 20th century could be due to natural variability <sup>[4]</sup>. Then it is impossible to draw conclusions from the short length of the dynamic temperature series. We need data for at least 175 years.

The intensity of Moscow's heat island has intensified despite the pause in global warming. It was found that the heat island can be traced vertically up to a height of 2 km. In summer, the lower part of the heat island represents dryness, while the upper part of the heat island corresponds to humidity. In winter, humidity is released in the lower part of the heat island <sup>[5]</sup>. In large cities, in addition, the temperature of the surface air layer increases due to the growth of the heat island over the years.

The unprecedented intensification of extreme weather events in recent years motivates research to understand long-term climate change <sup>[6]</sup>. But this uses averaged data, for example, for 10 years. Therefore, in many studies, transformed series of measurements are used. Mathematical methods are limited only to linear trends and strong data averaging. As a result, the so-called identification of the climate pattern occurs.

Comparison of the surface air temperature variability in three coupled integrations of the “ocean-atmosphere” model over 1000 years is also performed according to linear trends <sup>[7]</sup>. But land surface temperature measurements are the longest and most reliable. Gradually comes the understanding of the invariability of dynamic series according to the primary measurement data and the ban on all sorts of groupings in favor of the linearization method. There comes an awareness of the need to identify directly primary data by wave equations without tricks by their groupings.

As a result, time series of global or regional surface air temperatures are of fundamental importance for climate change studies <sup>[8]</sup>.

We carried out a wavelet analysis of the annual dynamics of the maximum temperature from 1878 to 2017 according to the Hadley Center for Central England Temperature (Hadcet) <sup>[9]</sup>.

The sun heats the Earth unevenly: the equator gets more, the poles get smaller. This temperature gradient is one of the main forces that drives the ocean and atmosphere. In the tropics, the climate system of our planet receives energy, and in temperate and polar latitudes it gives it away. The main transfer of heat from the equator to the pole is carried out in the atmosphere. The ocean is the slow component of the climate system. It does not respond as sharply to external influences as the atmosphere. In heat transfer, the ocean acts as a battery: taking heat from the Sun and heating up, it then shares it with the air <sup>[10]</sup>.

The climate is strongly influenced by solar activity <sup>[11]</sup>. The influence of solar activity on the temperature of the troposphere and the surface of the ocean proves the following conclusion <sup>[12]</sup>. According to Zherebcov G.A. et al., “There is reason to believe that global warming is now almost over and we should expect a slow decrease in the period 2014–2040, primarily in the Northern Hemisphere over land.”

The purpose of the study is to identify asymmetric wavelets of the dynamics of the mean annual temperature in Berlin from 1701 to 2021 by the identification method <sup>[12-17]</sup>, as well as to analyze the warming trends in Berlin until 2340 with a different number of wavelets.

## 2. Materials and Methods

For the possibility of modeling the dynamics of the average annual temperature by a set of wave equations, the initial time is taken  $\tau_0 = 0$  for 1701. For modeling the dynamics, a series of average annual temperatures is taken with discontinuities (lack of data for some years). Gaps in the time series according to the data do not give an accurate division of the dynamics into a set of wavelets (quanta of behavior).

The surface average annual temperature series for Berlin were taken from the site <http://www.pogodaiklimat.ru/history/10384.htm> (Accessed 04/01/2022).

Table 1 gives a fragment of the data array of the average annual temperature of the surface air layer at a height of 2 m according to measurements at the meteorological station in Berlin.

For 1701, data are not available for all months, so there is no average annual temperature.

In Table 1 there are 292 values in total with some gaps out of 28 values. As you know, the measurement error decreases over the years due to the increase in the accuracy of thermometers.

Success in physics is largely determined by the use of mathematics. Physicists often create the necessary mathematical apparatus themselves <sup>[18]</sup>.

We have developed a method for identifying succes-

sively a set of regularities in the form of asymmetric wavelet signals. This set is essentially a general algebraic (trigonometric) equation according to Rene Descartes. In this case, each component becomes a separate quantum of behavior of the surface air temperature.

**Table 1.** Berlin temperature

Year	Time $\tau$ , year	Temperature $t$ , °C
1701	0	-
1702	1	6.8
1703	2	7.4
1704	5	7.0
1705	6	6.9
1706	7	6.2
...	...	...
2017	316	10.6
2018	317	11.7
2019	318	11.8
2020	319	11.7
2021	320	10.5

Oscillations (asymmetric wavelet signals) are generally written by the wave formula <sup>[12-16]</sup> of the form:

$$\begin{aligned}
 y_i &= A_i \cos(\pi x / p_i - a_{8i}), \\
 A_i &= a_{1i} x^{a_{2i}} \exp(-a_{3i} x^{a_{4i}}), \\
 p_i &= a_{5i} + a_{6i} x^{a_{7i}},
 \end{aligned}
 \tag{1}$$

where  $y$  is the indicator (dependent factor),  $i$  is the number of the component of the model (1),  $m$  is the number of members in the model (1),  $x$  is the explanatory variable (influencing factor),  $a_1 \dots a_7$  are the parameters of the model (1) that take numerical values during structural and parametric identification in program environment CurveExpert-1.40 (URL: <http://www.curveexpert.net/>) according to statistical data,  $A_i$  is the amplitude (half) of the wavelet (axis  $y$ ),  $p_i$  is the half-period of oscillation (axis  $x$ ).

This article refers to quantum meteorology <sup>[15,16]</sup>, which makes it possible to isolate the quanta of the behavior of the surface layer of the atmosphere in the form of asymmetric wavelets (1) for the average annual temperature in Berlin. According to these identified quanta of the behavior of the average annual temperature, the signals are unknown, therefore, each wavelet needs to be analyzed by specialists using heuristic methods to find out the reasons for the occurrence of the fluctuation. This will reveal the mechanisms of oscillatory climate adaptation at the point of the Earth.

### 3. Results and Discussion

Difficulties arose with the identification of the wave equation for the long period 1702–1850. At this time in

Berlin there was a strong fluctuation in the average annual temperature. This indignation had a significant impact on the distant future. The results and their discussion are given by increasing the number of components of the general wave model (1). The next difficulty was the increase in the average annual temperature in 2018-2020 by 1.3 °C compared to 2021 (10.5 °C). In 2018, the average annual temperature was 10.6 °C. The beginning of the series, apparently, is irreparable, and the end of the series will have to wait a few years.

### 3.1 Two Components of the Dynamics of the Average Annual Temperature

#### 3.1.1 Pattern

Temperature is a physical quantity that is a measure of the average kinetic energy of the translational movement of molecules, in our case, air molecules in the surface layer at a height of 2 m above the land surface in the city of Berlin.

Initially, only two components of the model were identified (1). The arithmetic mean temperature was taken as the first component (Figure 1). This technique is justified by the large length of the dynamic temperature series of 320 years. If we immediately take a two-term trend as a pattern for identification, then it may turn out that a identification will occur. And the second component was taken as an infinite-dimensional wavelet containing the amplitude in the form of an exponential law.

From the trend graph, it can be seen that the correlation coefficient of the arithmetic mean temperature value is zero, but the maximum value of the standard deviation is 0.9455. However, the two components of the model (1) do not yet have a complete structure. Therefore, we further increase the construction of the equation (Table 2) by the parameters further and determine the limits of such construction.

Table 2 shows the design parameters of the general model (1) and the adequacy of the correlation coefficient, and Figure 2 shows a graph for these parameters.

The trend is characterized by a modified Mandelbrot equation showing exponential growth with a high growth rate of 1.47421. The wave equation also has an amplitude in the form of the Mandelbrot law (in mathematics, the Laplace law, in biology, the Zipf-Pearl law, in econometrics, the Pareto law), when the exponential growth rate is 1.

For 1701, the period of oscillation was  $2 \times 60.33333 \approx 120.7$  years. By 2021, the period has decreased and became equal to 87.6 years. The trend is that by 2340 the period of oscillation will decrease to 30.2 years. Such an

increase in fluctuations indicates an imbalance in climate disturbances in temperature in Berlin.

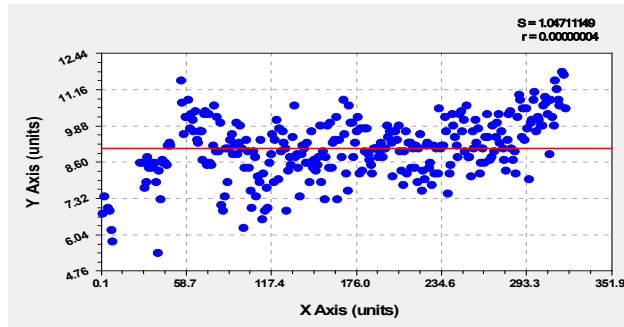
### 3.1.2 Distribution of Modeling Error

The number of points  $n_\varepsilon$  (pieces) in the intervals through 1 °C of the relative error  $[\varepsilon]$  (%) is given in Table 3.

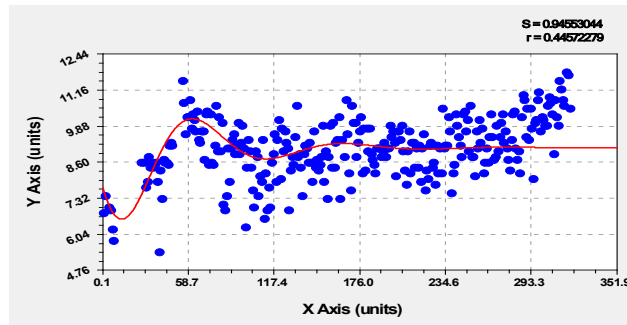
Three dots are excluded here (−36 two dots and −59 one dot).

Then the error changes according to the Gauss law (Figure 3) in the form of the equation:

$$n_\varepsilon = 13.3322 \exp(-0.0062225([\varepsilon] - 1.69821)^2). \quad (2)$$



Trend as arithmetic mean



Trend and Infinite Wavelet

**Figure 1.** Preliminary graphs of temperature dynamics in Berlin for 1701–2021. (in the upper right corner:  $S$  – standard deviation;  $r$  – correlation coefficient)

**Table 2.** Parameters of the dynamics of average annual temperatures in Berlin for 1701–2021

$i$	Asymmetric wavelet $y_i = a_{1i}x^{a_{2i}} \exp(-a_{3i}x^{a_{4i}}) \cos(\pi x / (a_{5i} + a_{6i}x^{a_{7i}}) - a_{8i})$								Coef. correl. $r$
	Amplitude (half) oscillation				Half cycle oscillation			Shift	
	$a_{1i}$	$a_{2i}$	$a_{3i}$	$a_{4i}$	$a_{5i}$	$a_{6i}$	$a_{7i}$	$a_{8i}$	
1	8.42480	0	-3.45328e-5	1.47421	0	0	0	0	0.5933
2	-2.02059	0	0.011180	1	60.33333	-0.0038429	1.45095	0.42159	

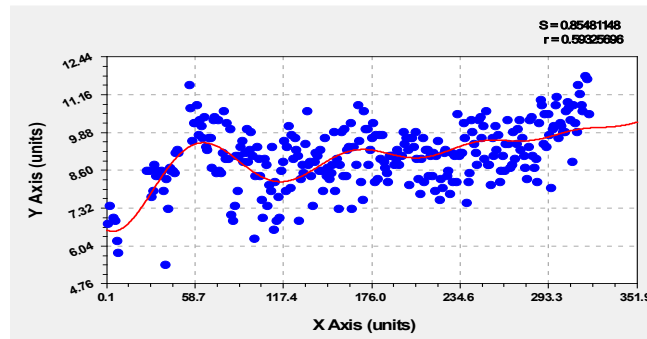
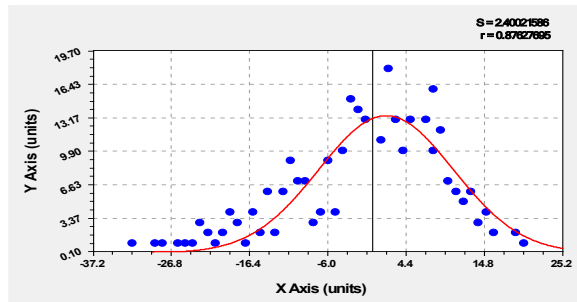


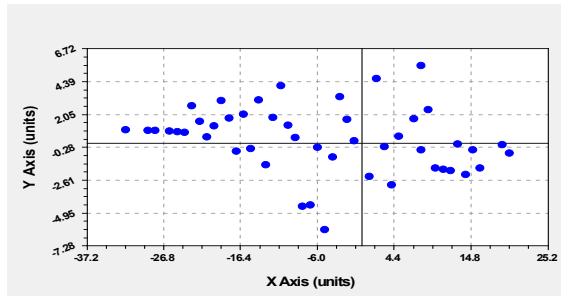
**Figure 2.** Graph of the dynamics of the average annual temperature in Berlin for 1701–2021

**Table 3.** Distribution of the relative error of the model according to Table 2 by intervals

Interval [ $\varepsilon$ ], °C	Quantity $n_{\varepsilon}$ , шт.	Interval [ $\varepsilon$ ], °C	Quantity $n_{\varepsilon}$ , шт.	Interval [ $\varepsilon$ ], °C	Quantity $n_{\varepsilon}$ , шт.	Interval [ $\varepsilon$ ], °C	Quantity $n_{\varepsilon}$ , шт.
20	1	8	10	-7	4	-19	4
19	2	5	13	-8	3	-20	2
16	2	4	10	-9	7	-21	1
15	4	3	13	-10	7	-22	2
14	3	2	18	-11	9	-23	3
13	6	1	11	-12	6	-24	1
12	5	-1	13	-13	2	-25	1
11	6	-2	14	-14	6	-26	1
10	7	-3	15	-15	2	-28	1
9	12	-4	10	-16	4	-29	1
8	16	-5	4	-17	1	-32	1
7	13	-6	9	-18	3	-	-



Relative error



Remainders of Equation (2)

**Figure 3.** Graphs of the distribution of relative error and residuals from the model (2)

The normal distribution law is observed with the adequacy of 0.8763.

### 3.1.3 A Look into the Future until 2340

The forecasting theory assumes that the forecast horizon is maximally equal to the length of the forecast base.

By direct calculations in the Excel software environment using the formula from Table 2, the graph shown in Figure 4 was obtained. The graph shows that for the period 2021–2340 the average annual temperature is increasing. This confirms the CMIP5 prediction<sup>[1]</sup>.

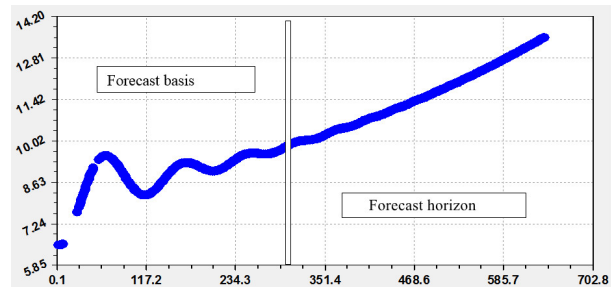


**Figure 4.** Forecast graph up to 2340 for the model with two components

Next, we increase the number of wavelets in the general model (1) to five.

## 3.2. General Formula (1) with Five Components

### 3.2.1 Features of CurveExpert-1.40

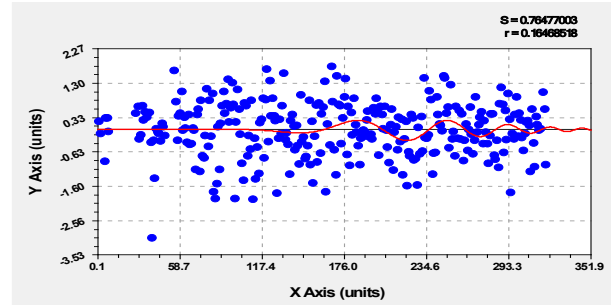
Subsequently, the identification method was used to increase the asymmetric components until five components were reached (Table 4 and Figure 5). The first four components were placed together in the CurveExpert-1.40 software environment, and the fifth component was identified separately.

**Table 4.** Parameters of the Berlin mean annual temperature dynamics model for 1701–2021

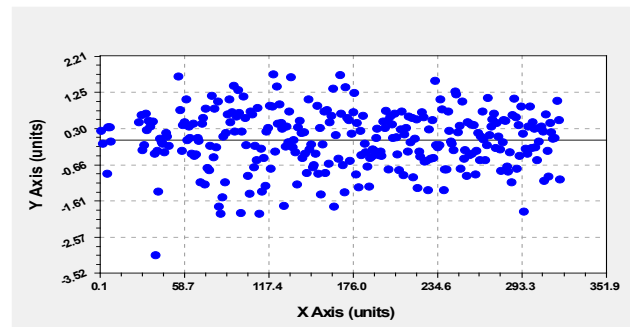
i	Asymmetric wavelet $y_i = a_{1i}x^{a_{2i}} \exp(-a_{3i}x^{a_{4i}}) \cos(\pi x / (a_{5i} + a_{6i}x^{a_{7i}}) - a_{8i})$								Coef. correl. $r$
	Amplitude (half) oscillation				Half cycle oscillation			Shift	
	$a_{1i}$	$a_{2i}$	$a_{3i}$	$a_{4i}$	$a_{5i}$	$a_{6i}$	$a_{7i}$	$a_{8i}$	
1	10.70443	0	-0.00098192	1	0	0	0	0	0.6819
2	-3.70801	0	0.00044630	1.80931	84.54606	-17.31516	9.13583	0.82444	
3	-1.63401	0	-0.0055698	1.17114	1.38827	0.17453	1.01460	-3.93651	
4	0.0045885	0	-1.99283	0.14237	3.89621	0	0	1.04925	
5	1.0182e-28	14.28439	0.045726	105821	105.6803	-0.20700	1.00480	-3.91402	0.1647

The level of adequacy with a correlation coefficient of 0.6819 almost approached 0.7, that is, a strong relationship between time and average annual temperature in Berlin. An equation with three components gets a correlation coefficient of 0.6517. Having fixed the degrees in the form of numbers, the fourth component is additionally introduced. The correlation coefficient increased to 0.6819.

An additional fifth component gives a correlation coefficient of only 0.1647 (Figure 5). Therefore, starting from the sixth component, the remaining wavelets do not give fundamental changes in the model. However, due to the quantum certainty of the dynamic series of mean annual temperature, it becomes possible to identify up to the 65th component of the general model (1). We did not bring the wavelet analysis up to the measurement error of  $\pm 0.05$  °C, because already with the second component, the rest of the wavelets do not have a significant impact on the future.



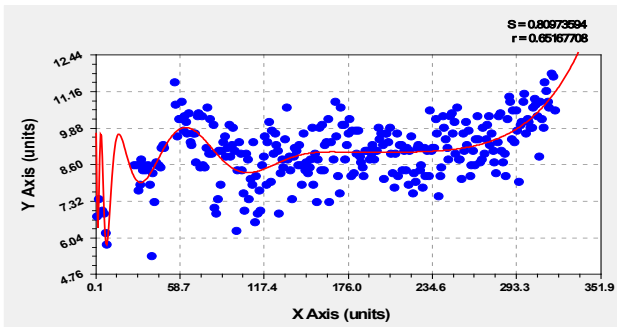
Fifth component



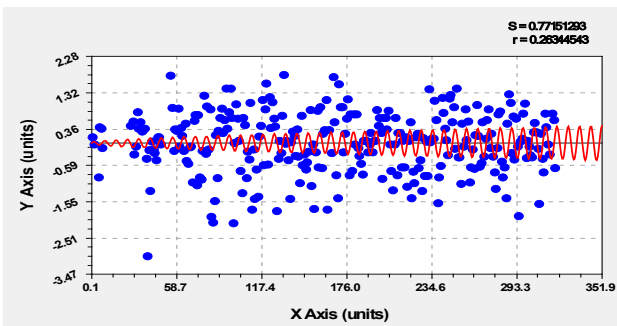
Residuals after the fifth component

**Figure 5.** Graphs of the dynamics of the average annual temperature in Berlin for 1701–2021

Figure 6 shows a general graph for the four components.



Equation (1) with three components



Fourth component

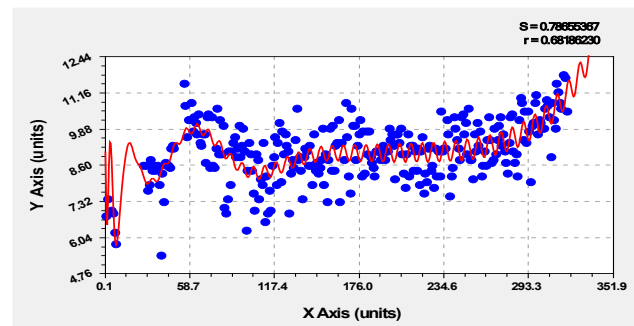


**Figure 6.** Graph of the average annual temperature in Berlin in four components

Why can a dynamic series be decomposed into a large

number of wavelets? However, a small number of the first components are taken for forecasting? So far, we do not have answers to these questions.

From the graph in Figure 6, it can be seen that since 1701 the tremor period has increased. Therefore, it would be very interesting to have a number from 1650. In 1759–1760, the temperature in Berlin rose to almost 11.5 °C. From the data in Table 1 it can be seen that the temperature became slightly higher only in 2018–2020. Then, in 2021, the temperature dropped to 10.5 °C. Therefore, we need to wait a few more years for the dynamic series to be determined.

### 3.2.2 Distribution of Modeling Error

With five components, the number of points  $n_\varepsilon$  (pieces) in intervals through 1 °C of the relative error  $[\varepsilon]$  (%) of modeling is given in Table 5.

Then the error changes according to the Gauss law (Figure 7) with the addition in the form of an asymmetric wavelet according to the equation,

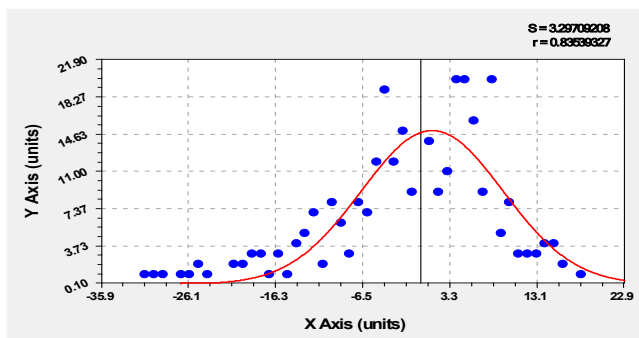
$$n_\varepsilon = 13.89770 \exp(-0.0065317([\varepsilon] - 1.35123)^2) - 1.06484 \cdot 10^{-31}([\varepsilon] + 40)^{25.83643} \exp(-0.41488([\varepsilon] + 40)^{1.08061}) \times \cos(\pi([\varepsilon] + 40) / (1.82689 + 0.0012950([\varepsilon] + 40)^{1.69907})) - 0.016560 \quad (3)$$

The correlation coefficient of the trend in the form of the Gaussian law of the normal distribution is 0.8354, and with the addition of a wavelet according to formula (3) it is 0.9018. Then it turns out that not only the average annual temperature changes according to the equations of oscillatory adaptation, but also the relative modeling errors have a wave character. It is applied in addition to the Gaussian law of the normal distribution.

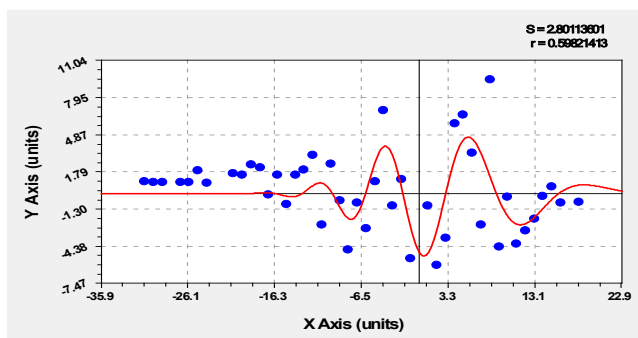
Table 5. Model error distribution from Table 4 with five components

Interval $[\varepsilon]$ , °C	Quantity $n_\varepsilon$ , шт.	Interval $[\varepsilon]$ , °C	Quantity $n_\varepsilon$ , шт.	Interval $[\varepsilon]$ , °C	Quantity $n_\varepsilon$ , шт.	Interval $[\varepsilon]$ , °C	Quantity $n_\varepsilon$ , шт.
18	1	5	20	-8	3	-20	2
16	2	4	20	-9	6	-21	2
15	4	3	11	-10	8	-24	1
14	4	2	9	-11	2	-25	2
13	3	1	14	-12	7	-26	1
12	3	-1	9	-13	5	-27	1
11	3	-2	15	-14	4	-29	1
10	8	-3	12	-15	1	-30	1
9	5	-4	19	-16	3	-31	1
8	20	-5	12	-17	1	-57	1
7	9	-6	7	-18	3	-	-
6	16	-7	8	-19	3	-	-

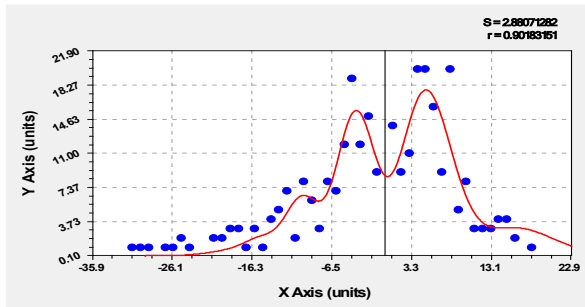
Note: Due to the sharp selection from the series, the last point is excluded.



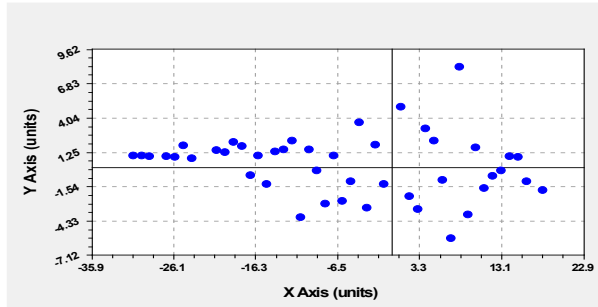
Error according to the well-known Gauss law



Asymmetric Error Wavelet



The sum of the Gauss law and the wavelet



Leftovers after model (3)

**Figure 7.** Graphs of the distribution of the relative error from the model from Table 4

### 3.2.3 Prediction according to Equation (3)

According to the equations from Table 4 in Figure 8, a graph is built. After 2022, it rises sharply. This happens because of the different signs of the components of the general model (1).

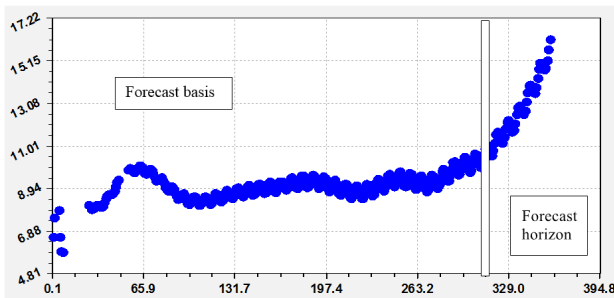


**Figure 8.** Prediction graph for the five equations of mean annual temperature until 2060

Then it turns out that, as quanta of behavior, the average annual temperature of Berlin is decomposed into 65 components, and the forecast can only be made using the first two formulas from Table 2. The climate of Berlin is significantly influenced by warm air currents over the Atlantic Ocean, which has an oscillatory character.

## 4. Conclusions

The revealed regularities of the average annual temperature of Berlin from 1701 to 2021 made it possible to positively answer the statement that the model with two components gives continuous growth, which is consistent with the conclusions of the IPCC report on global warming. However, we believe that in the depths of the Eurasian continent, due to the opposition of various mountain ranges to air flows from the Atlantic, there may be other trends aimed at global cooling.

In this regard, it is necessary to study the patterns and other regional assessments of climate change. For Berlin, the last three years are characterized by sharp decreases in

the average annual temperature from 11.8 °C to 10.5 °C, that is, by 12.4% in 2021. Therefore, the forecast is still unstable, since a further decrease in the average annual temperature of Berlin in the near future may change the whole picture according to many models.

## Conflict of Interest

There is no conflict of interest.

## Funding

This research received no external funding.

## References

- [1] Wu, Zh.H., Huang, N.E., Wallace, J.M., et al., 2011. On the time-varying trend in global-mean surface temperature. *Climate Dynamics*.37(3), 759-773.  
DOI: <https://doi.org/10.1007/s00382-011-1128-8>
- [2] Li, Q., Zhang, L., Xu, W., et al., 2017. Comparisons of time series of annual mean surface air temperature for China since the 1900s: observations, model simulations, and extended reanalysis. *Bulletin of the American Meteorological Society*, 98(4), 699-711.  
DOI: <https://doi.org/10.1175/bams-d-16-0092.1>
- [3] Ding, J., Cuo, L., Zhang, Y.X., et al., 2018. Monthly and annual temperature extremes and their changes on the Tibetan Plateau and its surroundings during 1963-2015. *Scientific reports*.  
DOI: 10.1038/s41598-018-30320-0
- [4] Mazurkin, P.M., Kudryashova, A.I., 2019. Quantum meteorology. *International Multidisciplinary Scientific GeoConference Surveying Geology and Mining Ecology Management, SGEM*. 5(1), 619-627.  
DOI: <https://doi.org/10.5593/sgem2019/5.1/S20.077>
- [5] Zappalà, D.A., Barreiro, M., Masoller, C., 2018. Quantifying changes in spatial patterns of surface air temperature dynamics over several decades. *Earth*

- System Dynamics. 9(2), 383-391.  
DOI: <https://doi.org/10.5194/esd-9-383-2018>
- [6] Mazurkin, P.M., Kudryashova, A.I., 2019. Urban phytometeorology: influence of the sum of temperatures on the ontogeny of drooping birch leaves. *Geographical Bulletin*. 4(51), 45-58. (in Russian).  
DOI: <https://doi.org/10.17072/2079-7877-2019-4-45-58>
- [7] Stouffer, R.J., Hegerl, G., Tett, S., 2000. A Comparison of Surface Air Temperature Variability in Three 1000-Yr Coupled Ocean–Atmosphere Model Integrations. *Journal of Climate*. 13(3), 513-537.
- [8] Kislov, A., Varentsov, M., Gorlach, I.A., et al., 2017. «Heat island» of the Moscow agglomeration and the urban-induced amplification of of global warming. Article in *Vestnik MGU. Serija V, Geografia*. <https://www.researchgate.net/publication/320057275> (in Russian).
- [9] Mazurkin, P.M., Wavelet analysis of annual dynamics of maximum temperature from 1878 to 2017 and forecast data Hadley center Central England temperature (Hadcet). *International Journal of Current Research*. 11(09), 7315-7324.  
DOI: <https://doi.org/10.24941/ijcr.36626.09.2019>
- [10] Mazurkin, P.M., 2019. Wavelet analysis of the annual dynamics of the average temperature from 1659 to 2017 and forecast according to Hadley center central England temperature (HadCET) data. *Exact Science Journal of Natural Sciences*. [www.t-nauka.ru](http://www.t-nauka.ru). Issue. 45. Kemerevo: Pluto Publishing House. pp. 50-65. (in Russian).
- [11] Balkhanov, V.K., 2019. Fractal Geometry: Axioms, Fractal Derivative and Its Geometrical Meaning. *Journal of Environmental & Earth Sciences*. 1(1).  
DOI: <https://doi.org/10.30564/jees.v1i1.475>
- [12] Zherebcov, G.A., Kovalenko, V.A., Molodyh, S.I., et al., 2013. Influence of solar activity on tropospheric and ocean surface temperatures. *News of the Irkutsk State University. Series Earth Sciences*. 6(1), 61-79. (in Russian).
- [13] Chernokulsky, A., 2022. Will Europe freeze without the Gulf Stream? pp. 46. [https://zen.yandex.ru/media/nplus1/zamerznet-li-evropa-bez-golfstrima-62028bab5eaa831b62461219?utm\\_campaign=dbr&](https://zen.yandex.ru/media/nplus1/zamerznet-li-evropa-bez-golfstrima-62028bab5eaa831b62461219?utm_campaign=dbr&) (Accessed 13 March 2022). (in Russian).
- [14] Zharkova, V., 2019. The solar magnet field and the terrestrial climate. <https://watchers.news/2018/11/11/valentina-zharkova-solar-magnet-field-and-terrestrial-climate-presentation/> (Accessed 1 March 2019).
- [15] Mazurkin, P.M., 2021. Quantum biophysics of the atmosphere: factor analysis of the annual dynamics of maximum, minimum and average temperatures from 1879 to 2017 to Hadley English Temperature Center (Hadcet). *Journal of Environmental & Earth Sciences*. 3(1), 29-40.  
DOI: <https://doi.org/10.30564/jees.v3i1.2489>
- [16] Mazurkin, P.M., 2021. Bioclimatic regularities of change in the density of organic carbon of the steppe soil in different regions of the World. *Journal of Atmospheric Science Research*. 4(1), 16-25.  
DOI: <https://doi.org/10.30564/jasr.v4i1.2521>
- [17] Mazurkin, P.M., 2021. Factor analysis of the parameters of samples of the steppe soil and grass of Mongolia and Inland Mongolia of China on the eastern transect of the Eurasian steppe. *Journal of Geological Research*. 3(1), 1-10.  
DOI: <https://doi.org/10.30564/jgr.v3i1.2520>
- [18] Friedrich, T., Timmermann, A., Tigchelaar, M., et al., 2016. Nonlinear climate sensitivity and its implications for future greenhouse warming. *Science Advances*. 2(11).  
DOI: <https://www.science.org/doi/full/10.1126/sciadv.1501923>

ARTICLE

# Significant Improvement in Rainfall Forecast over Delhi: Annual and Seasonal Verification

Kuldeep Srivastava \* 

Scientist & Head, Regional Weather Forecasting Center (RWFC), India Meteorological Department, New Delhi, India

---

ARTICLE INFO

*Article history*

Received: 4 June 2022

Revised: 30 June 2022

Accepted: 1 July 2022

Published: 14 July 2022

*Keywords:*

Thunderstorms

Percentage correct

Probability of detection

Missing ratio

False alarm ratio

Critical success index

True skill statistics

Heidke skill score

---

ABSTRACT

Regional Weather Forecasting Centre (RWFC) New Delhi has the responsibility to issue and disseminate rainfall forecast for Delhi. So it is very important to scientifically verify the rainfall forecast issued by RWFC. In this study rainfall forecast verification of Delhi has been carried out annually and season wise for the period 2011 to 2021. Various statistical parameters such as Percentage Correct (PC), Probability of Detection (POD), Missing Ratio (MR), False Alarm Ratio (FAR), Critical Success Index (CSI), True Skill Statistics (TSS) and Heidke Skill Score (HSS) have been calculated for season wise and annually. A forecast is considered to be improved if PC, POD, CSI, TSS and HSS increase and FAR and MR decrease over a period of time. The author can conclude that annual accuracy of forecast has increased significantly over the period of time from 2011 to 2021, as PC, POD, CSI, TSS and HSS increase and FAR and MR decrease over a period of time. Maximum contribution in the improved forecast has observed in transition season (pre-monsoon season followed by post-monsoon, having rainfall activity mainly in association with thunderstorms), when FAR and MR have decreased drastically.

## 1. Introduction

Delhi is tremendously affected by severe weather activities such as heavy rainfall during monsoon season; severe thunderstorms, severe heat wave, strong squally wind and dust storm during summer season; dense fog, severe cold wave during winter season. Severe weather effects public life such as human health issues during heat and cold wave

conditions, air and surface traffic is very much affected during heavy rain, dense fog and strong squally wind, public property is damaged due to heavy rain etc. In India January and February months fall in winter season, March, April and May months fall in pre-monsoon (Summer Season), June, July, August and September months fall in monsoon season (Rainy Season) and October, November and December months fall in post-monsoon Season.

---

\*Corresponding Author:

Kuldeep Srivastava,

Scientist & Head, Regional Weather Forecasting Center (RWFC), India Meteorological Department, New Delhi, India;

Email: [kuldeep.ind@gmail.com](mailto:kuldeep.ind@gmail.com)

DOI: <https://doi.org/10.30564/jasr.v5i3.4769>

Copyright © 2022 by the author(s). Published by Bilingual Publishing Co. This is an open access article under the Creative Commons Attribution-NonCommercial 4.0 International (CC BY-NC 4.0) License. (<https://creativecommons.org/licenses/by-nc/4.0/>).

Mason <sup>[1]</sup> discussed about the numerous reasons for performing a verification analysis, there are usually two general questions that are of interest: are the forecasts good, and can we be confident that the estimate of forecast quality is not misleading? In general, the vast majority of verification efforts over the past decades have focused on the calculation of one or more verification scores over a forecast-observation dataset, where the observations usually consist of surface or upper air point observations or analyses onto grids. These methods are sometimes referred to as “traditional verification” to contrast them with more recent developments in verification methodology. Casati <sup>[2]</sup> has discussed the current issues in forecast verification, reviews some of the most recently developed verification techniques, and provides recommendations for future research. Research and development of new approaches to verification has increased greatly over the last 10 years or so, and has been motivated by several factors, including the availability of new sources of data such as satellite and radar, the desire to generate verification results which are more meaningful to specific users or user groups, the advent of new modelling strategies such as ensembles, and the evolution of models and forecasts to higher spatial and temporal resolution. Nurmi <sup>[3]</sup> provides some general guidelines, various verification measures for continuous meteorological variables, for binary and multi-category weather events and for probabilistic forecasts. Forecast value and the end user decision making issues associated with forecast verification. Murphy <sup>[4]</sup> has described differences of opinion exist among forecasters and between forecasters and users—regarding the meaning of the phrase “good (bad) weather forecasts”. Three distinct types of goodness are identified. 1) The correspondence between forecasters’ judgments and their forecasts (type 1 goodness, or consistency), 2) the correspondence between the forecasts and the matching observations (type 2 goodness, or quality), and 3) the incremental economic and/or other benefits realized by decision makers through the use of the forecasts (type 3 goodness, or value). Each type of goodness is defined and described. In addition, issues related to the measurement of consistency, quality, and value are discussed. Nathan <sup>[5]</sup> explained a method for determining baselines of skill for the purpose of the verification of rare-event forecasts and examples are presented to illustrate the sensitivity to parameter choices. The Storm Prediction Center’s convective outlook slight risk areas are evaluated over the period from 1973 to 2011 using practically perfect forecasts to define the maximum values of the critical success index that a forecaster could reasonably achieve given the constraints of the forecast, as well as the minimum values of the critical success in-

dex that are considered the baseline for skilful forecasts. The annual frequency of skilful daily forecasts continues to increase from the beginning of the period of study, and the annual cycle shows maxima of the frequency of skilful daily forecasts occurring in May and June. Srivastava <sup>[6]</sup> stated that the rainfall can be estimated with a fair degree of accuracy at desired locations within the range of the Doppler Weather Radar using the radar rainfall products and the developed linear regression model.

Doswell <sup>[7]</sup> the so-called True Skill Statistic (TSS) and the Heidke Skill Score (S), as used in the context of the contingency, table approach to forecast verification, are compared. It is shown that the TSS approaches the Probability of Detection (POD) whenever the forecasting is dominated by correct forecasts of non-occurrence, i.e., forecasting rare events like severe local storms. This means that the TSS is vulnerable to “hedging” in rare event forecasting.

Rainfall activities over Delhi occurs in association with western disturbances (WD) during winter season, in summer season rainfall occurs due to convective thunder storms, during rainy season it occurs in association with monsoonal flow and in post monsoon season due to thunderstorms associated with WD. Regional Weather Forecasting Centre (RWFC) New Delhi has the responsibility to issue and disseminate warnings for the rainfall and disastrous weather affecting Delhi including National Capital Region (NCR). So, it is very important to scientifically verify the rainfall forecast issued by RWFC.

The main objective of this study is to verify the rainfall forecast issued by Regional Weather Forecasting Centre (RWFC) on day-to-day basis. Verification of Delhi has been carried out annually and season wise for the period 2011 to 2021. Various statistical parameters such as Percentage Correct (PC), Probability of Detection (POD), Missing Ratio (MR), False Alarm Ratio (FAR), Critical Success Index (CSI), True Skill Statistics (TSS) and Heidke Skill Score (HSS) have been calculated for season wise and annually. A forecast is considered to be improving if PC, POD, CSI, TSS and HSS increases and FAR and MR decreases over a period of time.

Data used in this study is described in section 2, Methodology used for forecast verification is described in section 3, Analysis and discussion of rainfall forecast verification has been carried out annually and season wise for the period 2011 to 2021 using various statistical parameters in the Section 4 and finally results are concluded in the section 5.

## 2. Data

To carry out the verification of forecast 24 hours observed rainfall data has been collected from five obser-

vatories of Delhi, namely Safdarjung, Palam, Ayanagar, Ridge and Lodi Road. These observatories are located within 20 km radius from Safdarjung observatory. 24-hour rainfall forecast has been collected from Regional Weather Forecasting Center (RWFC) New Delhi. Using observed and forecast rainfall data various statistical parameters are calculated and forecast verification is done.

### 3. Forecast Verification Methodology

To verify the forecast, a contingency table is prepared which shows the frequency of “yes” and “no” forecasts and occurrences. The four combinations are:

*Hit Event:* It means forecast to occur, and did occur

*Miss Event:* It means forecast not to occur, but did occur

*False Alarm:* It means event forecast to occur, but did not occur

*Correct non-event:* It means event forecast not to occur, and did not occur

The contingency table is a useful way to see what types of errors are being made. A perfect forecast system would produce only *hits* and *correct non-event*, and no *misses* or *false alarms* (Table 1).

**Table 1.** Contingency Table

Event Forecast	Event Observed		Marginal Total
	Yes	No	
Yes	Hits	False Alarm	Forecast Yes
No	Miss	Correct Non Event	Forecast No
Marginal Total	Observed Yes	Observed No	Sum Total

Categorical statistics that can be computed from the yes/no contingency table are given below.

#### 3.1 Percentage Correct (PC)

Percentage Correct is the accuracy in (%) using the following formula. *Its range is 0 to 1 and Perfect score is 1.* It is simple, intuitive. It can be misleading since it is heavily influenced by the most common category, usually “no event” in the case of rare weather.

$$Accuracy = \frac{hits + correct\ negatives}{total}$$

#### 3.2 Probability of Detection (Hit Rate)

*It tells fraction of the observed “yes” events that were correctly forecast. Its range is 0 to 1 and Perfect score is 1.* It is sensitive to hits, but ignores false alarms. POD is very sensitive to the climatological frequency of the event and good for rare events.

$$POD = \frac{hits}{hits + misses}$$

#### 3.3 False Alarm Ratio (FAR)

*It tells the fraction of the predicted “yes” events that actually did not occur. Its range is 0 to 1 and Perfect score is 1.* FAR is sensitive to false alarms, but ignores misses. FAR is Very sensitive to the climatological frequency of the event.

$$FAR = \frac{false\ alarms}{hits + false\ alarms}$$

#### 3.4 Critical Success Index (CSI)

Also known as *Threat score*. *It tells how well did the forecast “yes” events correspond to the observed “yes” events. Its range is 0 to 1 and Perfect score is 1.* It Measures the fraction of observed and/or forecast events that were correctly predicted. Sensitive to hits, penalizes both misses and false alarms. Does not distinguish source of forecast error. Depends on climatological frequency of events (poorer scores for rarer events) since some hits can occur purely due to random chance.

$$TS = \frac{hits}{hits + misses + false\ alarms}$$

#### 3.5 True Skill Statistic (TSS or HK)

*It tells how well did the forecast separate the “yes” events from the “no” events. Its range is 0 to 1 and Perfect score is 1.* TSS uses all elements in contingency table. The expression is identical to  $HK = POD - POFD$ . For rare events HK is unduly weighted toward the first term (same as POD), so this score may be more useful for more frequent events.

$$HK = \frac{(hits)}{hits + misses} - \frac{false\ alarms}{false\ alarms + correct\ negatives}$$

#### 3.6 Heidke Skill Score

*It tells what was the accuracy of the forecast relative to that of random chance. Its range is 0 to 1 and Perfect score is 1.* It Measures the fraction of correct forecasts after eliminating those forecasts which would be correct due purely to random chance.

$$Hss = \frac{(hits + correct\ negatives) - (expected\ correct)_{random}}{N - (expected\ correct)_{random}}$$

where,

$$(expected\ correct)_{random} = \frac{1}{N} \left[ (hits + misses)(hits + false\ alarms) + (correct\ negatives + misses)(correct\ negatives + false\ alarms) \right]$$

### 3.7 Missing Rate

The fraction or percentage of forecast that result in a miss is called the miss rate. It is defined in terms of Hit Rate or POD, which is described in 3.2:

$$\text{Missing Rate (MR)} = 1 - \text{Hit Rate}$$

## 4. Results and Discussion

In this section analysis and discussion of rainfall forecast verification has been carried out annually and season wise for the period 2011 to 2021 using various statistical parameters.

### 4.1 Annual Forecast Verification

#### 4.1.1 Percentage Correct (PC)

Figure 1 depicts the percentage correct (PC) forecast during the period 2011 to 2021 over Delhi. In the year 2011 and 2012 percentage correct forecast was 88% and 92% respectively with False Alarm Ratio (FAR) was 0.27 and 0.31 respectively (Figure 3). FAR is quite high when compared with the year 2021 having PC and FAR as 93% and 0.13. In the year 2013 percentage correct forecast was 79%, which has increased to 93% in the year 2021. Thus, the accuracy of forecast for Delhi has increased by 14% in last 8 years. It shows that there is significant improvement in the accuracy of forecast after 2013.

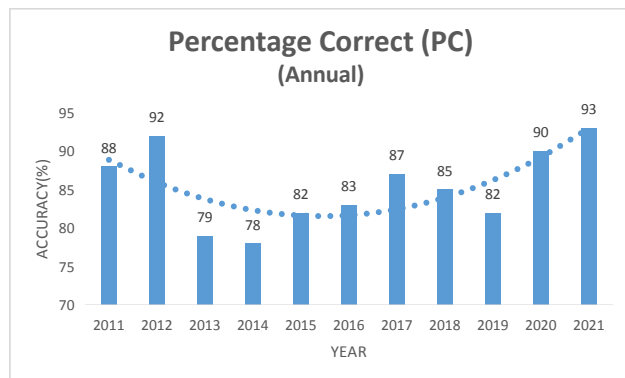


Figure 1. Percentage Correct (PC) for Forecast of Delhi during (2011 – 2021)

#### 4.1.2 Probability of Detection (POD)

The Probability of Detection (POD) for the rainfall event during the period 2011 to 2021 over Delhi is shown in the Figure 2. In the year 2011 and 2012 Probability of Detection (POD) of a rainfall event was around 0.80. In the year 2013 Probability of Detection (POD) was 0.58, which has increased to 0.91 in the year 2021. Thus, the Probability of Detection (POD) for Delhi has increased by

0.33 in the last 8 years. It shows that there is significant improvement in the Probability of Detection (POD) of an event after 2013.

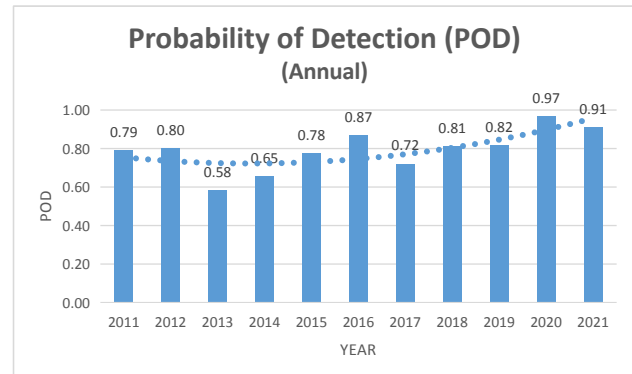


Figure 2. Probability of Detection (POD) for Forecast of Delhi during (2011 – 2021)

#### 4.1.3 False Alarm Ratio (FAR)

Figure 3 illustrates the False Alarm Ratio (FAR) for the rainfall event during the period 2011 to 2021 over Delhi. In the year 2011 and 2012 False Alarm Ratio (FAR) of rainfall event was 0.27 and 0.31 respectively. In the year 2013 False Alarm Ratio (FAR) was very high value 0.62, which has decreased to 0.13 in the year 2021. Thus, the False Alarm Ratio (FAR) for Delhi has decreased by 0.49 in last 8 years. It shows that there is significant decrement in the False Alarm Ratio (FAR) after 2013.

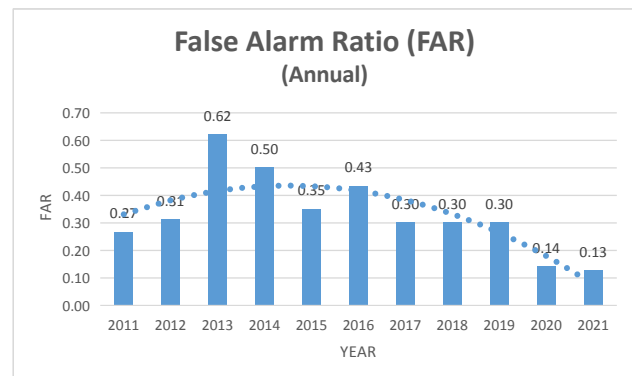


Figure 3. False Alarm Ratio (FAR) for Forecast of Delhi during (2011 – 2021)

#### 4.1.4 Missing Ratio (MR)

The Missing Ratio (MR) for the rainfall event during the period 2011 to 2021 over Delhi is depicted in the Figure 4. In the year 2011 and 2012 Missing Ratio (MR) of a rainfall event was around 0.20. In the year 2013 Missing Ratio (MR) was very high value 0.46, which has decreased to 0.09 in the year 2021. Thus, the Missing Ratio

(MR) of an event for Delhi has decreased by 0.37 in last 8 years. It shows that there is significant decrement in the Missing Ratio (MR) after 2013.

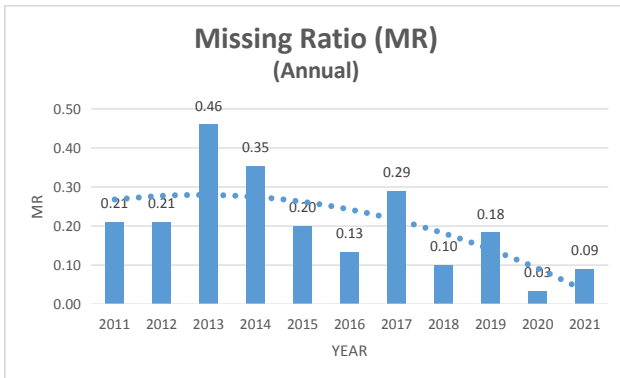


Figure 4. Missing Ratio (MR) for Forecast of Delhi during (2011 – 2021)

#### 4.1.5 Critical Success Index (CSI)

Figure 5 depicts the Critical Success Index (CSI) for the forecast during the period 2011 to 2021 over Delhi. In the year 2011 and 2012 Critical Success Index (CSI) was around 0.60. In the year 2013 Critical Success Index (CSI) was decreased to 0.36, which has increased to 0.81 in the year 2021. Thus, the Critical Success Index (CSI) for the forecast of an event for Delhi has significantly increased by 0.45 in last 8 years. It shows that there is significant improvement in the Critical Success Index (CSI) for the weather forecast after 2013.

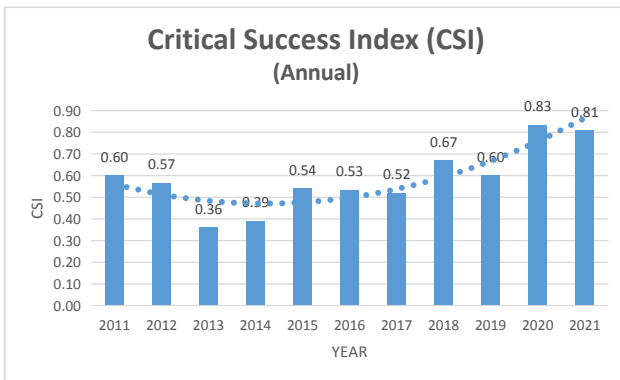


Figure 5. Critical Success Index (CSI) for Forecast of Delhi during (2011 – 2021)

#### 4.1.6 True Skill Statistics (TSS)

Figure 6 depicts the True Skill Statistics (TSS) for the forecast during the period 2011 to 2021 over Delhi. In the year 2011 and 2012 True Skill Statistics (TSS) were 0.61 and 0.68 respectively. In the year 2013 True Skill Statistics (TSS) was decreased significantly to 0.24, which has

increased to 0.79 in the year 2021. Thus, the True Skill Statistics (TSS) for the forecast of an event for Delhi has significantly increased by 0.55 in last 8 years. It shows that there is significant increase in the True Skill Statistics (TSS) for the weather forecast after 2013.

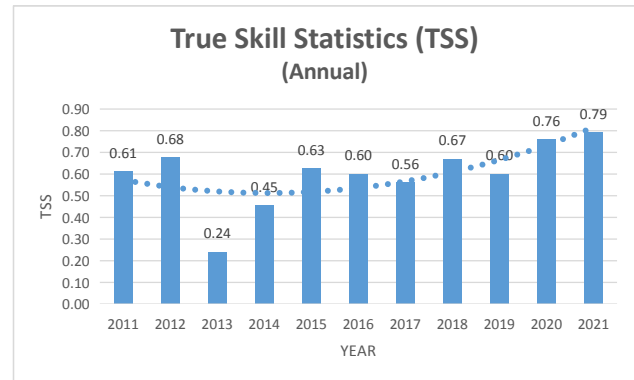


Figure 6. True Skill Statistics (TSS) for Forecast of Delhi during (2011 – 2021)

#### 4.1.7 Heidke Skill Score (HSS)

Figure 7 depicts the Heidke Skill Score (HSS) for the forecast during the period 2011 to 2021 over Delhi. In the year 2011 and 2012 Heidke Skill Score (HSS) were 0.57 and 0.60 respectively. In the year 2013 Heidke Skill Score (HSS) was decreased significantly to 0.25, which has increased to 0.79 in the year 2021. Thus, the Heidke Skill Score (HSS) for the forecast of an event for Delhi has significantly increased by 0.54 in last 8 years. It shows that there is significant increase in the HSS for the weather forecast after 2013.

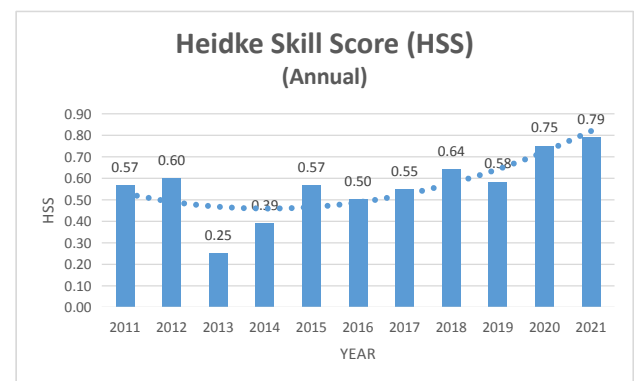


Figure 7. Heidke Skill Score (HSS) for Forecast of Delhi during (2011 – 2021)

Above analysis of PC, POD, FAR, MR, CSI, TSS and HSS for the annual forecast verification for Delhi depicts that PC was higher in the year 2011 and 2012 and again in 2021. But the major difference in these years is that in the year 2021, POD and CSI have significantly increased

and reached up to 0.91 and 0.81 respectively. TSS and HSS also increased significantly in the year 2021 and both reached up to 0.79. Simultaneously FAR and MR have significantly decreased up to 0.13 and 0.9 respectively.

Thus, significant increase in the PC, POD, CSI, TSS and HSS and significant decrease in FAR and MR has been noticed in last 8 years. A forecast is assumed to be improving if PC, POD, CSI, TSS and HSS increases and FAR and MR decreases over a period of time. In this case there is increasing trend in PC, POD, CSI, TSS and HSS while decreasing trend in FAR and MR. This shows that there is significant improvement in the forecast during 2011 to 2021.

## 4.2 Verification of Forecast for Winter Season

### 4.2.1 Percentage Correct (PC)

Figure 8 depicts the percentage correct (PC) forecast during the period 2011 to 2021 over Delhi during winter season. In the winter season of year 2011 and 2012 percentage correct forecast was 84% and 95% respectively with False Alarm Ratio (FAR) around 0.6 and 0.55 respectively (Figure 10). FAR is quite high when compared with the year 2021 having PC and FAR as 98% and 0.0. In the year 2014 percentage correct forecast was 75%, which has increased to 98% in the year 2021. Thus, the accuracy of forecast for Delhi has increased by 23% in last 7 years during winter season. Figure (8) shows that there is significant improvement in the accuracy of forecast after 2014.

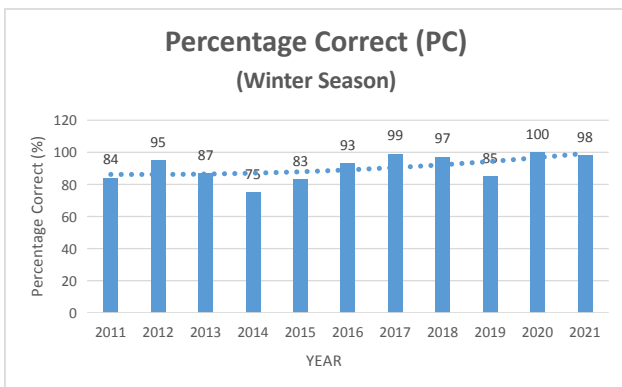


Figure 8. Percentage Correct (PC) for Forecast of Delhi during winter Season (2011 – 2021)

### 4.2.2 Probability of Detection (POD)

The Probability of Detection (POD) for the rainfall event during the period 2011 to 2021 over Delhi is shown in the Figure 9. In the year 2011 and 2012 Probability of Detection (POD) of a rainfall event was around 0.80. In the year 2013 and 2014 Probability of Detection (POD)

was 0.35 and 0.40 respectively, which has increased to 1.0 in the year 2020. Thus, the Probability of Detection (POD) for Delhi has increased by 0.6 in last 6 years. It shows that there is significant improvement in the Probability of Detection (POD) of an event after 2014. In the winter season of the year 2021 POD is reduced to 0.75. Reason for this decrease in POD is that in February 2021 there were only two rainy days, out of which one was predicted correctly and other was missed. Normally 6-7 rainy days are realised in each month of January and February. POD for January 2021 is 1.0, for February 2021 is 0.50 and overall for winter season (2021) is 0.75.

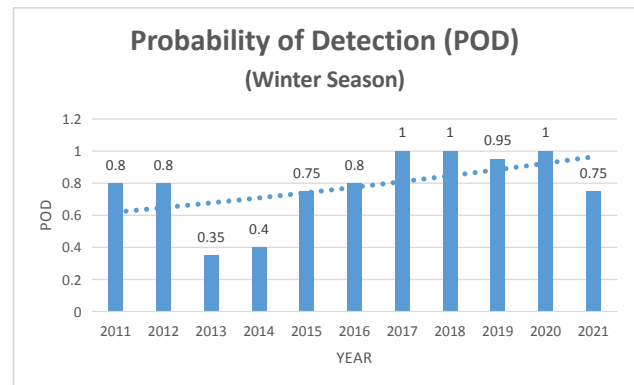


Figure 9. Probability of Detection (POD) for Forecast of Delhi during winter Season (2011 – 2021)

### 4.2.3 False Alarm Ratio (FAR)

Figure 10 illustrates the False Alarm Ratio (FAR) for the rainfall event during the period 2011 to 2021 over Delhi during winter season. In the year 2011 False Alarm Ratio (FAR) of rainfall event was 0.60. In the year 2013 False Alarm Ratio (FAR) was 0.6, which has decreased to 0.0 in the year 2021. Thus, the False Alarm Ratio (FAR) for Delhi has decreased significantly by 0.6 in last 8 years. It shows that there is significant decrement in the False Alarm Ratio (FAR) after 2011.

### 4.2.4 Missing Ratio (MR)

The Missing Ratio (MR) for the rainfall event during the period 2011 to 2021 during winter season over Delhi is depicted in the Figure 11. In the year 2011 and 2012 Missing Ratio (MR) of a rainfall event was around 0.20. In the year 2013 Missing Ratio (MR) was very high value 0.65, which has decreased to 0.0 in the year 2020. Thus, the Missing Ratio (MR) of an event for Delhi has decreased by 0.65 in last 7 years. It shows that there is significant decrement in the Missing Ratio (MR) after 2013. In the winter season of the year 2021 MR is increased to 0.25 as compared to 2020. Reason for this increase in MR is that

in February 2021 there were only two rainy days, out of which one was predicted correctly and other was missed. Normally 6-7 rainy days are realised in each month of January and February. Missing ratio for January 2021 is 0.0, for February 2021 is 0.50 and overall for winter season (2021) is 0.25.

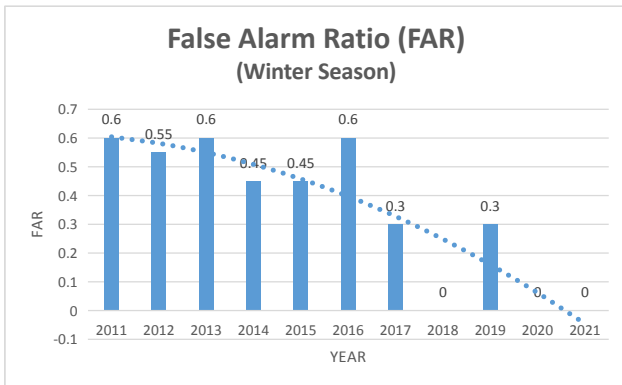


Figure 10. False Alarm Ratio (FAR) for Forecast of Delhi during winter Season (2011 – 2021)

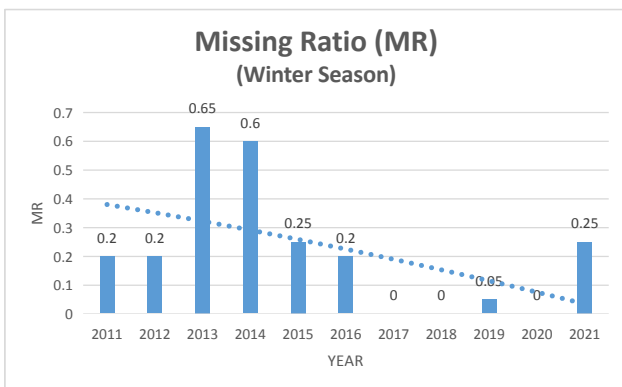


Figure 11. Missing Ratio (MR) for Forecast of Delhi during winter Season (2011 – 2021)

#### 4.2.5 Critical Success Index (CSI)

Figure 12 depicts the Critical Success Index (CSI) for the forecast during the period 2011 to 2021 during winter season over Delhi. In the year 2011 and 2012 Critical Success Index (CSI) was 0.35. In the year 2013 Critical Success Index (CSI) was decreased to 0.25, which has increased to 1.0 in the year 2018 and 2020. Thus, the Critical Success Index (CSI) for the forecast of an event for Delhi has significantly increased by 0.65 in last 8 years. It shows that there is significant improvement in the Critical Success Index (CSI) for the weather forecast after 2013. In the winter season of the year 2021 CSI is decreased to 0.75 as compared to 2020. Reason for this decrease in CSI is that in February 2021 there were only two rainy days, out of which one was predicted correctly and other

was missed. Normally 6-7 rainy days are realised in each month of January and February. CSI for January 2021 is 1.0, for February 2021 is 0.50 and overall, for winter season (2021) is 0.75.

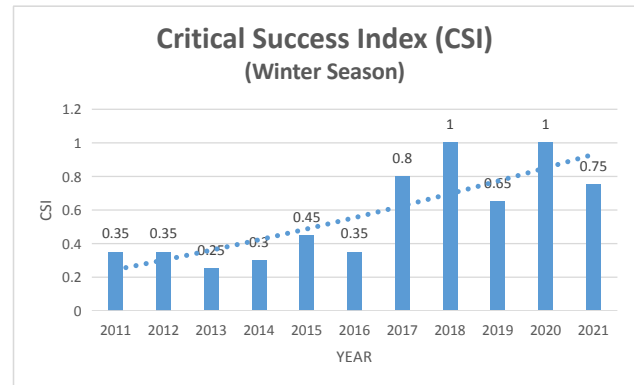


Figure 12. Critical Success Index (CSI) for Forecast of Delhi during winter Season (2011 – 2021)

#### 4.2.6 True Skill Statistics (TSS)

Figure 13 depicts the True Skill Statistics (TSS) for the forecast during the period 2011 to 2021 over Delhi. In the year 2011 and 2012 True Skill Statistics (TSS) were 0.65 and 0.70 respectively. In the year 2013 and 2014 True Skill Statistics (TSS) was decreased significantly to 0.25, which has increased to 1.0 in the year 2020 as compared to year 2013. Thus, the True Skill Statistics (TSS) for the forecast of an event for Delhi has significantly increased by 0.75 in last 7 years. It shows that there is significant increase in the True Skill Statistics (TSS) for the weather forecast after 2013. In the winter season of the year 2021 TSS is decreased to 0.75 as compared to 2020. Reason for this decrease in TSS is that in February 2021 there were only two rainy days, out of which one was predicted correctly and other was missed. Normally 6-7 rainy days are realised in each month of January and February. TSS for January 2021 is 1.0, for February 2021 is 0.50 and overall for winter season (2021) is 0.75.

#### 4.2.7 Heidke Skill Score (HSS)

Figure 14 depicts the Heidke Skill Score (HSS) for the forecast during the period 2011 to 2021 over Delhi. In the year 2011 and 2012 Heidke Skill Score (HSS) were 0.45 and 0.50 respectively. In the year 2013 Heidke Skill Statistics (HSS) was decreased significantly to 0.20, which has increased to 1.0 in the year 2020. Thus, the Heidke Skill Statistics (HSS) for the forecast of an event for Delhi has significantly increased by 0.8 in last 7 years. It shows that there is significant increase in the Heidke Skill Statistics (HSS) for the weather forecast after 2013. In the win-

ter season of the year 2021 HSS is decreased to 0.75 as compared to 2020. Reason for this decrease in HSS is that in February 2021 there were only two rainy days, out of which one was predicted correctly and other was missed. Normally 6-7 rainy days are realised in each month of January and February. HSS for January 2021 is 0.0, for February 2021 is 0.50 and overall for winter season (2021) is 0.75.

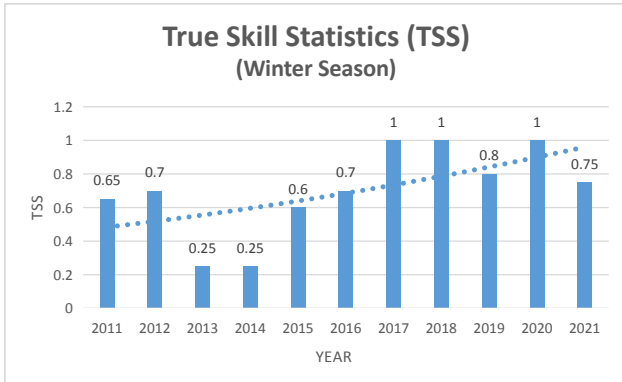


Figure 13. True Skill Statistics (TSS) for Forecast of Delhi during winter Season (2011 – 2021)

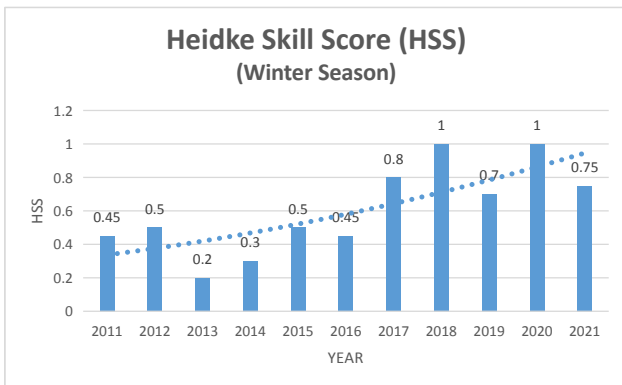


Figure 14. Heidke Skill Score (HSS) for Forecast of Delhi during winter Season (2011 – 2021)

Above analysis of PC, POD, FAR, MR, CSI, TSS and HSS for the winter season forecast verification for Delhi depicts that PC was higher in the year 2011 and 2012 and again in 2021. But the major difference in these years is that in the year 2020, POD and CSI have significantly increased and reached up to 1.0. TSS and HSS also increased significantly in the year 2020 and both reached up to 1.0. Simultaneously FAR and MR have significantly decreased up to 0.0 in the year 2020.

In the year 2021 PC, POD, FAR, MR, CSI, TSS and HSS values were 98%, 0.75, 0.0, 0.25, 0.75, 0.75 and 0.75 respectively. Decrease in POD, CSI, TSS and HSS and increase in MR for the year 2021 is due to the reason that in February 2021 there were only two rainy days, out of

which one was predicted correctly and other was missed. Normally 6-7 rainy days are realised in each month of January and February.

Thus, significant increase in the PC, POD, CSI, TSS and HSS and significant decrease in FAR and MR has been noticed in last few years. A forecast is assumed to be improving if PC, POD, CSI, TSS and HSS increases and FAR and MR decreases over a period of time. In this case there is increasing trend in PC, POD, CSI, TSS and HSS while decreasing trend in FAR and MR. This shows that there is significant improvement trend in the forecast during 2011 to 2021.

### 4.3 Verification of Forecast for Pre-monsoon Season

#### 4.3.1 Percentage Correct (PC)

Figure 15 depicts the percentage correct (PC) forecast during the period 2011 to 2021 for pre-monsoon Season over Delhi. In the year 2011 and 2012 percentage correct forecast were 90% and 88% respectively with False Alarm Ratio (FAR) around 0.23 and 0.37 respectively (Figure 17). Trend in Percentage forecast continue to decrease till year 2016, after that it has increasing trend and reached up to 92% in the year 2021 with FAR is 0.20. On comparing year 2011 and year 2021 there is slight increase of 2% in PC and slight decrease of 0.3 in FAR. Thus, the accuracy of forecast for Delhi for pre-monsoon Season has increased by 13% in last 8 years. It shows that there is significant improvement in the accuracy of forecast after 2013.

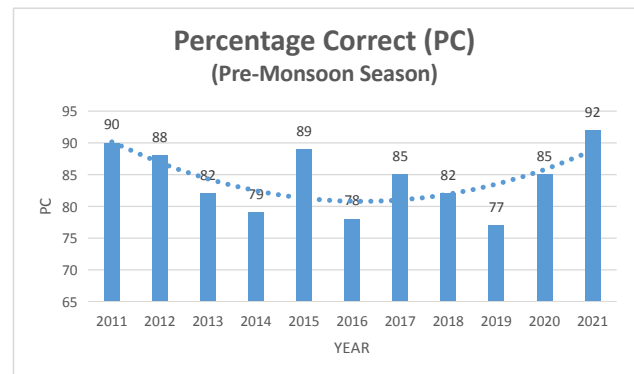


Figure 15. Percentage Correct (PC) for Forecast of Delhi during pre-monsoon Season (2011 – 2021)

#### 4.3.2 Probability of Detection (POD)

The Probability of Detection (POD) for the rainfall event during the period 2011 to 2021 for pre-monsoon Season over Delhi is shown in the Figure 16. In the year 2011 and 2012 Probability of Detection (POD) of a rain-

fall event was 0.73 and 0.63. In the year 2013 Probability of Detection (POD) was 0.30 which was lowest during the period 2011-2021; POD has increased to 0.97 in the year 2021. Thus, the Probability of Detection (POD) for Delhi has increased by 0.67 in last 8 years. It shows that there is significant improvement in the Probability of Detection (POD) of an event after 2013.

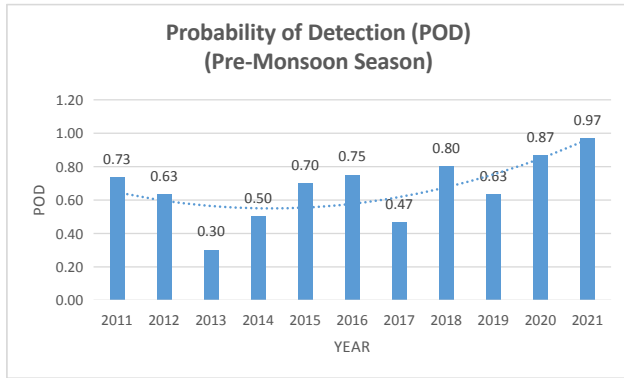


Figure 16. Probability of Detection (POD) for Forecast of Delhi during pre-monsoon Season (2011 – 2021)

#### 4.3.3 False Alarm Ratio (FAR)

Figure 17 illustrates the False Alarm Ratio (FAR) for the rainfall event during the period 2011 to 2021 for pre-monsoon Season over Delhi. In the year 2011 and 2012 False Alarm Ratio (FAR) of a rainfall event was 0.23 and 0.37 respectively. In the year 2013 False Alarm Ratio (FAR) was very high value 0.65, which has decreased to 0.20 in the year 2021. Thus, the False Alarm Ratio (FAR) for Delhi has decreased by 0.45 in last 8 years. It shows that there is significant decrement in the False Alarm Ratio (FAR) after 2013.

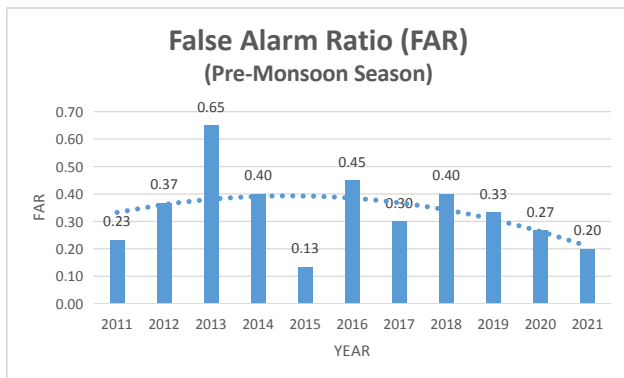


Figure 17. False Alarm Ratio (FAR) for Forecast of Delhi during pre-monsoon Season (2011 – 2021)

#### 4.3.4 Missing Ratio (MR)

The Missing Ratio (MR) for the rainfall events during

the period 2011 to 2021 for pre-monsoon Season over Delhi are depicted in the Figure 18. In the year 2011 and 2012 Missing Ratio (MR) of a rainfall event was 0.27 and 0.37 respectively. In the year 2013 Missing Ratio (MR) was very high value 0.80, which has decreased to 0.03 in the year 2021. Thus, the Missing Ratio (MR) of an event for Delhi has decreased by 0.77 in last 8 years. It shows that there is significant decrement in the Missing Ratio (MR) after 2013.

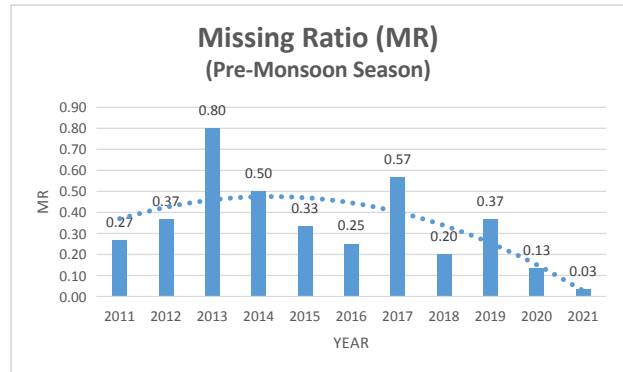


Figure 18. Missing Ratio (MR) for Forecast of Delhi during pre-monsoon Season (2011 – 2021)

#### 4.3.5 Critical Success Index (CSI)

Figure 19 depicts the Critical Success Index (CSI) for the forecast during the period 2011 to 2021 for pre-monsoon Season over Delhi. In the year 2011 and 2012 Critical Success Index (CSI) was 0.60 and 0.40 respectively. In the year 2013 Critical Success Index (CSI) was decreased to 0.15, which has increased to 0.80 in the year 2021. Thus, the Critical Success Index (CSI) for the forecast of an event for Delhi has significantly increased by 0.65 in last 8 years. It shows that there is significant improvement in the Critical Success Index (CSI) for the weather forecast after 2013.

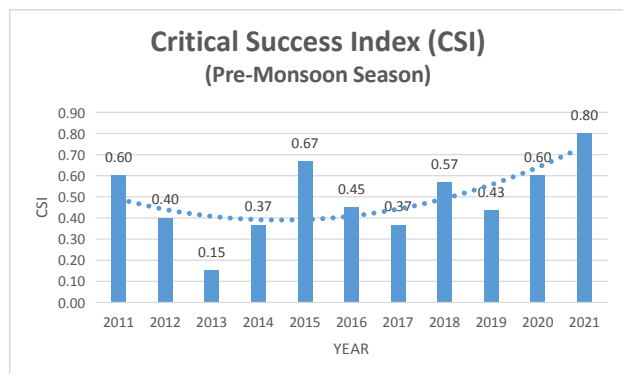


Figure 19. Critical Success Index (CSI) for Forecast of Delhi during pre-monsoon Season (2011 – 2021)

### 4.3.6 True Skill Statistics (TSS)

Figure 20 depicts the True Skill Statistics (TSS) for the forecast during the period 2011 to 2021 for pre-monsoon Season over Delhi. In the year 2011 and 2012 True Skill Statistics (TSS) was 0.67 and 0.60 respectively. In the year 2013 True Skill Statistics (TSS) was decreased significantly to 0.15, which has increased to 0.87 in the year 2021. Thus, the True Skill Statistics (TSS) for the forecast of the rainfall events for Delhi has significantly increased by 0.72 in last 8 years. It shows that there is a significant increase in the True Skill Statistics (TSS) for the weather forecast after 2013.

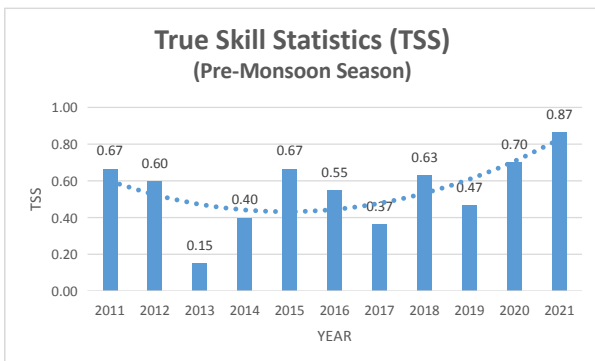


Figure 20. True Skill Statistics (TSS) for Forecast of Delhi during pre-monsoon Season (2011 – 2021)

### 4.3.7 Heidke Skill Score (HSS)

Figure 21 depicts the Heidke Skill Score (HSS) for the forecast during the period 2011 to 2021 for pre-monsoon Season over Delhi. In the year 2011 and 2012 Heidke Skill Score (HSS) were 0.67 and 0.50 respectively. In the year 2013 Heidke Skill Score (HSS) was decreased significantly to 0.20, which has increased to 0.83 in the year 2021. Thus, the Heidke Skill Score (HSS) for the forecast of an event for Delhi has significantly increased by 0.63 in last 8 years. It shows that there is significant increase in the Heidke Skill Score (HSS) for the weather forecast after 2013.

Above analysis of PC, POD, FAR, MR, CSI, TSS and HSS for the forecast verification for pre-monsoon Season for Delhi depicts that PC was higher in the year 2011, 2012, 2015 and again in 2021. But the major difference in these years is that in the year 2021, POD and CSI have significantly increased and reached up to 0.97 and 0.80 respectively. TSS and HSS also increased significantly in the year 2021 and both reached up to 0.87 and 0.83. Simultaneously FAR and MR have also shown decreasing trend and decreased up to 0.20 and 0.03 respectively.

Thus, significant increase in the PC, POD, CSI, TSS

and HSS and significant decrease in FAR and MR has been noticed in last 8 years. A forecast is assumed to be improving if PC, POD, CSI, TSS and HSS increases and FAR and MR decreases over a period of time. In this case there is increasing trend in PC, POD, CSI, TSS and HSS while decreasing trend in FAR and MR. This shows that there is significant improvement in the forecast during 2013 to 2021.

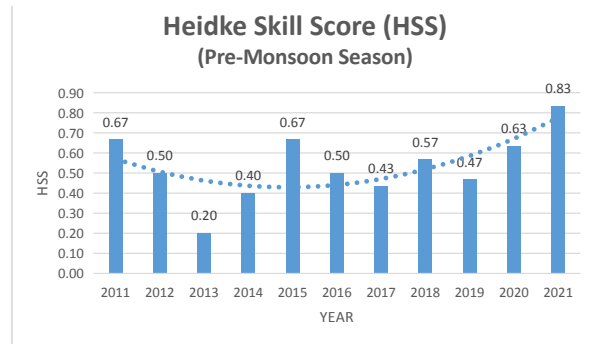


Figure 21. Heidke Skill Score (HSS) for Forecast of Delhi during pre-monsoon Season (2011 – 2021)

## 4.4 Verification of Forecast for Monsoon Season

### 4.4.1 Percentage Correct (PC)

Figure 22 depicts the percentage correct (PC) forecast during the period 2011 to 2021 for monsoon Season over Delhi. In the year 2011 and 2012 percentage correct forecast were 80% and 92% respectively with False Alarm Ratio (FAR) 0.1 in both the years (Figure 24). Decreasing trend in Percentage forecast is observed till year 2013, after that it has increasing trend and reached up to 87% in the year 2021 with FAR is 0.2. On comparing year 2011 and year 2021 there is increase of 7% in PC and slight increase of 0.1 in FAR. Thus, the accuracy of forecast for Delhi for pre-monsoon Season has increased by 20% in last 8 years. It shows that there is improvement in the accuracy of forecast after 2013.

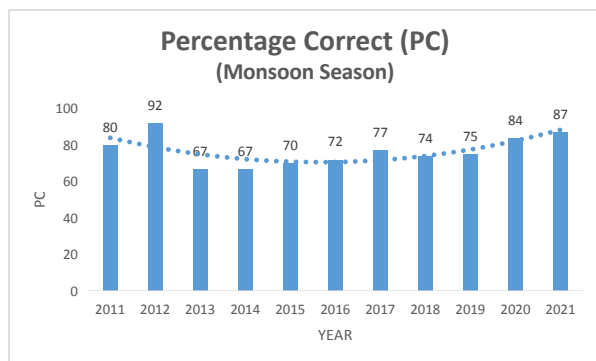


Figure 22. Percentage Correct (PC) for Forecast of Delhi during monsoon Season (2011 – 2021)

#### 4.4.2 Probability of Detection (POD)

The Probability of Detection (POD) for the rainfall event during the period 2011 to 2021 for monsoon Season over Delhi is shown in the Figure 23. In the year 2011 and 2012 Probability of Detection (POD) of a rainfall event was 0.80 and 1.0 respectively. In the year 2013 Probability of Detection (POD) was 0.70 which was lowest during the period 2011-2021; POD in the year 2021 was 0.9. Thus, the Probability of Detection (POD) for monsoon season over Delhi remains close to 0.9 during the period 2011-2021. It shows that there is no large change in the Probability of Detection (POD) of the rainfall in the monsoon season during the study period. The main reason for no large change is that monsoon season is the main rainy season and rainfall occur often, and is well predicted

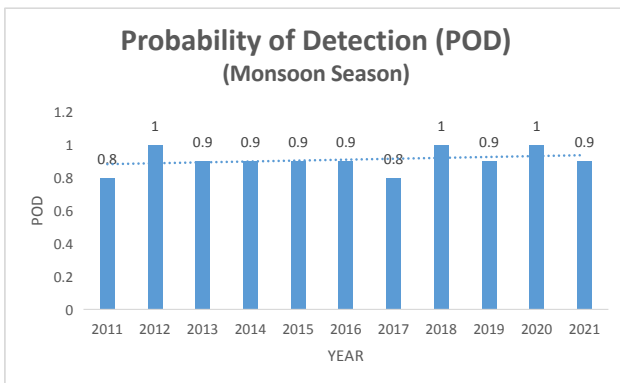


Figure 23. Probability of Detection (POD) for Forecast of Delhi during monsoon Season (2011 – 2021)

#### 4.4.3 False Alarm Ratio (FAR)

Figure 24 illustrates the False Alarm Ratio (FAR) for the rainfall event during the period 2011 to 2021 for the monsoon Season over Delhi. For both In the year 2011 and 2012 False Alarm Ratio (FAR) of the rainfall was 0.1. In the year 2013 False Alarm Ratio (FAR) was very high value 0.7, which has decreased to 0.20 in the year 2021. Thus, the False Alarm Ratio (FAR) for Delhi has decreased by 0.50 in last 8 years. It shows that there is significant decrement in the False Alarm Ratio (FAR) after 2013.

#### 4.4.4 Missing Ratio (MR)

The Missing Ratio (MR) for the rainfall events during the period 2011 to 2021 for the monsoon Season over Delhi are depicted in the Figure 25. In the year 2011, 2014 and 2017 Missing Ratio (MR) of a rainfall event was 0.20. Rest of the years of the period 2011 to 2021, MR is either 0.0 or 0.1. Thus, MR is very low during monsoon season.

Overall trend line shows that MR is further decreasing over the years. Reason for decreasing and low values of MR is that rainfall pattern and associated synoptic and atmospheric conditions are well understood during monsoon season.

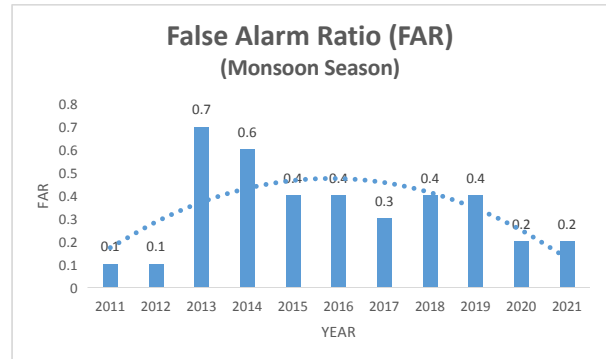


Figure 24. False Alarm Ratio (FAR) for Forecast of Delhi during monsoon Season (2011 – 2021)

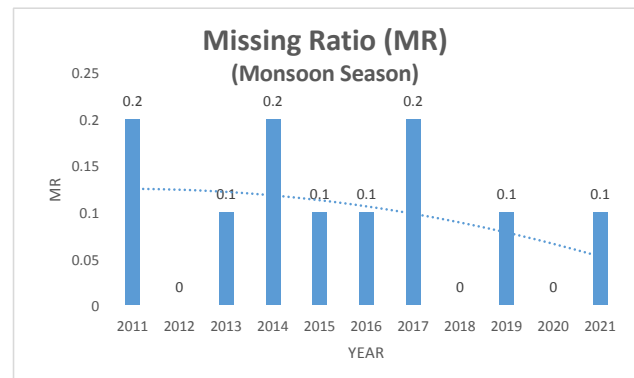


Figure 25. Missing Ratio (MR) for Forecast of Delhi during monsoon Season (2011 – 2021)

#### 4.4.5 Critical Success Index (CSI)

Figure 26 depicts the Critical Success Index (CSI) for the forecast during the period 2011 to 2021 for monsoon Season over Delhi. In the year 2011 and 2012 Critical Success Index (CSI) was 0.70 and 0.90 respectively. In the year 2014 Critical Success Index (CSI) was decreased to 0.4, which has increased to 0.80 in the year 2021. Thus, the Critical Success Index (CSI) for the forecast of rainfall for Delhi has significantly increased by 0.4 in last 7 years. It shows that there is significant improvement in the Critical Success Index (CSI) for the rainfall forecast after 2014.

#### 4.4.6 True Skill Statistics (TSS)

Figure 27 depicts the True Skill Statistics (TSS) for the forecast during the period 2011 to 2021 for monsoon Season over Delhi. In the year 2011 and 2012 True Skill

Statistics (TSS) was 0.5 and 0.70 respectively. In the year 2013 True Skill Statistics (TSS) was decreased significantly to 0.2, which has increased to 0.6 in the year 2021. Thus, the True Skill Statistics (TSS) for the forecast of the rainfall events for Delhi has significantly increased by 0.4 in last 8 years. It shows that there is significant increase in the True Skill Statistics (TSS) for the weather forecast after 2013.

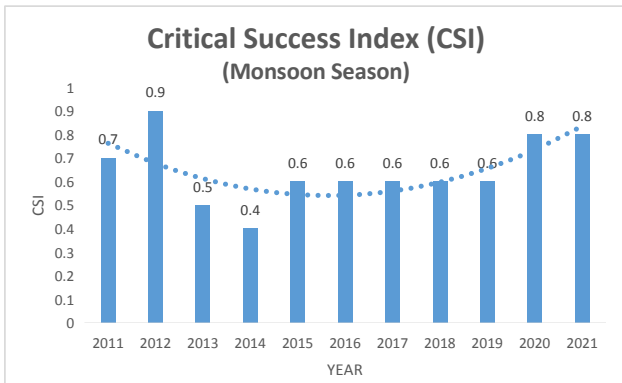


Figure 26. Critical Success Index (CSI) for Forecast of Delhi during monsoon Season (2011 – 2021)

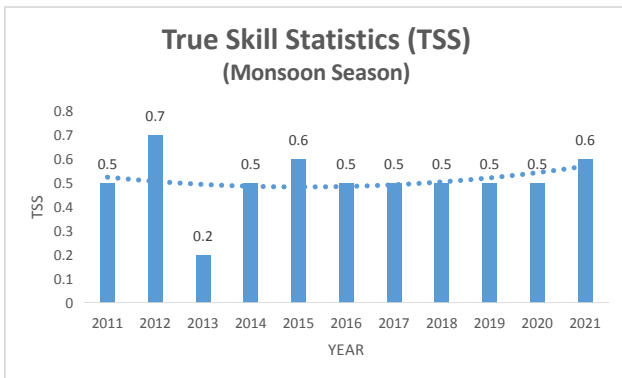


Figure 27. True Skill Statistics (TSS) for Forecast of Delhi during monsoon Season (2011 – 2021)

#### 4.4.7 Heidke Skill Score (HSS)

Figure 28 depicts the Heidke Skill Score (HSS) for the forecast during the period 2011 to 2021 for monsoon Season over Delhi. In the year 2011 and 2012 Heidke Skill Score (HSS) was 0.5 and 0.8 respectively. In the year 2013 Heidke Skill Score (HSS) was decreased significantly to 0.30, which has again increased to 0.6 in the year 2021. Thus, the Heidke Skill Score (HSS) for the forecast of an event for Delhi has significantly increased by 0.30 in last 7 years. It shows that there is significant increase in the Heidke Skill Score (HSS) for the weather forecast after 2014.

Above analysis of PC, POD, FAR, MR, CSI, TSS and HSS for the forecast verification for monsoon Season for Delhi depicts that PC was higher (>80%) in the year 2011, 2012, 2020 and 2021. Above analysis for monsoon season shows that POD is almost similar for the study period. However, trend line of POD indicates slight increase in POD. FAR has decreased significantly after 2013. Trend line of MR is indicating decrease in MR over the years. Trend line of CSI, TSS and HSS shows increasing trend after 2013. Reason for gradual decreasing trend of MR and gradual increasing trend of CSI, TSS and HSS is that during monsoon season rainfall occurs often and also rainfall pattern and associated synoptic and atmospheric conditions are well understood for monsoon season. This shows that there is gradual improvement in the forecast during 2013 to 2021 in monsoon season.

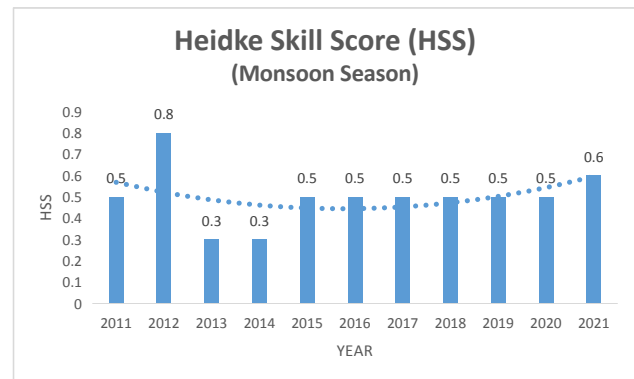


Figure 28. Heidke Skill Score (HSS) for Forecast of Delhi during monsoon Season (2011 – 2021)

### 4.5 Verification of Forecast for Post-monsoon Season

#### 4.5.1 Percentage Correct (PC)

Figure 29 depicts the percentage correct (PC) forecast during the period 2011 to 2021 for post-monsoon Season over Delhi. In the year 2011 and 2012 percentage correct forecast were 99% and 96% respectively with False Alarm Ratio (FAR) around 0.30 and 0.40 respectively (Figure 31). Trend in Percentage forecast continue to decrease till year 2013, after that it has increasing trend and reached up to 100% and 98% in the year 2020 and 2021 with FAR is 0.0 and 0.05 respectively. On comparing year 2011 and year 2021 PC is almost similar, however significant decrease of 0.30 in FAR is seen. Thus, the accuracy of forecast for Delhi for post-monsoon Season has increased considerably with significant decrease in FAR during last 8 years.

#### 4.5.2 Probability of Detection (POD)

The Probability of Detection (POD) for the rainfall

event during the period 2011 to 2021 for post-monsoon Season over Delhi is shown in the Figure 30. In the year 2011 and 2012 Probability of Detection (POD) of a rainfall event was 1.0 and 0.80. In the year 2013 Probability of Detection (POD) was 0.45 which was lowest during the period 2011-2021; POD has increased to 1.0 and 0.95 in the year 2020 and 2021 respectively. Thus, the Probability of Detection (POD) for Delhi has increased by 0.50 in last 8 years. It shows that there is significant improvement in the Probability of Detection (POD) of an event after 2013.

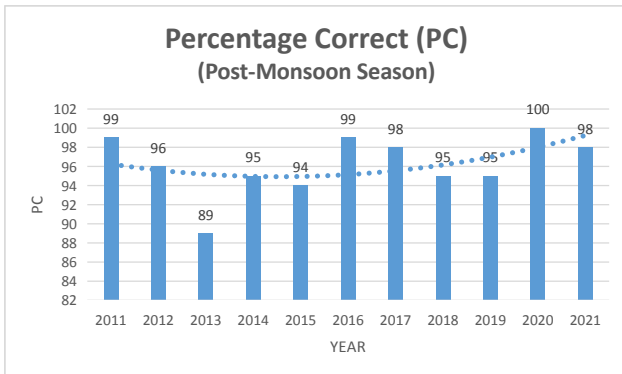


Figure 29. Percentage Correct (PC) for Forecast of Delhi during post-monsoon Season (2011 – 2021)

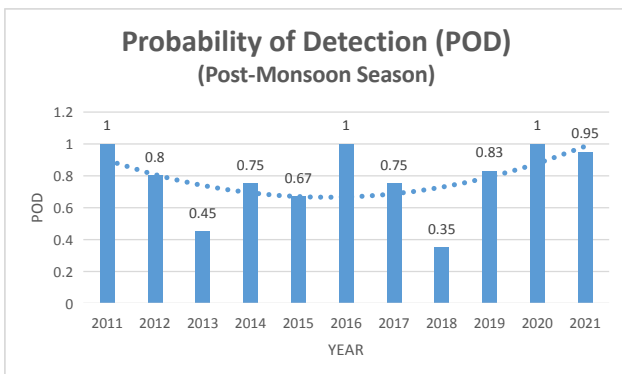


Figure 30. Probability of Detection (POD) for Forecast of Delhi during post-monsoon Season (2011 – 2021)

#### 4.5.3 False Alarm Ratio (FAR)

Figure 31 illustrates the False Alarm Ratio (FAR) for the rainfall event during the period 2011 to 2021 for post-monsoon Season over Delhi. In the year 2011 and 2012 False Alarm Ratio (FAR) of a rainfall event was 0.30 and 0.40 respectively. In the year 2013 and 2014 False Alarm Ratio (FAR) was very high value 0.55, which has decreased to 0.05 in the year 2021. Thus, the False Alarm Ratio (FAR) for Delhi has decreased by 0.50 in last 8 years. Trend line also shows that FAR is decreasing continuously. It shows that there is significant decrement in the False Alarm Ratio (FAR) after 2013.

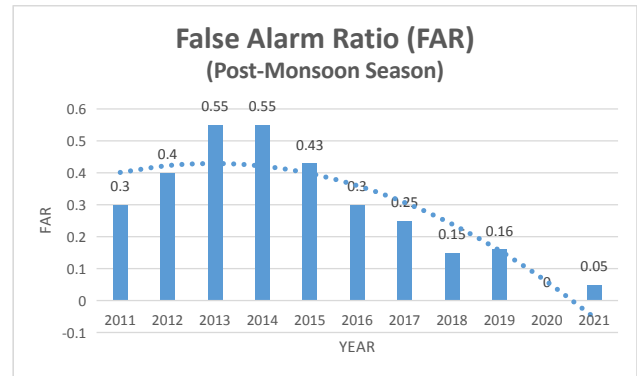


Figure 31. False Alarm Ratio (FAR) for Forecast of Delhi during post-monsoon Season (2011 – 2021)

#### 4.5.4 Missing Ratio (MR)

The Missing Ratio (MR) for the rainfall events during the period 2011 to 2021 for pre-monsoon Season over Delhi is depicted in the Figure 32. In the year 2011 and 2012 Missing Ratio (MR) of a rainfall event was 0.0 and 0.30 respectively. In the year 2013 Missing Ratio (MR) was very high value 0.60, which has decreased to 0.0 and 0.05 in the year 2020 and 2021 respectively. Thus, the Missing Ratio (MR) of an event for Delhi has decreased by 0.55 in last 8 years. Trend line also shows that MR is decreasing continuously. It shows that there is significant decrement in the Missing Ratio (MR) after 2013.

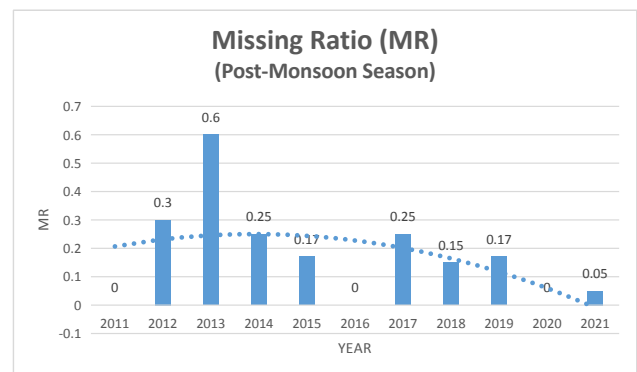
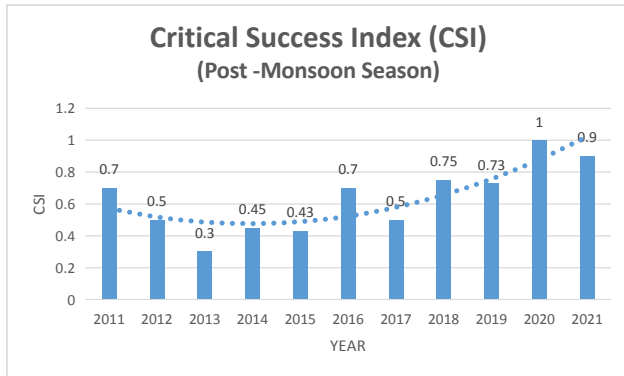


Figure 32. Missing Ratio (MR) for Forecast of Delhi during post-monsoon Season (2011 – 2021)

#### 4.5.5 Critical Success Index (CSI)

Figure 33 depicts the Critical Success Index (CSI) for the forecast during the period 2011 to 2021 for post-monsoon Season over Delhi. In the year 2011 and 2012 Critical Success Index (CSI) was 0.70 and 0.50 respectively. In the year 2013 Critical Success Index (CSI) was decreased to 0.3, which has increased to 1.0 and 0.90 in the year 2020 and 2021 respectively. Thus, the Critical Success Index (CSI) for the forecast of an event for Delhi has sig-

nificantly increased by 0.60 in last 8 years. Trend line also shows that CSI is increasing continuously. It shows that there is significant improvement in the Critical Success Index (CSI) for the weather forecast after 2013. Trend line also shows that CSI is increasing continuously.



**Figure 33.** Critical Success Index (CSI) for Forecast of Delhi during post-monsoon Season (2011 – 2021)

#### 4.5.6 True Skill Statistics (TSS)

Figure 34 depicts the True Skill Statistics (TSS) for the forecast during the period 2011 to 2021 for post-monsoon Season over Delhi. In the year 2011 and 2012 True Skill Statistics (TSS) was 1.0 and 0.70 respectively. In the year 2013 True Skill Statistics (TSS) was decreased significantly to 0.35, which has increased to 1.0 and 0.90 in the year 2020 and 2021 respectively. Thus, the True Skill Statistics (TSS) for the forecast of the rainfall events for Delhi has significantly increased by 0.55 in last 8 years. Trend line also shows that TSS is increasing continuously. It shows that there is significant increase in the True Skill Statistics (TSS) for the weather forecast after 2013.

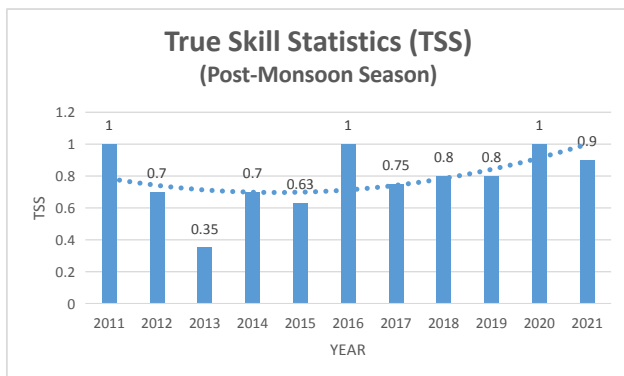


**Figure 34.** True Skill Statistics (TSS) for Forecast of Delhi during post-monsoon Season (2011 – 2021)

#### 4.5.7 Heidke Skill Score (HSS)

Figure 35 depicts the Heidke Skill Score (HSS) for the

forecast during the period 2011 to 2021 for post-monsoon Season over Delhi. In the year 2011 and 2012 Heidke Skill Score (HSS) were 0.80 and 0.60 respectively. In the year 2013 Heidke Skill Score (HSS) was decreased significantly to 0.35, which has increased to 1.0 and 0.90 in the year 2020 and 2021 respectively. Thus, the Heidke Skill Score (HSS) for the forecast of an event for Delhi has significantly increased by 0.55 in last 8 years. Trend line also shows that HSS is increasing continuously. It shows that there is significant increase in the Heidke Skill Score (HSS) for the weather forecast after 2013.

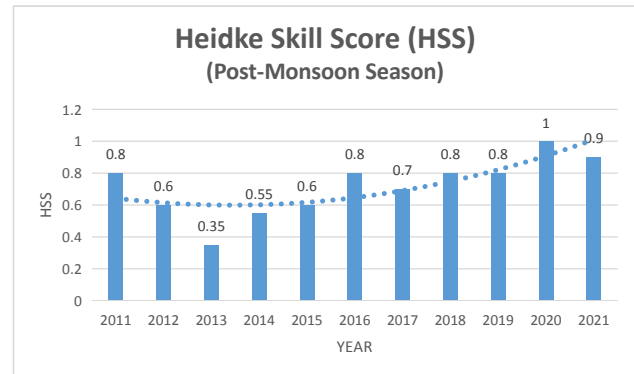


**Figure 35.** Heidke Skill Score (HSS) for Forecast of Delhi during post-monsoon Season (2011 – 2021)

Above analysis of PC, POD, FAR, MR, CSI, TSS and HSS for the forecast verification for post-monsoon Season for Delhi depicts that PC was higher (>95%) in all the year expect 2013 when it was 89%. CSI, TSS and HSS also increased significantly during the period 2013-2021 reached up to 1.0 and 0.90 in the year 2020 and 2021 respectively. Simultaneously FAR and MR has also shown significant decreasing trend and decreased up to 0.0 and 0.05 in the year 2020 and 2021 respectively.

Thus, significant increase in the CSI, TSS and HSS and significant decrease in FAR and MR has been noticed in last 8 years. A forecast is assumed to be improving if PC, POD, CSI, TSS and HSS increases and FAR and MR decreases over a period of time. In this case there is increasing trend in CSI, TSS and HSS while decreasing trend in FAR and MR. This shows that there is significant improvement in the forecast during 2013 to 2021 for the post-monsoon Season.

## 5. Conclusions

In this study rainfall forecast verification of Delhi for the period 2011 to 2021 has been carried out. Various statistical parameters such as Percentage Correct (PC), Probability of Detection (POD), Missing Ratio (MR), False Alarm Ratio (FAR), Critical Success Index (CSI), True Skill Statistics (TSS) and Heidke Skill Score (HSS) has

been calculated for season wise and annually. A forecast is assumed to be improving if PC, POD, CSI, TSS and HSS increases and FAR and MR decreases over a period of time. Based on the values of these parameters following conclusion are drawn:

**Annual:** The analysis of various parameters calculated annually depicts that PC was higher in the year 2011 and 2012 and again in 2021. But the major difference in these years (2011-2021) is that in the year 2021, POD, CSI, TSS and HSS has significantly increased and reached up to 0.91, 0.81, 0.79 and 0.79 respectively. Simultaneously FAR and MR has significantly decreased up to 0.13 and 0.9 respectively. This shows that there is significant improvement in the forecast during 2011 to 2021.

**Winter:** Analysis of various parameters for the winter season depicts that PC was higher in the year 2011 and 2012 and again in 2021. But the major difference in these years is that in the year 2020, POD and CSI have significantly increased and reached up to 1.0. TSS and HSS also increased significantly in the year 2020 and both reached up to 1.0. Simultaneously FAR and MR has significantly decreased up to 0.0 in the year 2020. Thus, there is increasing trend in PC, POD, CSI, TSS and HSS while decreasing trend in FAR and MR. This shows that there is significant improvement in the forecast for winter season during 2011 to 2021.

**Pre-Monsoon:** Analysis of various parameters pre-monsoon Season depicts that PC was higher in the year 2011, 2012, 2015 and again in 2021. But the major difference in these years is that in the year 2021, POD and CSI have significantly increased and reached up to 0.97 and 0.80 respectively. TSS and HSS also increased significantly in the year 2021 and both reached up to 0.87 and 0.83. Simultaneously FAR and MR have also shown decreasing trend and decreased up to 0.20 and 0.03 respectively. For pre monsoon season there is increasing trend in PC, POD, CSI, TSS and HSS while decreasing trend in FAR and MR. This shows that there is significant improvement in the forecast during 2013 to 2021.

**Monsoon:** Analysis for monsoon season shows that POD is almost similar for the study period. However, trend line of POD indicates slight increase in POD. FAR has decreased significantly after 2013. Trend line of MR is indicating decrease in MR over the years. Trend line of CSI, TSS and HSS shows increasing trend after 2013. Reason for gradual decreasing trend of MR and gradual increasing trend of CSI, TSS and HSS is that during monsoon season rainfall occurs often and also rainfall pattern and associated synoptic and atmospheric conditions are well understood for monsoon season. This shows that there is gradual improvement in the forecast during 2013

to 2021 in monsoon season.

**Post Monsoon:** Analysis of post-monsoon Season for Delhi depicts that PC was higher (>95%) in all the year expect 2013 when it was 89%. CSI, TSS and HSS also increased significantly during the period 2013-2021 reached up to 1.0 and 0.90 in the year 2020 and 2021 respectively. Simultaneously FAR and MR has also shown significant decreasing trend and decreased up to 0.0 and 0.05 in the year 2020 and 2021 respectively. There is increasing trend in CSI, TSS and HSS while decreasing trend in FAR and MR. This shows that there is significant improvement in the forecast during 2013 to 2021 for the post-monsoon Season.

Overall, we can conclude that annually accuracy of forecast has increase significantly during last 8 years. Maximum contribution in the improved forecast has observed in transition season (pre-monsoon season followed by post-monsoon), when FAR and MR has decreased drastically. We can also say accuracy of prediction of rainfall associated with thunderstorms has also increased, as in pre and post monsoon season rainfall activities occurs mainly in association with thunderstorms. The increase in forecast accuracy is mainly attributed to the availability of Doppler weather Radar and satellite images at frequent interval, increased accuracy of Numerical Weather Prediction Models and increased understanding of forecasters.

## Author Contributions

Author is Head of Regional Weather Forecasting Center, New Delhi since 2017 and looks after day to day forecasting activities of Delhi as well as North-west India. Author has significant contributions in writing this research paper.

## Conflict of Interest

Author has no conflicts of interest to disclose.

## Acknowledgements

The author is thankful to Director General of Meteorology (DGM), India Meteorological Department (IMD), New Delhi and Deputy Director General of Meteorology (DDGM), RMC New Delhi for rendering all the facilities. The author is also thankful to officials of RWFC for collection and providing the data for such a long period. The author also gratefully acknowledges Regional Weather Forecasting Centre (RWFC) for providing daily weather forecast data and Safdarjung, IGI Palam, Aayanagar, Ridge and Lodi Road observatories for providing the rainfall data.

## References

- [1] Casati, B., Wilson, L.J., Stephenson, D.B., et al., 2008. Forecast verification: current status and future directions. *Meteorological Applications*. 15(1), 3-18. DOI: <https://doi.org/10.1002/met.52>
- [2] Mason, S.J., 2008. Understanding forecast verification statistics. *Meteorological Applications*. 15(1), 31-40. DOI: <https://doi.org/10.1002/met.51>
- [3] Nurmi, P., 2003. Recommendations on the verification of local weather forecasts. DOI: <https://doi.org/10.21957/y1z1thg51>
- [4] Murphy, A.H., 1993. What is a good forecast? An essay on the nature of goodness in weather forecasting. *Weather and Forecasting*. 8(2), 281-293. DOI: [https://doi.org/10.1175/1520-0434\(1993\)008<0281:WIAGFA>2.0.CO;2](https://doi.org/10.1175/1520-0434(1993)008<0281:WIAGFA>2.0.CO;2)
- [5] Hitchens, N. M., Brooks, H. E., Kay, M. P. , 2013. Objective limits on forecasting skill of rare events. *Weather and forecasting*, 28(2), 525-534. DOI: <https://doi.org/10.1175/WAF-D-12-00113.1>
- [6] Srivastava, K., Nigam, A., 2020. Rainfall estimation using image processing and regression model on DWR rainfall product for Delhi-NCR region. *Journal of Atmospheric Science Research*. 3 (1), 9-15. DOI: <https://doi.org/10.30564/jasr.v3i1.1859>
- [7] Doswell, C. A. III, Davies-Jones, R., and Keller, D. L., 1990. On summary measures of skill in rare event forecasting based on contingency tables. *Weather and Forecasting*. 5(4), 576–585.

ARTICLE

## Experimental Simulation of Red Sprites in a Laboratory

Victor Tarasenko\* Nikita Vinogradov Evgenii Baksht Dmitry Sorokin

Laboratory of Optical Radiations, Institute of High Current Electronics SB RAS, Tomsk, 634055, Russia

ARTICLE INFO

*Article history*

Received: 30 June 2022

Revised: 20 July 2022

Accepted: 21 July 2022

Published: 30 July 2022

*Keywords:*

Red sprites

Experimental modeling

Streamer discharge in air

Low pressures

ABSTRACT

Over the past three decades, research of high-altitude atmospheric discharges has received a lot of attention. This paper presents the results of experimental modeling of red sprites during a discharge in low-pressure air. To initiate ionization waves in a quartz tube, an electrodeless pulse-periodic discharge fed by microsecond voltage pulses with an amplitude of a few kilovolts and a repetition rate of tens of kHz were formed. In this case ionization waves (streamers) have a length of tens of centimeters. The main plasma parameters were measured at various distances along the tube. The measurements confirm the fact that ionization waves propagate in opposite directions from the zone of the main electrodeless discharge, just as it happens during the formation of red sprites.

### 1. Introduction

Much attention is paid to the study of atmospheric discharges. They affect human life, and physical processes occurring in many types of these discharges still require further study. Over the past three decades, many scientific groups have intensively studied Transient Luminous Events (TLEs) such as which include red sprites, blue jets, elves, and others<sup>[1-25]</sup>. Simulations of TLEs are carried out in laboratory conditions; see for example<sup>[4,5]</sup>. Figure 1 is a widely known image<sup>[10]</sup>, which presents various types of

atmospheric discharges.

One of these types of discharges, which is initiated at altitudes of 70 km ~ 80 km from the Earth's surface and is observed above thunderclouds, are red sprites, see the first color photo<sup>[1]</sup>. They propagate at altitudes of 40 km ~ 100 km (air pressure varies within  $3\text{-}2.4\cdot 10^{-4}$  Torr) and their color can change from red to blue one at the altitude of about 50 km. It is known that red sprites can be compared with streamers (ionization waves), which, due to low pressures at high altitudes, have a length of tens of kilometers. It is believed that the red color of sprites is de-

\*Corresponding Author:

Victor Tarasenko,

Laboratory of Optical Radiations, Institute of High Current Electronics SB RAS, Tomsk, 634055, Russia;

Email: [vft@loi.hcei.tsc.ru](mailto:vft@loi.hcei.tsc.ru)

DOI: <https://doi.org/10.30564/jasr.v5i3.4858>

Copyright © 2022 by the author(s). Published by Bilingual Publishing Co. This is an open access article under the Creative Commons Attribution-NonCommercial 4.0 International (CC BY-NC 4.0) License. (<https://creativecommons.org/licenses/by-nc/4.0/>).

terminated by the emission of bands formed by spectral transitions of the first positive system (FPS; 1+) of a nitrogen molecule [3-6,9,11-13]. Important data on the radiation characteristics of sprites were obtained by observing them from an aircraft [1,23] and from space [6,24]. In particular, a glow duration, emission spectra, and propagation velocities of red sprites were measured and analyzed [1-24]. However, many of the processes that are observed during the formation of red sprites require further research, including in a laboratory. One of such properties of sprites is their propagation both towards the Earth's surface and in the opposite direction [12,17]. The mechanism for initiating red sprites also remains beyond understanding. In particular, it is assumed that their development is initiated by plasma inhomogeneities in the D-region of the ionosphere [25].

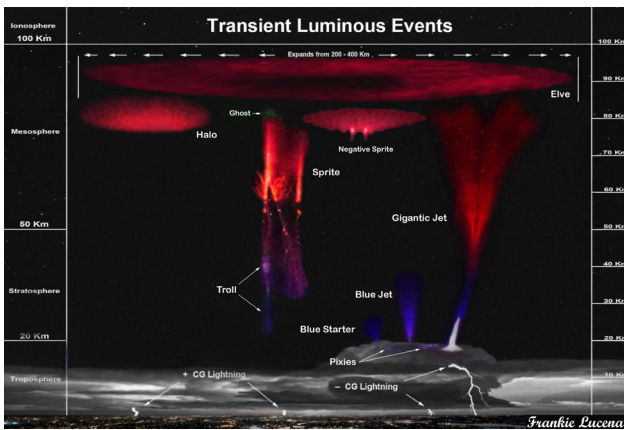


Figure 1. Different types of TLEs. Photo used with permission from F. Lucena [10]

The purpose of this work is to study in details the radiation of a plasma formed by an electrodeless pulse-periodic streamer discharge in air at pressures of 0.4 Torr ~ 9 Torr. Preliminary experiments have shown that such a discharge are red colored due to the emission of bands formed by spectral transitions of the 1+ system of a nitrogen molecule and are can be classified as a streamer discharge. This paper, unlike others dealing with laboratory modeling of red sprites in low-pressure air [15,26-31], has a significant difference in the form of an electrodeless discharge.

## 2. Experimental Setup and Measuring Techniques

For these studies, a setup was used that had two modifications, which made it possible to study the optical characteristics of a discharge plasma at air pressures corresponding to altitudes where red sprites arise. The setup consisted of a quartz tube (GE 214 grade) with the high transmission in the ultra violet (UV) and visible spectral regions equipped with 1-cm-width ring-shaped electrodes made of aluminum foil, as well as a high-frequency volt-

age pulse generator ( $U_g$ ), which was connected to them (Figure 2). A length, an inner diameter and a wall thickness of the tube were 120 cm, 50 mm and 2.5 mm, respectively. The electrodes were located in the center of the tube. A distance between the electrodes was 6 cm.

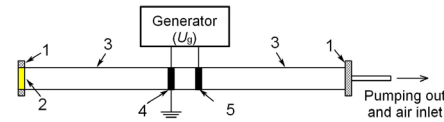


Figure 2. Experimental setup consisting of a quartz tube with ring-shaped electrodes. 1 - flanges; 2 - quartz window; 3 - quartz tube; 4, 5 - ring-shaped electrodes.

In the most experiments, the  $U_g$  generator produced voltage pulses with a rise/fall time of ~350 ns, an amplitude of 7 kV, a full width at half-maximum (FWHM) of  $\approx 2 \mu s$ . A pulse repetition rate  $f$  was 21 kHz. The ends of the tube were closed with caprolon flanges. The right flange had a 5-mm-diameter central hole that served for pumping out and filling the chamber with air. A quartz window (2 on Figure 2) or two additional pointed electrodes made of nichrome wire (A and C on Figure 3a).

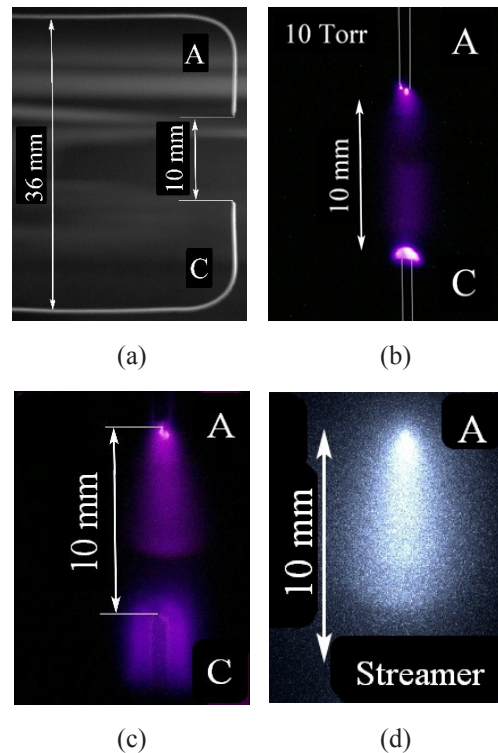


Figure 3. Integral photographs of the gap formed by two additional pointed electrodes (A and C) made of 1-mm—diameter nichrome wire (a), discharges without the streamer formation (b) and with it (c), as well as an ICCD image of a streamer (d). Air pressure is  $p = 10$  (b) and 3 Torr (c, d). Amplitude of the voltage applied across the additional pointed electrodes is  $U_{DC} = +5$  kV.

A gap width between the additional electrodes was 10 mm. A radius of curvature of these electrodes was  $\approx 0.1$  mm. DC voltage was applied across the additional electrodes from a DC voltage source ( $U_{DC}$ ) and a discharge was formed at various pressures  $p$  and voltages.

The additional electrodes and high-voltage source  $U_{DC}$  in a number of cases were used in experiments with the  $U_g$  generator and the ring-shaped electrodes. In this case, these electrodes were interconnected outside the chamber and grounded or fed by the  $U_{DC}$  source via 100 M $\Omega$  resistance. Polarities of the  $U_g$  generator and  $U_{DC}$  source could change. It was also possible to change the voltage amplitude. Note that the  $U_{DC}$  source and additional electrodes are not shown in the Figure 2, however the additional electrodes are shown in the Figure 3a. The voltage across the ring electrodes and the discharge current was measured, correspondingly, by an ACA-6039 (AKTAKOM) voltage divider and a hand-made current shunt. Signals from these probes were recorded with a MDO3104 oscilloscope (Tektronix) with a bandwidth of 1 GHz and a sampling rate of 5 GS/s. The optical characteristics of the discharge plasma radiation were measured with an A100 (SONY) digital camera, an HR2000+ES spectrometer (OceanOptics Inc.) with known spectral sensitivity characteristic, and a four-channel ICCD camera (HSFC-PRO). The HR2000+ES spectrometer (OceanOptics Inc.) allows to record a spectral energy distribution in the range of wavelengths of  $\Delta\lambda = 190$  nm  $\sim$  1100 nm. Its instrumental function is  $\Delta\lambda_{instr} \approx 0.9$  nm. In addition, to estimate the main parameters of the formed plasma, an HR4000 spectrometer (OceanOptics Inc.) with known spectral sensitivity characteristic and  $\Delta\lambda_{instr} \approx 0.2$  nm was used to record the plasma emission spectrum in the wavelength range  $\Delta\lambda = 300$  nm  $\sim$  400 nm. In experiments with the  $U_g$  generator, a streamer velocity was determined with a PD025 photodiode (Photek) with subnanosecond time resolution and the maximum sensitivity in the region of 250 nm  $\sim$  500 nm (LNS20 cathode). Using the photodiode, we recorded the time behavior of the radiation intensity 4-cm-width discharge regions, the centers of which were located at the distance of 3 cm, 13 cm, and 23 cm from the edge of the grounded ring-shaped electrode. The rest of the tube was covered with an opaque screen.

A quartz tube was filled with atmospheric air with a humidity of  $\approx 23\%$ , but first it was pumped out to a residual  $p = 10^{-2}$  Torr.

### 3. Experimental Results

#### 3.1 Characteristics of the Discharge Implemented between Additional Electrodes

The experiment was aimed at determining the influence of the polarity of a high-voltage (HV) electrode on the formation of streamers at low air pressures, as well

as fixing their color at pressures of 1 Torr  $\sim$  3 Torr, at which the sprites still remain red. However, the color of the pulsed discharge at low pressures can be either blue or violet<sup>[15,26-31]</sup>. DC voltage of positive or negative polarity from the  $U_{DC}$  source was applied via a 3-m-long cable equipped with a 100-M $\Omega$  resistor to the additional electrodes mounted on the left flange (Figure 3a). The bottom electrode in Figure 3a was grounded through the current shunt. In this case, ring-shaped electrodes were not mounted on the tube, and the length of the tube was 20 cm or 120 cm. As experiments have shown, see below, in a number of cases, the length of the tube affected the characteristics of the discharge.

Intense discharge plasma radiation at  $p = 6$  Torr or higher with additional electrodes shown in the Figure 3a was observed only at their tips (Figure 3b). The discharge current and voltage across the gap (less than  $U_{DC}$ ) were constant during the discharge. Voltage was applied to the additional electrodes via a 100-M $\Omega$ -resistance. If there was no breakdown in the tube, the voltage at the electrodes and at the output of the source ( $U_{DC}$ ) was the same. In the case of air breakdown, a discharge plasma resistance was connected in series with the 100-M $\Omega$ -resistance, and the voltage was redistributed between these two resistances in inverse proportion to their values. Accordingly, the voltage across the electrodes decreased. Streamers (ionization waves) usually were not observed under these conditions.

The formation of streamers in a quasi-stationary regime was recorded at  $p = 1$  and 3 Torr with a relatively low  $U_{DC}$ . An integral photograph of the discharge plasma glow is shown in Figure 3c. Here we can see the glow near the electrodes and a streamer propagating from the HV anode. An image of a streamer obtained with an ICCD camera under these conditions is shown in Figure 3d. Reducing the frame duration made it possible to register only the streamer glow without stationary plasma radiation at the opposite electrode. The length of streamers arisen under these conditions was less than  $d$ , and they were generated in the repetitively pulsed mode. The voltage across the gap in the period between current pulses slowly increased and quickly decreased (the source provided DC voltage). A discharge current waveform had both constant and alternating components (Figure 4).

Under these conditions, the gap breakdown voltage was almost an order of magnitude lower than that supplied from the source. The discharge current was  $\approx 0.65$  mA. The repetition rate of the current pulses increased due to increasing  $U_{DC}$ . This discharge regime is due to the formation of cylindrical streamers, which do not have time to bridge the gap. Due to the high resistance (100 M $\Omega$ ), as well as the small capacitance of the interelectrode gap, the voltage across the latter rapidly decreases during the streamer formation process. This leads to the cessation of the development and propagation of a streamer that

has not reached the opposite electrode, as well as to the recombination of a dense streamer plasma in the gap. Accordingly, a pulsed discharge current mode is implemented, in which the current value rapidly increases and then decreases by more than an order of magnitude. The increase in current is due to the charging of the increasing capacitance between the streamer front and the opposite electrode. It was proposed to call dynamic displacement current (DDC) the current flowing through a gap in this mode [32]. The streamer dimensions and its front velocity, as well as the voltage determine the DDC amplitude across the gap. The latter in these experiments, due to the large value of the charging resistance and small interelectrode capacitance, rapidly decreased with increasing conductivity current. This leads to an increase in the plasma resistance after the streamer stops in the gap and the dense plasma recombines. Then, the voltage across the gap increases again. When the threshold voltage is reached, a streamer is formed again. Moreover, at low air pressures, streamers are formed from the positive electrode, and this electrode could be either HV or grounded. At the air pressure of several Torr, cylindrical streamers near the positive tip begin to form at lower voltage values than at the negative one. An increase in  $U_{DC}$ , in this case, will lead to a gap breakdown [33]. The data are in agreement with the results obtained with corona and diffuse discharges from a metal tip [29,34], as well as with an apokampic discharge from a positive charged bent plasma channel between two pointed electrodes [28]. When a pointed electrode is a cathode (a negative tip) electrons move to a region where an electric field strength is lower, i.e. they move away from the cathode tip. There they attach to oxygen molecules. Due to this, the electric field strength at the tip decreases and higher voltage is required to form a streamer. With a positive tip, electrons move to the tip, and positive ions, due to their greater mass, accumulate at the tip and amplify the electric field in this area. This facilitates the formation of a positive cylindrical streamer [29]. As a result, breakdown in an inhomogeneous electric field occurs at a positive polarity of an electrode with a small radius of curvature at a voltage 2-3 times lower than at a negative one (see, e.g., [33]). At nanosecond voltage pulses and low pressures, the color of the discharges was blue or violet [23,26-31] (without taking into account the influence of the interelectrode material [30]). Under the conditions of the experiments, the color of plasma emission both in the region where streamers propagate and in the region near the electrodes was red, including at the air pressure in  $p = 6$  Torr  $\sim 9$  Torr, at which streamers were not observed.

At  $p = 1$  Torr, with a decrease in the length of the quartz tube to 20 cm, red plasma formed not in the short gap

( $d = 10$  mm, Figure 3a) formed by the tips of the additional electrodes, but in the longer gap ( $d = 36$  mm, Figures 3a and 5a) between the parallel wire electrodes. In this case, there was no plasma at the tips and between them in the gap with  $d = 10$  mm (Figure 5a). However, red colored plasma is visible in the gap with  $d = 36$  mm formed by the parallel parts (wires) of the additional electrodes, as well as near these wires. With a decrease in  $p$  to 0.1 Torr, a violet colored glow appears near the cathode wire (Figure 5b), although red sprite emission is observed in this pressure range. The purpose of the description of this experiment is to show that discharge modes at low pressures can differ significantly under different conditions. In the future, we plan to study in detail the detected discharge mode.

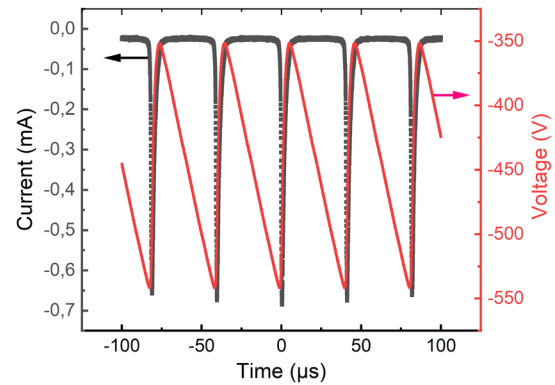


**Figure 4.** Waveforms of the voltage across the gap and discharge current at the air pressure  $p = 3$  Torr.  $U_{DC} = +5$  kV.

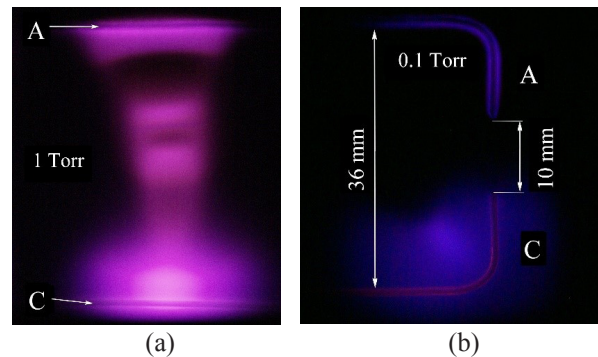


**Figure 5.** Integral photographs of the discharge plasma glow in the gap ( $d = 36$  mm) formed by the parallel parts (wires) of the additional electrodes at  $p = 1$  Torr (a) and  $p = 0.1$  Torr (b) in the 20-cm-length tube.  $U_{DC} = +5$  kV.

Thus, the experiment with additional electrodes confirmed that the formation of streamers leading to gap breakdown from a positive polarity electrode with a small radius of curvature occurs at lower voltages than from an electrode of negative polarity. Herewith, this positive electrode can be either HV or grounded.

However, it should be noted, that the formation of red

sprites occurs without metal electrodes. This explains why we used an electrodeless high-frequency discharge between two ring-shaped electrodes (Figure 2).

### 3.2 Characteristics of the Discharge Implemented between Ring-shaped Electrodes

To provide no plasma contact with electrodes, a repetitively pulsed mode was used. The  $U_g$  generator operated at  $f = 21$  kHz provided the formation of a streamer discharge between ring-shaped electrodes mounted on the outer surface of the quartz tube. The main discharge zone was located in the tube center. The distance between the electrodes was  $d = 6$  cm, while their width was 1 cm each. As noted above, the left electrode was grounded, and the right one was HV. The source provided voltage pulses of both positive and negative polarity. The voltage pulse amplitude was  $U_g = 7$  kV. The rise time of voltage pulse  $t_f$  and its duration  $\tau$  (FWHM) were  $\approx 350$  ns and  $\approx 2$   $\mu$ s, respectively. The experimental setup made it possible to obtain extended streamer discharges at pressures in  $p = 0.4$  Torr  $\sim$  3 Torr. Figure 6 shows photographs of the discharge plasma glow at  $p = 0.4$  Torr with additional electrodes, which were either short circuited or grounded, and without them. In the latter case, a quartz window was installed at the left side of the tube, see Figure 2.

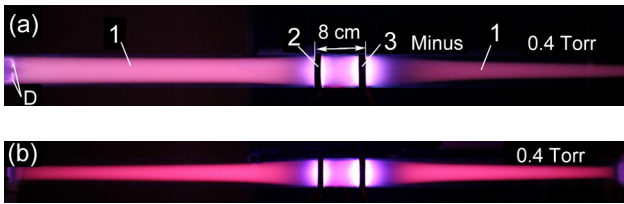


**Figure 6.** Integral photographs of the electrodeless discharge in the quartz tube (horizontal arrangement) with the additional electrodes (a) and without them (b).  $p = 0.4$  Torr. D - grounded additional electrodes. 1 - ionization waves (streamers), 2 - ring-shaped electrode (grounded), 3 - high voltage (HV) ring-shaped electrode of negative polarity.  $U_g = 7$  kV. Shutter speed 0.05 s, lens aperture f/5.6.

The discharge was initiated in the region characterized by the highest electric field, i.e. between the ring-shaped electrodes and near them. This electrodeless discharge is a capacitive one. The color of the discharge plasma in the tube on both sides of the ring-shaped electrodes was red and depended on whether contact with the additional electrode occurred or not. At  $p = 0.4$  Torr, ionization waves (streamers) reached the left end of the tube. This affected the color of the discharge plasma glow and led to an increase in the transverse dimensions of the discharge region (Figure 6a). A further decrease in  $p$ , even without additional electrodes, contributed to the fact that the

streamers were in contact with both ends of the tube.

Changing the polarity of the HV ring-shaped electrode (3) did not have a strong effect on the discharge morphology. Integral photos of the discharge plasma glow at  $p = 1$  Torr and both polarities of the HV ring-shaped electrode are shown in Figure 7.

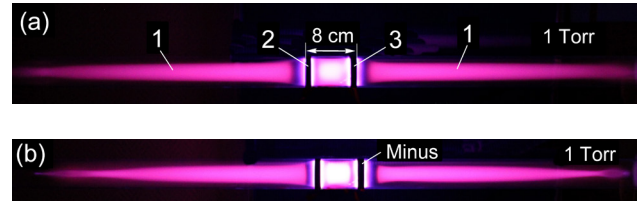


**Figure 7.** Integral photographs of the discharge plasma glow in the quartz tube without an additional electrode filled with air at  $p = 1$  Torr: positive (a) and negative (b) polarity.  $U_g = 7$  kV. 1 - ionization waves (streamers), 2 - ring-shaped electrode (grounded), 3 - high voltage (HV) ring-shaped electrode of positive polarity.  $U_g = 7$  kV.

Shutter speed 0.05 s, lens aperture f/5.6.

As we can see, the morphology and color of the discharge without an additional electrode(s) on the left flange weakly depend on the polarity of the HV ring-shaped electrode. The main differences can be seen at the fronts of the ionization waves, photographs of which are demonstrated in Figure 8.

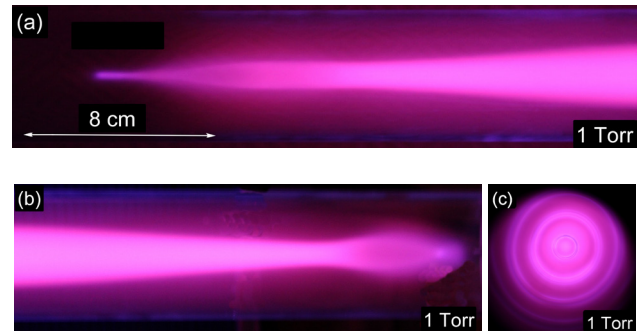


**Figure 8.** Integral photographs of the discharge plasma glow in the quartz tube (without additional electrodes) to the left (a) and to the right (b) of the ring-shaped electrodes at the positive polarity of the HV electrode, as well as a photograph of the discharge plasma glow (c) captured through the quartz window embedded to the left flange (see Figure 2) at  $p = 1$  Torr.  $U_g = +7$  kV.

The ionization wave on the left side has a pointed end. The photo captured through the quartz window embedded to the left flange shows that there is a bright spot in the center, which, apparently, is due to the emission of a part of the ionization wave with a small diameter near the window (Figure 8a). The color of the discharge regions in all photographs is the same.

A decrease in the amplitude of a voltage pulse pro-

duced by the generator leads to a decrease in the length of an ionization wave on both sides of the ring-shaped electrodes. This is demonstrated in Figures 9a,b,c at air pressure of 1 Torr.

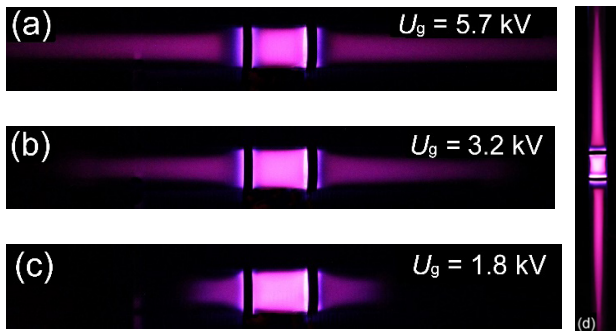


**Figure 9.** Integral photographs of the discharge plasma glow in the quartz tube (without an additional electrodes) placed horizontally (a, b, c) at various generator voltages and placed vertically at  $U_g = 7$  kV and  $p = 1$  Torr (d). The polarity of the right ring-shaped electrode (a, b, c) and the upper one (d) is positive.

With a decrease in  $U_g$ , the length of an ionization wave on the left and right sides of the ring-shaped electrodes decreased, which was to be expected from a decrease in the reduced electric field strength ( $U/pd$ ). However, the red color of the discharge plasma was preserved. A similar shortening of the streamer length and color preservation were observed with a further increase in  $p$  to 3 Torr. At  $p = 6$  Torr and 9 Torr and  $U_g = 7$  kV, a red colored discharge was formed only between the ring-shaped electrodes. There was no discharge in other zones of the quartz tube.

Figures 6 ~ 9a,b,c show the streamer discharge when the quartz tube is placed parallel to the Earth's surface. This position was easy-to-measure of current, voltage, etc. In addition, in a number of experiments, the tube was placed transversely to the Earth's surface (Figure 9d). From the comparison of Figure 7a and Figure 9d, it is seen that the tube position did not affect the formation of ionization waves, as well as their appearance and color. Ionization waves were photographed at the same pressure  $p = 1$  Torr, positive polarity of the high-voltage ring-shaped electrode, and  $U_g = 7$  kV.

The emission spectra of a plasma formed in the region where ionization waves propagate recorded from both sides of the ring electrodes were also the same and did not depend on the position of the quartz tube.

Figure 10 shows the spectral energy distribution  $W_{\text{spec}}$  obtained from the plasma region located at the distance of 13 cm from the left ring-shaped electrode.

The emission spectra of ionization waves at the distance of several centimeters from the ring-shaped electrodes is sim-

ilar to those of red sprites<sup>[17,18,20,21]</sup>. Nitrogen bands belonging to the 2+ and 1+ system contribute predominantly to the spectral energy distribution. Although under these conditions the spectral energy density of radiation of individual bands of the 2+ system exceed that of the 1+ system by more than an order of magnitude, the discharge plasma glow in integral images are red colored (Figures 6 ~ 9). When visually observed, their color is also red.

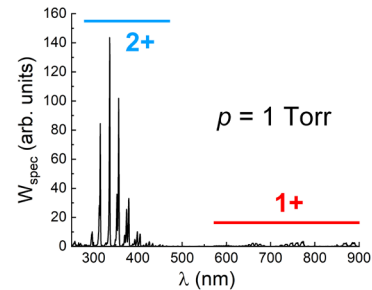


**Figure 10.** Emission spectrum of the discharge plasma in air at  $p = 1$  Torr recorded at the distance of 13 cm from the left ring-shaped electrode.  $U_g = +7$  kV. 2+ - the second positive system (SPS) of a nitrogen molecule, 1+ - the first positive system (FPS) of a nitrogen molecule.

Figure 11 shows a discharge plasma emission spectrum obtained at the distance of 13 cm from the left ring-shaped electrode at the same air pressure as in Figure 10, but with a light filter (ZhS-12) that cuts off radiation in the wavelength range shorter than 450 nm.

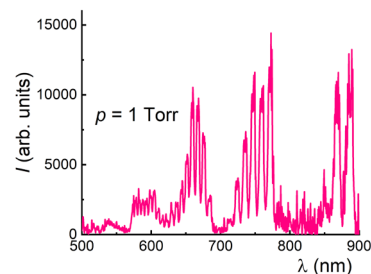


**Figure 11.** Emission spectrum of air plasma at  $p = 1$  Torr recorded at the distance of 13 cm from the grounded ring-shaped electrode to the left with a light filter (ZhS-12) that cuts off radiation in the wavelength range shorter than 450 nm obtained.  $U_g = +7$  kV.

The use of the filter, which has a transmission of  $\approx 90\%$  in the region of 500 nm ~ 1800 nm and a strong absorption in the region shorter than 450 nm, made it possible to identify the main nitrogen bands belonging to the 1+ system, which coincided with good accuracy with the emission spectra of red sprites<sup>[17,18,20,21]</sup>.

The emission spectra from the ionization wave regions obtained to the right and left of the ring-shaped electrodes (starting from a few centimeters from them) practically

coincide and do not depend on air pressure. The spectra, as we noted before, show, that the radiation of the 2+ system dominates. The spectral energy density of this radiation in individual bands is more than an order of magnitude higher than that of the 1+ system. As the pressure increases, the ratio of the intensity of the bands belonging to the 2+ system to the intensity of the bands of the 1+ system can exceed two orders of magnitude. As the pressure decreases to 0.4 Torr, this intensity ratio difference decreases to one order of magnitude. It follows from the data obtained that the emission spectra of ionization waves that propagate in opposite directions are the same. This, as well as their other properties, confirms that it is possible to form two ionization waves from one region, propagating in opposite directions.

Figure 12 shows the spectrum recorded at lower air pressure from the region of an enhanced electric field near the ring electrodes and between them. It is seen, that the spectral energy density of radiation of the first negative band (1-) of a nitrogen molecular ion increases significantly. Wherein, the spectral energy density of their individual lines can be the highest. So, in the area between the electrodes at  $p = 0.4$  Torr, the most spectral radiation energy density at  $U_g = 7$  kV had an ion line of the nitrogen molecule with a wavelength of 391.4 nm (Figure 12). This is explained by an increase in the reduced electric field strength  $E/N$  ( $E$  is the electric field,  $N$  is the concentration of air particles) in this region. The radiation spectrum of dark areas in electrodes (see, e.g., Figure 6) was similar to that in Figure 12 and at  $p = 1$  Torr. Herewith, the width of the dark areas decreased with increasing  $p$ . This indicates an increase in the average electron energy. As can be seen from the images in Figure 6, the color in these areas changes. On the other hand, the radiation spectrum of an ionization wave at  $p = 0.4$  Torr at the distance of 10 cm and more from the right ring-shaped electrode was similar to that in Figure 10.

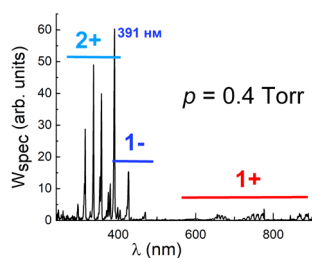


**Figure 12.** Emission spectrum of the discharge plasma glow from the region between the ring-shaped electrodes. 2+ - the second positive system of a nitrogen molecule, 1+ - the first positive system of a nitrogen molecule, 1- - the first negative system of a nitrogen molecular ion.  $U_g = 7$  kV. Air,  $p = 0.4$  Torr.

Red colored glow regions, which are directed in opposite directions from the main capacitive discharge between the ring-shaped electrodes, are formed due to the propagation of ionization waves. This is confirmed by measurements of the main parameters of the discharge plasma along the tube. The main parameters of the plasma formed at the air pressure in the tube of 1 Torr were measured with optical emission spectroscopy (OES) methods<sup>[35-38]</sup>. We used plasma emission spectra recorded from the middle part of the tube (the middle of the distance between the inner edges of the ring-shaped electrodes), as well as at distances of 3 cm, 13 cm, and 23 cm to the right and left of the outer edge of the electrodes. First of all, using a method based on measuring the ratio of the peak intensities of the ion (391.4 nm) and molecular (394.3 nm) nitrogen bands<sup>[35,36]</sup>, we estimated the integral values of the electron temperature  $T_e$  and the reduced electric field strength  $E/N$ . The measurements show that an increase in the distance from the central part of the tube leads to a change in these values from 4.5 eV to 2.5 eV and from 600 Td to 350 Td (which is still quite high), respectively, which is characterized by a relatively small change in the ionization wave front velocity (see the measurement results below). The vibrational temperature  $T_v$  and the gas temperature  $T_g$  were also estimated by applying the Boltzmann method<sup>[36,38,39]</sup> to the emission spectra of the discharge plasma. We would also like to note that these temperatures are practically unchanged over the entire length of the tube and their average values are  $\sim 2700$  and  $\sim 380$  K, respectively. The reliability of the given values is confirmed by modeling the emission spectra of the plasma using the SPECAIR code<sup>[40]</sup>, where these values are used as input data. Despite the fact that the experimentally measured values of the main parameters make it possible to obtain an almost complete coincidence of the simulated spectral distribution of the radiation energy with the emission spectrum recorded by the HR4000 spectrometer, a feature associated with the discharge morphology appears during the simulation. Thus, the simulation data show some increase in the electron density with increasing distance to the tube ends. At a distance of 1 cm from electrode, the electron density was  $\sim 4 \cdot 10^{11}$  cm<sup>-3</sup>, and at a distance of 23 cm it became  $\sim 2 \cdot 10^{12}$  cm<sup>-3</sup>. As follows from Figures 6, 7 and 9, the diameter of the ionization waves (streamers) decreases with distance from the electrodes in both directions. The area of the ionization wave increases in proportion to the square of its diameter. The discharge current in part of ionization wave does not decrease significantly and the current density increases. Although the plasma parameters for air pressures below 1 Torr have not been estimated for this case, it can be confidently claimed

that  $T_e$  and  $E/N$  should be much higher in this case. This is confirmed by the large values of the peak intensity of the nitrogen molecular ion band relative to the intensity of the molecular band (see Figure 12).

Evidence for the implementation of the streamer discharge regime outside the ring-shaped electrodes is also high plasma velocities at various distances from the region where the discharge is initiated. The measurements were carried out using a photodiode. The calculations showed that the average velocity of the glow front between the first (3 cm from the grounded ring-shaped electrode, Figure 6) and the second (13 cm) points was 0.17 cm/ns, and between the second and third ones (13 cm and 23 cm) was 0.12 cm/ns. These values correspond to the propagation velocities of streamers at low pressures<sup>[12,41,42]</sup> and red sprites<sup>[12,17,21,43-45]</sup>. During measurements with the photodiode, the bands of the 2+ nitrogen system was mainly recorded. The radiation energy density in individual bands of the 2+ system (UV region, Figure 10) is significantly greater than that for 1+ bands. In addition, the lifetime of the upper level  $C^3\Pi_g$  of a nitrogen molecule is more than an order of magnitude shorter than that of  $B^3\Pi_g$ . The photodiode also had the highest sensitivity in the UV region of the spectrum.

#### 4. Discussion

When comparing the results obtained in the laboratory and those recorded during observations of red sprites, the following important point should be taken into account. The pressure at altitudes where red sprites propagate varies from  $2.5 \cdot 10^{-4}$  Torr (100 km) to  $\approx 0.8$  Torr (50 km). At the same time, when the altitude changes from 55 km ( $p \approx 0.4$  Torr) to 55.3 km ( $p \approx 0.42$  Torr) relative to the Earth's surface, the pressure increases by only 5%. Therefore, the streamer front propagates a few meters at almost constant pressure  $p$  and particle concentration  $N$ . Based on this fact, we can assume that the change in air pressure at different altitudes should not lead to significant differences in the properties of the ionization wave in the laboratory and red sprites when moving over short distances. Their velocities, color, as well as emission spectra should be similar. The studies carried out confirm this conclusion.

Table 1 shows the main properties of red sprites and ionization waves, which were obtained in our studies. You can see their correspondence.

Let us analyze the obtained results again, compare them with the known data on the development of red sprites, and propose a model for the sprites formation. In experiments, we observed the formation of ionization waves from the plasma of a capacitive discharge. For the formation of red sprites, it is also necessary to have a plasma with a sufficiently high concentration of electrons and ions. We assume that diffuse discharges between different areas of noctilucent clouds are the source of the preliminary plasma. It is known that noctilucent clouds are formed approximately at the same altitudes as red sprites occur<sup>[46]</sup>. The charge separation in noctilucent clouds, which may consist of ice crystals, occurs similarly to the separation of charges in thunderclouds near the Earth's surface<sup>[47]</sup>. During diffuse discharges, plasma has a relatively low radiation intensity due to low air pressure at high altitudes. Therefore, this radiation has not yet been experimentally detected. We assume that in a number of cases diffuse discharges in noctilucent clouds at a sufficient value of the reduced electric field  $E/N$  initiates the formation of ionization waves - sprites. However, we do not deny the possibility of the appearance plasma inhomogeneities and red sprites in the D-region of the ionosphere<sup>[25]</sup>.

The direction of downward sprites at the first stage generates the electric field, which should be directed from appearing place to the negative charge surface. This may be the Earth's surface or the upper surface of thunderclouds. Although, the latter usually has a positive charge<sup>[3,4,13,47]</sup>, but during cloud-to-ground lightning from the upper layer of clouds, the negative charge of the Earth is transferred to this region. As follows from the experiments, the length of the left ionization wave increases when a negative voltage is applied to the additional electrode or when it is grounded (Figure 6a). When sprites that are directed downwards are formed, their length, in addition to reducing the electric field, limits the increase in gas pressure at large distances. It should also be taken into account that the magnitude of the electric field above thunderclouds

**Table 1.** Comparative characteristics of sprites and ionization waves.

Research object	Color	Main spectral bands	Front velocity, m/s	Pressure, Torr	Electron temperature, eV	Reduced electric field strength, Td	Refs.
Sprite	Red	FPS (1+); SPS; (2+)	$(0.4-1.7) \cdot 10^7$	$(3-2.4) \cdot 10^{-4}$	1-2	1s-1000s Td	[4,12,20-22, et al.]
Ionization wave	Red	FPS (1+); SPS; (2+)	$(1.2-1.7) \cdot 10^7$	3-0.4	$\approx 2.5$	$\approx 350$ Td	This paper

changes due to the presence of lightning and the development of the sprite. Apparently, a change in the electric field leads to the propagation of red sprites upward from the Earth's surface, and can also lead to the propagation of sprites in different directions<sup>[17,18,22,41]</sup>. The observed chaotic direction of sprites at altitudes of about 70 km ~ 80 km can also be explained by the uneven distribution of charges in the region of noctilucent clouds.

## 5. Conclusions

It was shown that using a high-frequency electrodeless discharge, it is possible to simulate the properties of red sprites in a laboratory. This possibility was achieved by recording the integral radiation of tens of thousands of individual pulses. At the air pressure of  $\approx 1$  Torr or less, the radiation intensity of the streamer discharge plasma with centimeter dimensions is low. Registration of red sprites in the Earth's atmosphere is simple due to their large size. Using the methods of formation of streamer discharges, a plasma formation with a length of more than 1 m was realized with properties corresponding to those in the plasma of discharges occurring in the natural environment. The air pressure range, observed emission spectra, velocities of ionization wave propagation, as well as visually observed and imprinted color of the discharge plasma glow confirm this. Thus, the length of ionization waves in free space reached 50 cm and was limited by the size of the chamber used as the pressure decreased. As in the sprites, bands 1+ and 2+ systems of a nitrogen molecule dominate in the emission spectrum of the discharge plasma. Moreover, the spectral energy density of the bands of the 2+ system on individual lines was greater than that of the most intense emission bands of the 1+ system. The velocity of ionization wave under laboratory conditions reached 2 mm/ns, which also agrees with the sprite front velocity<sup>[12,17,43-45]</sup>. The color of the generated ionization waves in a wide range of experimental conditions at appropriate pressures was red, as in sprites. In addition, the paper shows the possibility of generating two streamers that propagate in two opposite directions from a diffuse electrodeless plasma of a capacitive discharge.

## Author Contributions

VT supervised the project, analyzed the results, and wrote the manuscript. EB and NV carried out the experiments. DS analyzed the results and performed simulations.

## Conflict of Interest

The authors declare that the research was conducted in

the absence of any commercial or financial relationships that could be construed as a potential conflict of interest.

## Funding

The study is funded by the Ministry of Science and Higher Education of the Russian Federation within Agreement no. 075-15-2021-1026 of November 15, 2021.

## Acknowledgments

The authors are thankful to G.V. Naidis for the helpful discussion and to D.S. Pechenitsin for the development and creation of the pulse generator with a high repetition rate.

## References

- [1] Sentman, D.D., Wescott, E.M., Osborne, et al., 1995. Preliminary results from the Sprites94 aircraft campaign: 1. Red sprites. *Geophysical Research Letters*. 22(10), 1205-1208.
- [2] Bell, T.F., Reising, S.C., Inan, U.S., 1998. Intense continuing currents following positive cloud-to-ground lightning associated with red sprites. *Geophysical Research Letters*. 25(8), 1285-1288.
- [3] Pasko V.P., 2007. Red sprite discharges in the atmosphere at high altitude: the molecular physics and the similarity with laboratory discharges. *Plasma Sources Science and Technology*. 16. S13.  
DOI: <https://doi.org/10.1088/0963-0252/16/1/S02>
- [4] Rodger, C.J., 1999. Red sprites, upward lightning, and VLF perturbations. *Reviews of Geophysics*. 37(3), 317-336.
- [5] Raizer, Y.P., Milikh, G.M., Shneider, M.N., 2010. Streamer-and leader-like processes in the upper atmosphere: Models of red sprites and blue jets. *Journal of Geophysical Research: Space Physics*. 115, A7.  
DOI: <https://doi.org/10.1029/2009JA014645>
- [6] Neubert, T., Østgaard, N., Reglero, V., et al., 2019. The ASIM mission on the international space station. *Space Science Reviews*. 215(2), 1-17.  
DOI: <https://doi.org/10.1007/s11214-019-0592-z>
- [7] Wang, Y., Lu, G., Ma, M., et al., 2019. Triangulation of red sprites observed above a mesoscale convective system in North China. *Earth and Planetary Physics*. 3(2), 111-125.  
DOI: <https://doi.org/10.26464/epp2019015>
- [8] Jiang, F., Huang, C., Wang, Y., 2019. Emission spectrum of sprites caused by the quasi-electrostatic field above thunderstorm clouds. *Meteorology and Atmospheric Physics*. 131(3), 421-430.

- DOI: <https://doi.org/10.1007/s00703-018-0579-4>
- [9] Kuo, C.L., Williams, E., Adachi, T., et al., 2021. Experimental Validation of N<sub>2</sub> Emission Ratios in Altitude Profiles of Observed Sprites. *Frontiers in Earth Science*. 9, 1102.  
DOI: <https://doi.org/10.3389/feart.2021.687989>
- [10] Facebook. Available online: <http://www.facebook.com/frankie.lucena.1> (Accessed on 01.11.2021).
- [11] Füllekrug, M., Mareev, E.A., Rycroft, M.J., (Eds.), 2006. Sprites, elves and intense lightning discharges. Springer Science & Business Media. V. 225.
- [12] Kanmae, T., Stenbaek-Nielsen, H.C., McHarg, M.G., et al., 2012. Diameter-speed relation of sprite streamers. *Journal of Physics D: Applied Physics*. 45(27), 275203.  
DOI: <https://doi.org/10.1088/0022-3727/45/27/275203>
- [13] Ebert, U., Nijdam, S., Li, C., et al., 2010. Review of recent results on streamer discharges and discussion of their relevance for sprites and lightning. *Journal of Geophysical Research: Space Physics*. 115, A00E43.  
DOI: <https://doi.org/10.1029/2009JA014867>
- [14] Wang, Y., Lu, G., Cummer, S.A., et al., 2021. Ground observation of negative sprites over a tropical thunderstorm as the embryo of Hurricane Harvey (2017). *Geophysical Research Letters*. 48(14), e2021GL094032.  
DOI: <https://doi.org/e2021GL094032>
- [15] Williams, E.R., 2001. Sprites, elves and glow discharge tubes. *Physics Today*. 54(11), 41-47.
- [16] Huang, A., Lu, G., Yue, J., et al., 2018. Observations of red sprites above Hurricane Matthew. *Geophysical Research Letters*. 45(23), 13-158.  
DOI: <https://doi.org/10.1029/2018GL079576>
- [17] Stenbaek-Nielsen, H.C., McHarg, M.G., 2008. High time-resolution sprite imaging: observations and implications. *Journal of Physics D: Applied Physics*. 41(23), 234009.  
DOI: <https://doi.org/10.1088/0022-3727/41/23/234009>
- [18] Marshall, R.A., Inan, U.S., 2007. Possible direct cloud-to-ionosphere current evidenced by sprite-initiated secondary TLEs. *Geophysical research letters*. 34(5).  
DOI: <https://doi.org/10.1029/2006GL028511>
- [19] Kuo, C.L., Huang, T.Y., Hsu, C.M., et al., 2021. Resolving elve, halo and sprite halo images at 10,000 Fps in the Taiwan 2020 campaign. *Atmosphere*. 12(8), 1000.  
DOI: <https://doi.org/10.3390/atmos12081000>
- [20] Kanmae, T., Stenbaek-Nielsen, H.C., McHarg, M.G., 2007. Altitude resolved sprite spectra with 3 ms temporal resolution. *Geophysical Research Letters*. 34(7), L07810.  
DOI: <https://doi.org/10.1029/2006GL028608>
- [21] Gordillo-Va'zquez, F.J., Luque, A., Simek, M., 2012. Near infrared and ultraviolet spectra of TLEs. *Journal of Geophysical Research*. 117, A05329.  
DOI: <https://doi.org/10.1029/2012JA017516>
- [22] Qin, J., Celestin, S., Pasko, V.P., 2012. Formation of single and double-headed streamers in sprite-halo events. *Geophysical Research Letters*. 39, L05810.  
DOI: <https://doi.org/10.1029/2012GL051088>
- [23] Sentman, D.D., Wescott, E.M., 1993. Observations of upper atmospheric optical flashes recorded from an aircraft. *Geophysical Research Letters*. 20(24), 2857-2860.
- [24] Garipov, G.K., Khrenov, B.A., Klimov, P.A., et al., 2013. Global transients in ultraviolet and red-infrared ranges from data of Universitetsky-Tatiana-2 satellite. *Journal of Geophysical Research: Atmospheres*. 118(2), 370-379.  
DOI: <https://doi.org/10.1029/2012JD017501>
- [25] Qin, J., Pasko, V.P., McHarg, M.G., et al., 2014. Plasma irregularities in the D-region ionosphere in association with sprite streamer initiation. *Nature communications*. 5(1), 1-6.  
DOI: <https://doi.org/10.1038/ncomms4740>
- [26] Anikin, N.B., Zavialova, N.A., Starikovskaia, S.M., et al., 2008. Nanosecond-discharge development in long tubes. *IEEE Transactions on Plasma Science*. 36(4), 902-903.  
DOI: <https://doi.org/10.1109/TPS.2008.924504>
- [27] Tarasenko, V.F., Sosnin, E.A., Skakun, V.S., et al., 2017. Dynamics of apokamp-type atmospheric pressure plasma jets initiated in air by a repetitive pulsed discharge. *Physics of Plasmas*. 24(4), 043514.  
DOI: <https://doi.org/10.1063/1.4981385>
- [28] Sosnin, E.A., Babaeva, N.Y., Kozhevnikov, et al., 2021. Modeling of transient luminous events in Earth's middle atmosphere with apokamp discharge. *Physics-Uspekhi*. 64(2), 191-210.  
DOI: <https://doi.org/10.3367/UFNe.2020.03.038735>
- [29] Tarasenko, V., Baksht, E., Kuznetsov, V., et al., 2020. Corona with Streamers in Atmospheric Pressure Air in a Highly Inhomogeneous Electric Field. *Journal of Atmospheric Science Research*. 03(4), 28-37.  
DOI: <https://doi.org/10.30564/jasr.v3i4.2342>
- [30] Tarasenko, V., Vinogradov, N., Beloplotov, D., et al., 2022. Influence of Nanoparticles and Metal Vapors on the Color of Laboratory and Atmospheric Discharges. *Nanomaterials*. 12(4), 652.  
DOI: <https://doi.org/10.3390/nano12040652>
- [31] Tarasenko, V.F., 2022. Analysis of Dynamics of At-

- ospheric Discharges Using Data on Cylindrically and Spherically Shaped Streamers. *Atmospheric and Oceanic Optics*. 35(2), 164-167.  
DOI: <https://doi.org/10.1134/S1024856022020154>
- [32] Shao, T., Tarasenko, V.F., Zhang, C., et al., 2013. Application of dynamic displacement current for diagnostics of subnanosecond breakdowns in an inhomogeneous electric field. *Review of Scientific Instruments*. 84(5), 053506.  
DOI: <https://doi.org/10.1063/1.4807154>
- [33] Raizer, Y.P., Allen, J.E., 1991. *Gas discharge physics*. Springer: Berlin.
- [34] Tarasenko, V., Beloplotov, D., Burachenko, A., et al., 2020. On the Formation of a Bead Structure of Spark Channels during a Discharge in Air at Atmospheric Pressure. *Journal of Atmospheric Science Research*. 3(1), 1-8.  
DOI: <https://ojs.bilpublishing.com/index.php/jasr>
- [35] Nassar, H., Pellerin, S., Musiol, K., et al., 2004. N<sub>2</sub><sup>+</sup>/N<sub>2</sub> ratio and temperature measurements based on the first negative N<sub>2</sub><sup>+</sup> and second positive N<sub>2</sub> overlapped molecular emission spectra. *Journal of Physics D: Applied Physics*. 37(14), 1904-1916.  
DOI: <https://doi.org/10.1088/0022-3727/37/14/005>
- [36] Britun, N., Gaillard, M., Ricard, A., et al., 2007. Determination of the vibrational, rotational and electron temperatures in N<sub>2</sub> and Ar-N<sub>2</sub> rf discharge. *Journal of Physics D: Applied Physics*. 40(4), 1022-1029.  
DOI: <https://doi.org/10.1088/0022-3727/40/4/016>
- [37] Paris, P., Aints, M., Valk, F., et al., 2005. Intensity ratio of spectral bands of nitrogen as a measure of electric field strength in plasmas. *Journal of Physics D: Applied Physics*. 38(21), 3894-3899.  
DOI: <https://doi.org/10.1088/0022-3727/38/21/010>
- [38] Ochkin, V.N., 2009. *Spectroscopy of low temperature plasma*. John Wiley & Sons.
- [39] Phillips, D.M., 1976. Determination of gas temperature from unresolved bands in the spectrum from a nitrogen discharge. *Journal of Physics D: Applied Physics*. 9(3), 507-521.
- [40] Laux, C.O., 2002. *Physico-chemical modeling of high enthalpy and plasma flows*. Lecture Series. Belgium: Rhode Saint Genèse.
- [41] Sentman, D.D., Stenbaek-Nielsen, H.C., McHarg, M.G., et al., 2008. Plasma chemistry of sprite streamers. *Journal of Geophysical Research: Atmospheres*. 113, D11112.  
DOI: <https://doi.org/10.1029/2007JD008941>
- [42] Liu, N., Pasko, V.P., 2006. Effects of photoionization on similarity properties of streamers at various pressures in air. *Journal of Physics D: Applied Physics*. 39(2), 327-334.  
DOI: <https://doi.org/10.1088/0022-3727/39/2/013>
- [43] Stanley, M., Krehbiel, P., Brook, M., et al., 1999. High speed video of initial sprite development. *Geophysical Research Letters*. 26(20), 3201-3204.
- [44] Cummer, S.A., Jaugey, N.C., Li, J.B., et al., 2006. Submillisecond imaging of sprite development and structure. *Geophysical Research Letters*. 33, L04104.  
DOI: <https://doi.org/10.1029/2005GL024969>
- [45] McHarg, M.G., Stenbaek-Nielsen, H.C., Kammer, T., 2007. Observations of streamer formation in sprites. *Geophysical Research Letters*. 34(6), L06804.  
DOI: <https://doi.org/10.1029/2006GL027>
- [46] Hervig, M., Thompson, R.E., McHugh, M., et al., 2001. First confirmation that water ice is the primary component of polar mesospheric clouds. *Geophysical Research Letters*. 28(6), 971-974.
- [47] Bazelyan, E.M., Raizer, Y.P., 2000. *Lightning physics and lightning protection*, CRC Press: USA (2001, Fizmatizdat: Moscow, pp. 320).

REVIEW

# The Evil Couple: Illegal Mining in Water Bodies and Climate Change: A Case Study of Ghana

Victor Adjei\* Elijah Foh Amaning Isaac Tettey Adjokatse

Institute for Environment and Sanitation Studies, University of Ghana, Legon, Accra, Ghana

ARTICLE INFO

*Article history*

Received: 9 June 2022

Revised: 20 July 2022

Accepted: 22 July 2022

Published: 8 August 2022

*Keywords:*

Climate change

Galamsey (illegal mining)

Adaptation

Mitigation

ABSTRACT

For the past few decades, illegal mining sector in Ghana popularly known as galamsey has received public outcry due to its negative impacts on quantity and quality of water resources. The purpose of this study was to explore the combined effects of mining in water bodies and climate change on water resources in Ghana. The methodology explored in the study was quantitative approach. The quality and quantity of most water bodies in Ghana had been compromised due to extraction of minerals, and such contaminants (heavy metals) include mercury, zinc, cyanide, sulphur etc. This phenomenon had made most water resources (e.g. River Fena, River Pra) unwholesome or inhabitable. Apart from this, climate change had also dried up some streams and rivers such as Anyinam, Offin and Goa. These unfortunate events had made water resources precarious which could spike water scarcity in the country in the near future. This paper, therefore, commends that stringent measures are to be taken to protect water bodies in the country as a menace of climate will continue to get worse.

## 1. Introduction

Climate change is now universally recognised as a global threat. The main argument has been what might be the nature of climate for tomorrow and what can be done to adapt to tomorrow's climate which has the propensity to change the success story of human race. Another debate has to do with what can be done to mitigate the impacts which primarily emerge from greenhouse gas (GHG) emission and land cover change. Report of Inter-

governmental Panel on Climate Change (Fifth Assessment Report) contents that since 2011, concentration of GHGs has continued to rise in the lower atmosphere as a result of anthropogenic forcing, reaching annual averages of 410 parts per million (ppm) for carbon dioxide (CO<sub>2</sub>), 1866 parts per billion (ppb) for methane (CH<sub>4</sub>), and 332 parts per billion (ppb) for nitrous oxide (N<sub>2</sub>O) in 2019. Over the past decade, the land and ocean have proportionately taken about 56% of GHG emission from human-induced radiative forcing. One of the causes of these effects was

\*Corresponding Author:

Victor Adjei,

Institute for Environment and Sanitation Studies, University of Ghana, Legon, Accra, Ghana;

Email: [victoradjei73@gmail.com](mailto:victoradjei73@gmail.com)

DOI: <https://doi.org/10.30564/jasr.v5i3.4778>

Copyright © 2022 by the author(s). Published by Bilingual Publishing Co. This is an open access article under the Creative Commons Attribution-NonCommercial 4.0 International (CC BY-NC 4.0) License. (<https://creativecommons.org/licenses/by-nc/4.0/>).

the significant increase in world temperature which has caused drastic impacts to the environment and society itself, which has become a worldwide concern regarding the maintenance and the cost of adapting to climate change in the face of its mitigation, which became the order of the day during the summit in Copenhagen in 2009. The summit clearly confirms the acceptance of the constraints that climate change presents to the globe by a larger community<sup>[1-3]</sup>.

Access to good, reliable and adequate water supply augment the health status of people irrespective of age or class. According to International Water Association<sup>[4]</sup>, 'access to good, safe and reliable drinking water is one of the most basic needs of human society'. An observation made by Global Water Partnership<sup>[5]</sup> states that a fifth of the global population is without access to safe drinking water, and service deficiencies mainly impact the poorest class of the population in the third world countries.

The scientific proof for global warming is currently realised irreversible<sup>[8]</sup>; it is evidenced by unparalleled rates of rise in air atmospheric and oceanic temperatures, and it is associated with swift rises in atmospheric carbon dioxide (CO<sub>2</sub>). The unprecedented loss of icecap and glaciers on the world's mountaintops and unabated sea level rise which is 'swallowing' islanders and coastal stretches validate the unceasing warming trends of climate change phenomenon<sup>[3,9]</sup>.

Developing countries such as those found in sub-Saharan Africa which are least contributors to greenhouse gases, as it has been reported and estimated would bear about 70%-80% of the cost of the damages that evolve from climate change<sup>[10]</sup>. Current projection shows that total cost of climate 'insurance' via mitigation actions to stabilize atmospheric temperature increase to 2 °C at carbon dioxide content of 450 parts per million (ppm) will be less than 1% of world Gross Domestic Product (GDP) in 2100<sup>[11,12]</sup>. The changing climate would impact farming activities through higher air temperatures and irregular rainfall, with significant drop in precipitation likely in the mid-latitudes where the state of agriculture is perilous and normally irrigation dependent. It has been reported that rainfall for major and minor seasons has been compromised in duration and intensity in the transitional belt of Ghana<sup>[13]</sup> hence water resource availability and quality would not be spared either, as rainfall trend changes and evaporation increases. Hydrological alteration rising from change in climate would intensely affect aquaculture and inland fishery activities badly. The precarious rain-fed farming in the mid and low-latitudes would continue to

suffer unlike those of higher latitudes (North America and northern Europe) which would experience rise in farming productivity<sup>[3,14]</sup>.

## 2. Methods and Materials

Ghana is the study area, and it is located between 5°N and 11°N and longitude 4°W and 2°E. It borders with Togo in the East, Cote d'Ivoire in the West, Burkina Faso in the North and meets the Atlantic Ocean in the South. It covers approximately (total land area) 238,540 km<sup>2</sup>. Ghana extends up to about 670 km northward from the Atlantic Ocean to Burkina Faso and approximately 560 km from Cote D'Ivoire (W) to Togo (E)<sup>[15]</sup>. Currently, Ghana's population stands at 32.72 million<sup>[16]</sup>. Ghana Meteorological Agency has divided Ghana into four ecological zones<sup>[17]</sup>. The methodology that was made reference to was quantitative approach.

## 3. Global Climate Change and Precipitation

Most of the global projections on rainfall patterns in several regions have been confirmed, but the overall constraints of Global Climate Models (GCMs) in giving explicit spatial trends of precipitation remain problematic. Nevertheless, the latest Atmosphere-Ocean (coupled) Global Climate Models (AOGCMs) is working on the interactions and feedbacks obtained among topography, elevation and albedo<sup>[3]</sup>.

There is enough evidence supporting acceleration of El Nino Southern Oscillation events and the relationship between sea surface temperature (SST) and frequent cyclones occurrence, however, GCMs cannot model them thoroughly. Climate variability is also sped up by these two internal phenomena (La Nina and El Nino) in some regions such as Kenya (La Nina) and southern Africa (El Nino), and their occurrences have accounted for droughts which is negatively affecting GDP<sup>[18]</sup>.

When it comes to prediction of future precipitation, there are uncertainties from a lot of the models. For instance, a recent downscaling exercises across the width and breadth of United States established that there were discrepancies with respect to evidence on precipitation from ensemble GCM modelling and 'off-line'. Regional Climate Model (RCM) modelling projected mean rises in rainfall and runoff in contrary to the earlier report from GCM and ensemble GCM-based work for at least four major river basins<sup>[19-21]</sup>. The reason might be that slight differences in scenario specification and downscaling techniques do not necessarily preserve GCM rainfall per grid cell; GCM grids tend to smear out gradients, particularly precipitation; and

poor representation of an estimated shift to winter dominated precipitation in the Colorado Basin and in California - a change that would improve runoff<sup>[3]</sup>.

The events of precipitation, unlike atmospheric temperature, varies from latitude to latitude or from region to region per the various simulations. Rainfall is predicted to rise over high latitudes, the Equatorial Pacific and parts of the monsoon regions, but reductions over parts of the subtropics and small portions in the tropics in SSP2-4.5, SSP3-7.0 and SSP5-8.5. The part of the land mass experiencing detectable rise or reduction in seasonal average precipitation is estimated to rise as contained in the report of AR6<sup>[18]</sup>.

A warmer climate, as being experienced recently, would amplify very wet and very dry weather and climate events and seasons, with effects of drought or floods. However, the geographical position and frequency of these phenomena depend on estimated changes in regional atmospheric circulation, comprising monsoons and mid-latitude storm tracks. There is a possibility that rainfall variability in conjunction with the El Nino Southern Oscillation is anticipated to intensify by the second half of 21st century in the SSP2-4.5, SSP3-7.0 and SSP5-8.5 scenarios<sup>[18,19]</sup>.

#### 4. Climate Change and Water Resources

Water resource is already over-appropriated in many parts of the globe. It is estimated that more than 2.4 billion people, which represents one-third of the Earth's population, will live in water-stressed regions and it is projected that by 2025, the figure is believed to increase to two-thirds<sup>[22]</sup>.

As rainfall has direct impact on running and groundwater, reduction in precipitation would desiccate most water bodies on the surface of the Earth. According to Adams & Peck<sup>[23]</sup>, variation in rainfall in the face of climate change will influence quantity, variability, timing, form and intensity of water resources. It is worth noting that terrestrial climate change will equally alter or cause a rise in the rate of evaporation, increase proportion of precipitation received as rain instead of snow, reduce runoff seasons, augment water temperatures and decrease the quality of water in both hinterland and coastal zones<sup>[23]</sup>.

It is worth mentioning that many geographical regions will suffer from reduced water supplies. According to FAO<sup>[22]</sup>, due to how man misuses water, groundwater tables and river levels are declining in several regions globally. Summer periods are projected to experience much shortfalls resulting in reduction in moisture content in the soil and more severe and regular agricultural drought<sup>[24]</sup>.

Contrary, winter precipitation in the form of rain will rise as a result of increasing surface temperatures, with a deficit proportion falling as snow. Snow pack levels are equally estimated to develop later in the winter season, amass in minute quantities, and thaw earlier in the season, resulting in reduced summer flows<sup>[23,25]</sup>.

A report of National Centre for Atmospheric Research<sup>[26]</sup> has it that regions classified as 'very dry' have been doubled since 1970s. Besides, areas known to be drought prone regions are also expanding in an alarming rate, and these areas comprise sub-Saharan Africa and Australia. Elsewhere in Northern Hemisphere, the flow of long-term annual rivers and natural water storage capacity have been experiencing deficit due to glacial/snow cap melting. Several Asia's largest rivers are estimated to drop off in coming years due to glacial thawing. Scientists have projected a possible dryness of Lake Mead, which serve over millions of inhabitants in the south-western United States, around 2021<sup>[25-27]</sup>.

#### 5. Existing Challenge of Water Resources

One of the major problems that is threatening human survival especially in the developing countries is declining water quality. The situation is compounded by inadequate wastewater treatment due to unavailability of resources or capital. In most of less developed countries such as those found in African soil, running water (strings, streams, rivers etc.) traditionally used as sources of drinking water have been dangerously polluted by some citizens (miners) and expatriate alike who want to get rich overnight. In China, for instance, several water bodies have been polluted beyond measure. It has been estimated that due to insufficient sanitation facilities and rising water demand as a result of growing population, it is documented that globally, 900 million people lack access to safe water while up to 5 million populace die each passing year from water-related illness<sup>[24,28]</sup>.

#### 6. El Nino Southern Oscillation (ENSO) Events in Ghana

The impacts of El Nino South Oscillation is very strong on all the ecological zones in Ghana as indicated by Adiku *et al.*<sup>[29]</sup> and Sultan *et al.*<sup>[30]</sup>, and it was dominant around 1972-1973, 1982-1983, 1997-1998. However, the strong influence of La Nina episodes of 1973-1974, 1975-1976 and 1988-1989 has also been felt along the coast and the forest zone. Usually, the impact of ENSO is strongest at the coast than the northern part of the country as it weakens northwards due to some dynamics from West African

Monsoon [29]. The variability of the ENSO in Ghana improves the easterlies and decreases monsoon movement. The upper easterlies are weakened giving rise to dry situations near the surface of the Inter-Tropical Discontinuity (ITD), and this happens during major rainy season and the dry season. Mawunya *et al.* [31] contend that ENSO years are characterised with late onset of rainfall while La Nina years are characterised with early onset. Various studies by Paeth & Hense [32], Owusu *et al.* [33] and Yorke & Omotosho [34] confirm that there has been a decline in the amount of annual rainfall. Recently, rainfall amount has persistently declined since 70s and it can be attributed to the strong event of ENSO, as it was also predominant around 2009-2010 [35].

### 7. Seasonal Trend Analysis

Generally, all the four agro-ecological zones in Ghana are experiencing reduction in rainfall with the exception of Coastal Zone which has a predominant increasing pattern (Table 1). This increasing trend that has characterised the coastal zone is nevertheless insignificant using the Mann Kendall Trend Test at the 0.01 and 0.05 significant levels (Table 1). The transitional zone persistently displays significant declining trends in all the seasons with the exception of June, July and August (JJA) as shown in Table 1. The December, January and February (DJF) season (also known as the Harmattan season) depicts a significant reduction trends at the 0.01 significant level for all but one of the agro-ecological zones signifying intensification of the dry season [15] as shown in Figure 1.

**Table 1.** Rainfall Trend Rate (mm per year)

Seasonal Rainfall	Coast	Forest	Transitional	Savannah
DJF	-0.1429**	-0.1273**	-0.1040**	-0.0102
MAM	0.0692	-0.0793	-0.2016**	-0.1181**
JJA	0.0510	-0.0242	0.2112*	-0.0972
SON	0.0677	-0.0512	-0.1460*	-0.1582**

DJF- December, January, February; MAM - March, April, May; JJA - June, July, August; SON - September, October, November (*Wavelet Analysis of Rainfall over the Agro-Ecology Zones of Ghana*).

Source: [15]

The rate of seasonal rainfall pattern in the four agro-ecological zones in Ghana (\*\* and \* show significant trends at 0.01 and 0.05 significant levels respectively)

The Figures shown below represent the seasonal mean rainfall over Ghana (Figure 1).

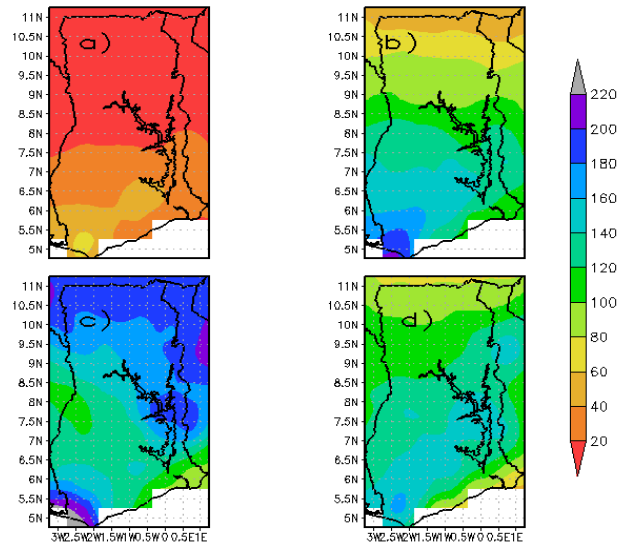


**Figure 1.** Seasonal mean rainfall (mm) over Ghana for a) December- January - February B) March - April - May C) June - July - August D) September - October - November During 1901 - 2010 period

Source: Baidu *et al.* (2017)

### 8. Inter-Tropical Discontinuity (ITD)

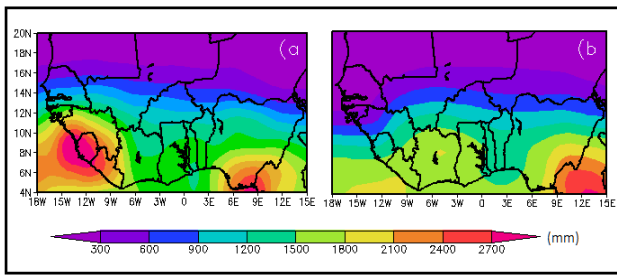
The nature of rainfall in West Africa, as shown in Figure 2, is characterised with variability on inter-annual and decadal time scales, and it is highly correlated with Sea Surface Temperature (SST) [36]. The positive ENSO Sea Surface Temperature anomalies of the eastern tropical Pacific has greater impact on dry conditions prevailing over Sahel and wet conditions over Guinea. The phenomenon is also correlated with SST anomalies of the Southern Hemisphere Atlantic and with negative anomalies of the Northern Hemisphere Atlantic (the Atlantic dipole) and positive SST anomalies of the tropical Indian Ocean [37-39].

Basically, the simulated pattern replicates the observed trend. Related to the observations, the broad features of rainfall experienced in West Africa such as the one that characterises Ghana-Togo gap was simulated by the model studied by Ekwezuo *et al.* (2017) as shown in Figure 2.

Figure 2 shows rainfall simulation observed in West Africa.

With regards to Representative Concentrated Pathway (RCP) 4.5 (Figure 3), around the coast of Cameroun, rainfall is projected to rise by ~35 mm, the adjacent coast by ~1 mm to 20 mm. It is anticipated that the expected changes would not benefit inland stretch where the projection will be around ~1 mm to 10 mm with the exception of north-western Nigeria, some parts of Mali, Togo and Ghana where precipitation is projected to remain compar-

atively unchanged.



a) GPCP-observed      b) NorESM1-M- simulated

**Figure 2.** Mean annual rainfall trend over West Africa sub-region for the baseline period (1980-2005)

Source: Ekwezuo *et al.* (2017)

Under RCP 8.5 (Figure 3), approximately 35 mm rise in precipitation is projected around the coastal stretch of Cameroun, followed by the adjacent coast where increase of ~1 mm to 25 mm should be expected. On the other hand, rainfall reduction (~1 mm to 10 mm) is expected to characterised farther inland with an exception of north-eastern Niger and Guinea where it is anticipated to remain unchanged.

It can be inferred that under all the RCP, there is an anticipated rise in rainfall amount, with the southern part of the sub-region most especially coastal areas of Cameroun (~20 mm to 35 mm) experiencing the highest amount of precipitation. Closely followed is the south-western part of the Atlantic Ocean with a rise of ~10 mm to 30 mm. Other regions are to experience an increase of ~1 mm to 10 mm. With respect to areas where there is no noticeable change or little change, there is a considerable difference in the RCPs (Figure 3) except over the Atlantic Ocean [40].

The different rainfall regime in Ghana, the West African country, along the coastal stretch in the south to the Sahelian region in the far north [41] is defined by the northward and south-ward oscillation of the Inter-Tropical Convergence Zone [42]. This phenomenon results in African monsoon, leading to uni-modal and bi-modal distribution characteristic of the northern and southern part of the country, respectively.

The rainfall annual cycle in Ghana is characterised by bi-modal type of rainfall in the south as there is double maxima rainfall regime and uni-modal rainfall trend in the north characterised with one rainy reason followed by long dry spell popularly known as Harmattan. The rains commence in April and gets to its maximum in August-September when the moisture-bearing tropical maritime air mass gets there to induce heavy rainfall [15]. The cessation of rainy season in the north begins in October and welcomes the dry northeast trade winds. The north-

east trade winds start to become dominant in November which normally lasts till March.

Under all RCP, the West African sub-region is estimated to enjoy a rise in precipitation amount. This, nevertheless, contradicts the projected change trend in the early twenty-first century. The Figure 3 below shows the current precipitation projection.

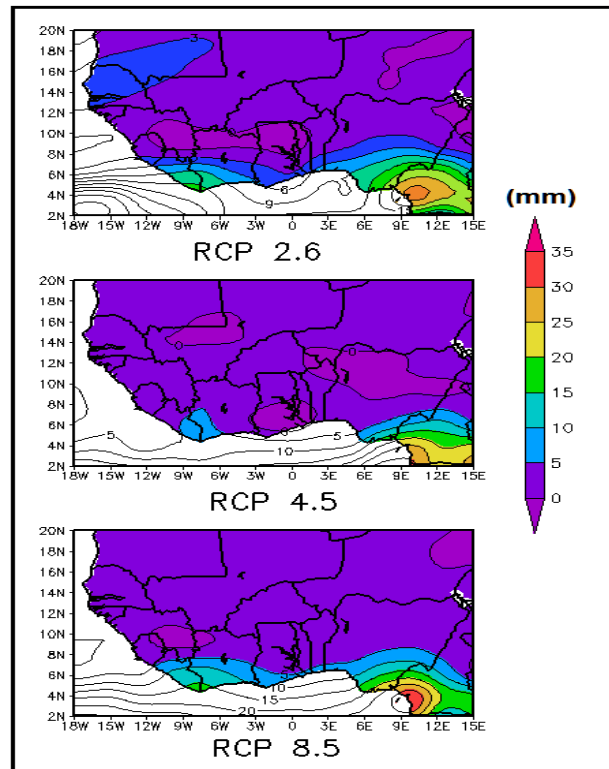


**Figure 3.** Projected changes in annual rainfall trend for mid twenty first century

Source: Ekwezuo *et al.* (2017)

## 9. Evidence of Climate Change in Ghana

According to IPCC forth assessment report [43], currently, Ghana is undergoing four physical impacts of climate change, and these include temperature rising, changing regime of rainfall towards a longer dry season and vanishing rainy season. Climate change is impacting on rainfall trend in all ecological zones but has hit hard in the far north where rainfall regime is single maxima. Recent sea level rise coupled with floods being experienced in south-east (Keta) of the coast of Ghana is a clear indication that climate change is at work.

A projected trend of atmospheric temperatures from 2010 to 2050 by World Bank as cited by Asante & Amuakwa-Mensah [44] for Ghana shows warming over the entire West African country with the highest temperatures occur-

ring in the northern part of Ghana with the lowest being experienced in the transitional belt (formerly Brong Ahafo).

The current mean annual temperature ranges between 25 °C to 30 °C. However, occasionally, the air temperatures can be as low as 18 °C (minimum) and as high as 40 °C (maximum) in the northern part of Ghana <sup>[44]</sup>.

An average annual precipitation of 2000 mm/year, 950 mm/year and 800 mm/year occur in the South West, Northern and South Eastern parts respectively. According to a study by Adjei & Kyerematen <sup>[13]</sup> and Owusu, *et al.* <sup>[45]</sup>, the transitional ecological zone of Ghana (a region separating forest from Savanna belt) has undergone late onset of rainfall (from early March to late March) and early cessation of it (from November to late October). This has compelled farmers to shift planting date from March to April <sup>[46]</sup> while others (farmers) too have turned their attention from their main occupation (maize) to cashew farming <sup>[47]</sup>. A long-term data analysis by Dietz *et al.* <sup>[48]</sup> shows that places in the northern part of Ghana around Upper East Region has equally experienced below average rainfall conditions for over 18 years (1972-1990). In the same vein, it is reported that drought years have risen in several parts of Ghana. According to a study by Adiku *et al.* <sup>[49]</sup>, manifestation of drought year has reached 3 to 4 out of every 10 years in the late 1980s as compared to 1 to 2 years in the preceding years. The paper further argued that rainfall irregularity analysis substantiate the swing from drought to flood years have become pervasive posing great threats to most smallholder farmers in Ghana.

The climate change in Ghana is having a negative impact on vital water resources, energy supplies, crop production and food security. The three northern regions of Ghana are the most vulnerable with the experience of extremely high temperatures and severe flooding <sup>[50]</sup>. According to Akudugu and Alhassan <sup>[51]</sup>, the northern part of Ghana has repeatedly experienced incidences of droughts and floods with several communities and families losing their farms as a source of their livelihood in the past years which is attributed to a change in climatic conditions. Furthermore, in 2007, floods in the northern part of the country, proceeded a long period of dryness which affected more than 325,000 people (Global Facility for Disaster Reduction and Recovery) <sup>[52]</sup>. The capital city of the country (Accra) in 2015, also experienced days of torrential rainfall which resulted in severe flooding leaving 159 Ghanaians losing their lives <sup>[53]</sup>. However, Ghana as a whole is also experiencing increased extreme weather conditions <sup>[54]</sup> such as a rise in sea level causing flooding and displacing some communities in the coastal belt. Ghanaian farmers have identified erratic rainfall

patterns, longer periods of dry season and desertification as the main current consequences of climate change <sup>[55]</sup>. Prolonged period of drought coupled with high temperatures is also experienced, changing rainfall pattern making it difficult for farmers to plan their planting season due to their inability to predict rainfall pattern <sup>[13]</sup>. This has affected food production and poor yield by farmers causing food insecurity in Ghana (especially in the northern part). Farmers are therefore forced to grow crops that are resilient to extreme weather conditions such as cassava, cocoa and cashew <sup>[46]</sup>. Furthermore, prolonged drought has caused drying up of major water bodies that serve as source of raw water to the Ghana Water Company Ltd (GWCL). This has caused water shortage in several communities, villages, towns and cities in the country <sup>[56]</sup>.

There is also a current tension between Ghana and Burkina Faso over a decision to withdraw water from the River Volta which would lead to a reduction in the volume of water needed for the production of electricity in Ghana from a study carried out by USDA <sup>[57]</sup>. This however could lead to trans-boundary conflict. In addition to the above evidence of climate change in Ghana is where nomadic herdsmen in search of water and grass to feed their cattle cause destruction to farmers in the southern part of the country. This has led to a number of conflicts between the Fulani herdsmen and the farmers <sup>[58,51]</sup>. The decrease in the volume of water in the Akosombo dam has also had a negative impact on generation of hydroelectric power in that the country experienced severe power outages consistently as a result of drought <sup>[59]</sup>. Due to an increase in air temperatures, the countries inland fisheries in Lake Volta also experience a reduction in stock <sup>[60]</sup>.

## 10. Nature of Water Resources in Ghana

Basically, water resources in Ghana can be categorised into surface and underground sources. The known major water bodies (rivers) classifying under surface water in Ghana include River Volta and its tributaries (Oti, Black and White Volta), Pra, Bia, Tano, Todzie, Aka, Densu, Ayensu, Ankobra, Ofin and Och-Nakwa (Figure 4). Apart from the tributaries of River Volta, almost major rivers in Ghana drain the southern sector of the country <sup>[61,62]</sup> (Figure 4). The largest river, which is River Volta, is shared among five other countries which include Cote d' Ivoire, Mali, Burkina Faso, Togo and Benin. It drains about 70% of the total land of the country (Ghana) and the other rivers take over the 30% remaining <sup>[61]</sup>.

About 41% of the population of Ghana depends on groundwater for their livelihood. Nevertheless, this rate is higher in the small communities in the hinterland (59%) as compared to urban areas (16%). The dependency ratio

of the populace on groundwater is highest in the northern part of Ghana due to low seasonal availability of surface water [63,64]. Unlike precipitation where the projection is full of uncertainty, higher atmospheric temperatures are expected to be dominant hence will speed up evaporation and result in water losses and this will consequently affect water resources in most parts of the country [44].

The surface water sources are made use by industries, home, transport services and tourist whereas the groundwater sources are mainly used among both urban and rural folks for domestic purposes [62].

A study conducted on River Offin [65] suggests that climate change has a great gravity on water resources. The study argued that several tributaries that feed the River Offin are drying up with some ceasing to exist. The dryness of the tributaries of River Offin has made the volume of the River small. So when dry season prolongs, the River reduces to pocket of stagnant water bodies. In 2013 for

instance, the report maintained that the River Offin dried up and became dry land. Hand-dug wells were produced around the banks of the river to provide alternative source of water to the communities at the catchment area. Other rivers which have also been affected by this phenomenon are River Anyinam in the Eastern Region closed to Anyinamso and River Goa near Goaso. A research has established that the entire river, which the community (Anyinamso) was named after, has vanished (dried up) leaving behind its huge channel due to scanty rainfall and dissipation of streams that supply constant water to the river [65].

Apart from River Volta and its tributaries, most of the water bodies (rivers) found in Ghana can be located in the southern part of the country as depicted in Figure 4. The Figure 4 also shows that Ghana does not experience water stress or scarcity (if the country gives priority to its water resources).

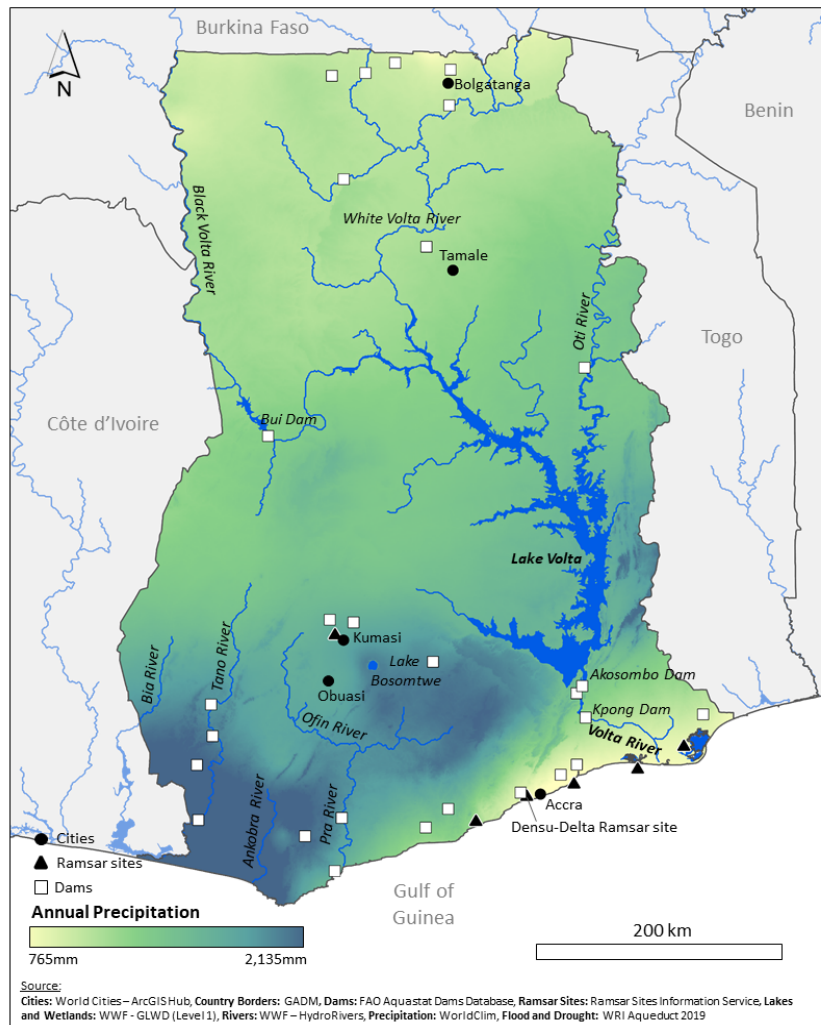


Figure 4. Annual rainfall and major water bodies in Ghana

Source: USAID (n.d)

## 11. Mining Operations in Ghana

### 11.1 Nature of Illegal Mining (Galamsey) Activities in Ghana

Ghana, a West African country formerly called Gold Coast, is blessed with enormous mineral deposits (Figure 5); the major ones being gold, diamonds, manganese and bauxite. Gold is principally the largest mineral produced in the West African country, accounting for over 90% of all mineral revenues accrued from minerals for the past two or more decades<sup>[66]</sup>. The sector is made up of large and small scale industries. The small scale also comprises legal and illegal mining sectors. The small scale sector absorbs about one million unemployed indigenous people<sup>[67]</sup>. The unregulated or illegal mining sector which is commonly known as *galamsey*, is the chief polluter of water bodies as its activities are not monitored by any legal instrument. According to Baah-Ennumh<sup>[68]</sup>, illegal mining in Ghana depicts all mining activities done without obtaining proper license from regulatory bodies that govern practices of miners, hence such activities flout most of the mining laws, and fail to observe appropriate buffer restrictions. They make use of rudimentary tools and techniques such as pick ass, chisels, sluices and pans for the exploitation of mineral reserves<sup>[69,70]</sup>.

In Ghana, and many other countries in sub-Saharan Africa, predominant environmental challenges associated with small-scale mining activities consist of destruction of farmlands, pollution of water bodies, destruction of vegetation and habitats of wildlife<sup>[71,72]</sup>.

According to a study by Yeleliere *et al.*<sup>[73]</sup>, about 60% of surface water bodies in Ghana are polluted, and the menace is worse in the southern part of the country where mining activities are ubiquitous. High turbidity in the River Pra for instance has substantially increased water treatment cost and left some plants inoperable for couple of years<sup>[74]</sup>. A study has shown that River Volta basin contains high level of chromium that might have come from industrial or municipal pollution<sup>[65]</sup>.

Ghana is blessed with gold. However, most of the rocks containing this mineral are found in the western part of the country running from north to south (Gulf of Guinea) as shown in Figure 5.

### 11.2 Impacts of Illegal Mining (Galamsey) on Drainage Systems

There are countless of environmental problems and challenges linked to mining activities which evolve from competition for surface water<sup>[76]</sup>. The danger posed by illegal mining to water quality and water resources in

Ghana has led to public outcry due to the closure of several treatment plants and how it has left several water bodies unusable<sup>[77]</sup>. Contamination, which is very deadly to both aquatic and living creatures, results from the discharge of effluents making up the various toxic chemicals such as cyanide, mercury and other organic chemicals used in the processing of mineral ores. These chemicals (with high percentage of acid) of effluent can either percolate into the soil affecting underground water or cause havoc to water bodies on the surface of the earth posing threat to human-kind, domestic animals and even wildlife which depend on the water bodies in the catchment area<sup>[78-80]</sup>. "Once in the natural environment, mercury undergoes a change in speciation from an inorganic to a stable methylated state (MeHg) by non-enzymically and microbial action, and when ingested, ecotoxicological effects result"<sup>[82]</sup>.

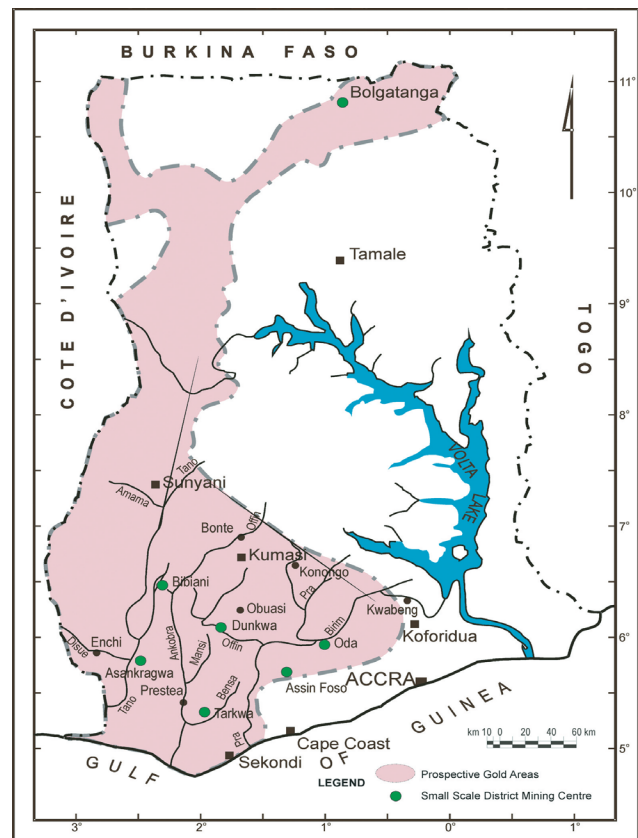


**Figure 5.** Prospective Gold Mining Areas in Ghana

Source: Hilson (2002)

Another concern of worry is the leaching of heavy metal oxides which comprises lead and zinc. Sometimes, these aforementioned metals spread throughout the environment following down pour causing mayhem to aquatic life, fauna, flora and the micro-organisms<sup>[78]</sup>. It is very hard, in recent years, to notice water resources such as crabs, fish, shrimps, snails etc. in the water bodies

found in Ghana especially where mineral is mined due to the presence of hazardous chemicals in most water bodies<sup>[83]</sup>.

It has been reported that<sup>[81]</sup> the south-western basin of River Tano contains heavy metal from gold mining, but the situation is worse in the River Pra Basin where hazardous illegal mining is intensified. Again, arsenic levels near Prestea (River Pra Basin) have also been detected nearly 800 times the World Health Organisation (WHO) guideline limit for human consumption, most likely from unregulated gold mining in the country<sup>[61,74,73,84]</sup>.

Total metal concentrations in mg/kg dry weight (ppm) and organic matter content determined as loss on ignition (LOI) on river sediments done by Donkor *et al.*<sup>[85]</sup> from the River Pra basin during the rainy season (summer season) are displayed below. The Table 2 shows the mean values of physicochemical parameters and the maximum and minimum values of heavy metal concentration in River Pra. The various contaminants in the river make it unwholesome for human and animal utilisation or consumption.

Furthermore, a study by Duncan<sup>[77]</sup> in River Pra established that excessive pollution of the River (Figure 6) poses health threat to the riparian communities around

which rely on the River for their livelihood as most fisher men too had lost their jobs due to the death of fishes in the water body.

High or low pH can cause the death of aquatic organisms. pH also influences the solubility of certain toxic compound such as heavy metals in a river (Table 3).

Total metal concentrations in mg/kg dry weight (ppm) and organic matter content determined as loss on ignition (LOI) on river sediments done by Donkor *et al.*<sup>[85]</sup> from the River Pra basin during the dry season (winter season) are shown in Table 3. BDL = Below Detection Limit (i.e. 0.003 ppm for Pb and 0.00075 ppm for Co). The Table 3 shows the mean values of physicochemical parameters and the maximum and minimum values of heavy metal concentration in River Pra. The various pollutants in the river make it unwholesome for human and animal utilisation or consumption.

Natural courses of several water bodies are either diverted or blocked to provide successful operations of small scale mining activities (most especially the illegal ones), and sample is given below in Figure 6. While large scale mining takes into account the health of the ecosystem, the small scale mining does not as the miners tend to float over environmental laws.

**Table 2.** Water quality parameters of River Pra in dry season (winter)

River	Section Site #	Hg	Al	Fe	As	Pb	Cu	Mn	Co	Ni	V	Cr	Zn	%OM
Lower Pra	1	0.066	278.1	301.2	0.414	0.238	0.263	6.790	0.053	0.439	0.777	0.905	1.418	2.08
	2	0.076	267.5	328.1	0.411	0.043	0.226	8.955	0.134	0.370	0.791	0.819	1.531	5.55
	3	2.917	236.9	168.7	0.213	0.179	0.252	2.387	0.130	0.271	0.706	0.724	1.553	9.98
	4	0.018	146.2	134.8	0.184	0.064	0.127	3.516	0.063	0.308	0.392	0.47	0.742	11.50
	5	0.046	174.7	225.3	0.360	0.096	0.221	6.518	0.188	0.362	0.758	0.825	1.214	1.30
	6	0.103	195.1	155.6	0.384	0.041	0.158	4.384	0.078	0.318	0.518	0.586	0.754	4.92
	7	0.022	223.6	220.7	0.488	0.022	0.221	6.297	0.166	0.348	0.652	0.744	1.072	1.67
	8	0.310	348.9	370.4	0.691	0.078	0.333	8.595	0.272	0.493	1.098	1.321	1.285	7.61
Upper Pra	9	0.079	226.8	432.9	0.180	0.060	0.386	4.883	0.112	0.356	3.378	1.176	1.526	1.91
Pra	10	0.678	158.1	166.2	0.079	0.214	0.169	2.658	0.023	0.300	0.594	0.620	0.802	2.89
	11	0.071	273.7	376.1	0.115	0.014	0.323	5.002	0.249	0.441	1.252	1.273	1.201	1.56
	12	0.180	736.9	1266.3	0.133	0.160	1.010	10.704	0.517	0.874	0.861	2.401	1.603	7.91
	13	0.070	236.8	290.2	0.165	2.441	0.299	3.546	0.138	0.342	0.834	1.100	1.286	3.47

Source: Donkor *et al.* (2005)

The low and stable temperature recorded, as shown in Table 4, do not favour the growth and survival of aquatic species; this would explain why fishes are scarce in rivers where mining is done. Apart from the temperatures menace, there are other factors such as presence of heavy metals that have resulted in disappearance of fishes.

The majority of aquatic creatures prefer a pH range of 6.5-9.0 even though some can live outside that pH range. The pH of water can equally be influenced by the acidity of the catchment area. Fen 1 has a pH value within World Health Organisation’s permissible value as recorded above. Again, heavy metals can be dissolved into water by low pH; due to the continuous usage of rivers by farm-

ers for irrigation purpose, this phenomenon has a public health concern <sup>[77]</sup>.

Temperature positively impacts aquatic life. It accelerates the activity of photosynthesis, reaction of pollutants and parasites, and influences solubility of dissolved oxygen in water <sup>[86]</sup>.

The concentration of pollutants (metals) shown above were far higher than required limit is an indication that the river was polluted, and these metal concentration has been aggravated by the intensity of the mining carried out in the water body. The results show poor and marginal quality of River Fena, and this possesses threat to domestic activities and aquatic life.

**Table 3.** Water quality parameters of River Pra in dry season (winter)

River	Section	Site #	Hg	Al	Fe	As	Pb	Cu	Mn	Co	Ni	V	Cr	Zn	% OM
Lower Pra	1	0.003	90.0	141.0	0.216	BDL	0.018	3.031	*BDL	0.252	0.204	0.203	0.569	0.46	
	2	0.008	308.0	214.0	0.146	BDL	0.089	2.828	BDL	0.400	0.484	0.523	1.199	3.15	
	3	0.002	406.0	236.0	0.281	BDL	0.153	5.102	BDL	0.457	0.645	0.732	0.704	1.68	
	4	0.017	570.0	283.0	0.355	BDL	0.207	4.461	BDL	0.457	0.878	0.985	1.280	4.74	
	5	0.005	117.0	68.0	0.218	BDL	0.029	1.470	BDL	0.301	0.145	0.267	0.746	0.25	
	6	0.043	198.0	271.0	0.370	BDL	0.192	7.890	BDL	0.453	0.619	0.579	1.152	0.96	
	7	0.009	287.0	135.0	0.158	BDL	0.091	2.573	BDL	0.343	0.475	0.575	0.557	0.00	
	8	0.002	245.0	247.0	0.458	BDL	0.133	8.221	BDL	0.574	0.548	0.537	0.756	3.01	
Upper Pra	9	0.002	407.0	497.0	0.125	BDL	0.150	5.016	BDL	0.437	0.867	1.030	1.027	1.74	
Pra	10	0.002	318.0	116.0	0.088	BDL	0.072	2.195	BDL	0.429	0.461	0.522	0.728	0.52	
	11	0.005	509.0	356.0	0.124	BDL	0.196	9.781	BDL	0.568	0.885	1.031	1.171	0.39	
	12	0.030	288.0	378.0	0.103	BDL	0.261	4.480	BDL	0.429	1.219	1.755	0.666	0.84	
	13	0.043	247.0	243.0	0.369	BDL	0.049	2.495	BDL	0.569	0.349	0.333	0.881	2.91	

Source: Donkor *et al.* (2005)



**Figure 6.** Illegal activity in Ghana.

Source: Fatawu, & Allan (2014)

**Table 4.** The quality of River Fena in a mining area

Parameters	Fen 1			Mean and std	Fen 2		WHO standard
	Mean and std	Max	Min		Max	Min	
pH	6.17 ± 0.27	6.63	5.82	5.81 ± 0.41	6.33	5.21	6.5-9
Temp.	23.58 ± 0.17	23.85	23.31	23.45 ± 0.17	23.73	23.08	25-30°C
Turb.	182.25 ± 20.49	213	148	194.33 ± 16.34	231	169	75NTU
TSS	2415.67 ± 440.1	3314	2560	2971.67±	3354	2830	500 mg/L
TDS	3165.33 ± 207.83	3314	2560	3180.50 ± 142 .11	3334	2730	500 mg/L
Conductivity	1236.75 ± 59.38	1311	1103	1268 ± 19.44	1300	1238	1000 mg/L
Pb	0.192 ± 0.23	0.81	BDL	0.72 ± 0.29	1.04	0.23	0.01 mg/L
Cd	0.14 ± 0.19	0.7	BDL	0.02 ± 0.01	0.04	0.01	0.003 mg/L
Cu	0.09 ± 0.03	0.14	0.03	0.09 ± 0.06	0.24	0.01	2 mg/L
Fe	12.94 ± 1.57	16.43	11.03	13.01 ± 0.71	14.09	11.63	2 mg/L
Zn	0.81 ± 0.14	0.91	0.46	0.84 ± 0.09	1.02	0.71	5 mg/L

Source: Duncan (2020)

## 12. Conclusions and Recommendation

Ghana has enough water bodies that can protect the country from water stress. There is also enough groundwater to shield the West African country from water scarcity. However, climate change and variability are currently impacting on these water bodies drying up most tributaries which feed up such streams and rivers. In recent years, most rivers are either reducing volumes drastically or completely drying up. The presence of illegal mining in water bodies is compounding the situation which might lead the country to experience water stress if measures are not put in place to contain mining in river banks and beds. Politicisation of sensitive issues in Ghana has made the fight against illegal mining in water bodies extremely difficult for the various ruling governments.

## Conflict of Interest

There is no conflict of interest.

## References

- [1] National Oceanic Atmospheric Administration (NOAA), 2019. Global Climate Report, Annual 2018. US National Oceanic and Atmospheric Administration's National Centers for Environmental Information (NCEI). <https://www.ncdc.noaa.gov/sotc/global/201813>.
- [2] Intergovernmental Panel on Climate Change, 2021. Masson-Delmotte, V., Zhai, P., Pirani, A., Connors, S.L., Péan, C., S. Berger, N., Caud, Y., Chen, Y., Goldfarb, L., Gomis, M.I., Huang, M., Leitzell, K., Lonnoy, E., Matthews, J.R., Maycock, T.K. Waterfield, T., Yelekçi, O., Yu, R. & Zhou. B. The Physical Science Basis. Contribution of Working Group I to the Sixth Assessment Report of the Intergovernmental Panel on Climate Change. In Press. [www.environmentalgraphiti.org](http://www.environmentalgraphiti.org).
- [3] Intergovernmental Panel on Climate Change, 2011. IPCC Introduces New 'Climate Change' Definition. IPCC SREX Summary for Policymakers page 2. <http://www.thegwpc.org/ipcc-introducesnew-climate-change-definition/>.
- [4] International Water Association, 2004. The Bonn Charter for Safe Drinking Water, Bonn. Retrieve from <https://www.wateraction.hub.org>.
- [5] Global Water partnership, 2000. Integrated Water Resources Management, Global Water Partnership, Stockholm. Retrieve from <https://cap.net.org>.
- [6] Grillakis, M.G., 2019. Increase in severe and extreme soil moisture droughts for Europe under climate change. *Science of The Total Environment*. 660, 1245-1255.
- [7] Padgham, J., Jabbour, J., Dietrich, K., 2015. Managing change and building resilience: A Multi-stressor analysis of urban and peri-urban agriculture in Africa and Asia. *Urban Climate*. 12, 183-204. DOI: <https://doi.org/10.1016/j.uclim.2015.04.003>
- [8] Allison I., N.L., Bindoff, R.A., Bindenschadler, P.M., et al., 2009. The Copenhagen Diagnosis. Updating the World on the Latest Climate Science. The University of New South Wales Climate Change Research Centre (CCRC), Sydney, Australia. pp. 60.
- [9] Hartmann, D.L., Klein Tank, A.M.G., Rusticucci, M., et al., 2013. Observations: Atmosphere and surface.

- T.F. Stocker, D. Qin, G.-K. Plattner, M. Tignor, S. K. Allen, J. Boschung, A. Nauels, Y. Xia, V. Bex & P. M. Midgley (Eds.), *Climate Change 2013: The Physical Science Basis. Contribution of Working Group I to the Fifth Assessment Report of the Intergovernmental Panel on Climate Change*. Cambridge, United Kingdom and New York, NY, USA: Cambridge University Press.
- [10] World Bank, 2009. *World Development Report 2010. Development and Climate Change*. World Bank Washington.
- [11] Parry, M.N., Arnell, P., Berry, D., et al., 2009. *Assessing the Costs of Adaptation to Climate Change: A review of the UNFCCC and Other Recent Estimates*. London: International Institute for Environment and Development and the Grantham Institute for Climate Change, Imperial College. pp. 111.
- [12] World Bank, 2010. *Economics of Adaptation to Climate Change: Synthesis Report*. Washington DC. pp. 100. <https://worldbank.org>.
- [13] Adjei, V., Kyerematen, R., 2018. *Impacts of Changing Climate on Maize Production in the Transitional Zone of Ghana*. *American Journal of Climate Change*. 7, 463-476.  
DOI: <https://doi.org/10.4236/ajcc.2018.73028>
- [14] Haensler, A., Saeed, F., Jacob, D., 2013. *Assessing the robustness of projected precipitation changes over central Africa on the basis of a multitude of global and regional climate projections*. *Climatic Change*. 121(2), 349-363.  
DOI: <https://doi.org/10.1007/s10584-013-0863-8>
- [15] Baidu, M., Amekudzi, L.K., Aryee, J.N.A., et al., 2017. *Assessment of Long-Term Spatio-Temporal Rainfall Variability over Ghana Using Wavelet Analysis*. (Retrieved on 20th June, 2022). [www.mdpi.com/journal/climate](http://www.mdpi.com/journal/climate).
- [16] Ghana Statistical Service, 2021. *2021 Population and Housing Census Publications. General Report Volume 3C*.
- [17] Amekudzi, L.K., Yamba, E.I., Preko, K., et al., 2015. *Variabilities in rainfall onset, cessation and length of rainy season for the various Agro-Ecological Zones of Ghana*. *Climate*. 3, 416-434.
- [18] Barclays and Met Office, 2009. *Storm Shelter: managing climate risks in Africa*. Crown Copyright. UK Met Office. Exeter. UK.
- [19] USDA., 2008. *The Effects of Climate Change on Agriculture, Land Resources, Water Resources, and Biodiversity in the United States*. U.S. Climate Change Science Program Synthesis and Assessment Product 4.3. <http://www.climatechange.gov>.
- [20] Milly, P.C.D., Dunne, K.A., Vecchia, A.V., 2005. *Global pattern of trends in streamflow and water availability in a changing climate*. *Nature*. 438, 347-350.
- [21] Christensen, N., Lettenmaier, D.P., 2007. *A multi-model ensemble approach to assessment of climate change impacts on the hydrology and water resources of the Colorado River basin*. *Hydrology and Earth System Sciences*. 11, 1417-1434.
- [22] Food and Agriculture Organisation, 2011. *Climate Change, Water and Food Security Rome*. FAO water reports. Retrieve from <https://www.statsghana.gov.gh>.
- [23] Adams, R.M., Peck, D.E., 2018. *Effects of Climate Change on Water Resources*. *The magazine of food, farm, and resource issues*. Retrieve from <https://www.choicesmagazine.org>.
- [24] Morrison, J., Morikawa, M., Murphy, M., et al., 2009. *Water Scarcity & Climate Change: Growing Risks for Businesses & Investors*. [www.pacinst.org](http://www.pacinst.org).
- [25] Gleick, P., 2007. *The World's Water 2006-2007: A Biennial Report on Freshwater Resources*. Retrieve from <https://link.springer.com>.
- [26] National Center for Atmospheric Research, 2005. *Drought's Growing Reach: NCAR Study Points to Global Warming as Key Factor*. The University Corporation for Atmospheric Research. [http://www.ucar.edu/news/releases/2005/drought\\_research.shtml](http://www.ucar.edu/news/releases/2005/drought_research.shtml).
- [27] Barnett, T.P., Pierce, D.W., 2008. *When will Lake Mead go dry?* *Water Resources Research*, 44, Scripps Institution of Oceanography, University of California, San Diego. <http://scrippsnews.ucsd.edu/Releases/?releaseID=876>.
- [28] Koutroulis, A.G., Papadimitriou, L.V., Grillakis, M.G., et al., 2018. *Freshwater vulnerability under high end climate change. A pan-European assessment*. *Science of the Total Environment*. 613-614, 271-286.
- [29] Adiku, S., Mawunya, F., Jones, J., et al., 2007. *Can ENSO help in agricultural decision-making in Ghana?* In *Climate Prediction and Agriculture*. Springer: Berlin/Heidelberg, Germany. pp. 205-212.
- [30] Sultan, B., Janicot, S., 2000. *Abrupt shift of the ITCZ over West Africa and intra-seasonal variability*. *Geophysical Research Letters*. 27, 3353-3356.
- [31] Mawunya, F., Adiku, S., Laryea, K., et al., 2011. *Characterisation of seasonal rainfall for cropping schedules*. *West African Journal of Applied Ecology*. 19, 108-118.
- [32] Paeth, H., Hense, A., 2004. *SST versus climate change signals in West African rainfall: 20th-century variations and future projections*. *Climatic Change*.

- 65, 179-208.
- [33] Owusu, K., Waylen, P., Qiu, Y., 2008. Changing rainfall inputs in the Volta basin: Implications for water sharing in Ghana. *GeoJournal*. 71, 201-210.
- [34] Yorke, C., Omotosho, J., 2010. Rainfall variability in Ghana during 1961-2005. *Journal of the Ghana Science Association*. 12.  
DOI: <https://doi.org/10.4314/jgsa.v12i1.56813>
- [35] Lee, T., McPhaden, M.J., 2000. Increasing intensity of El Niño in the central-equatorial Pacific. *Geophysical Research Letters*. 37.  
DOI: <https://doi.org/10.1029/2010GL044007>
- [36] Zhang, Q., Holmgren, K., Sundqvist, H., 2015. Decadal rainfall dipole oscillation over southern Africa modulated by variation of austral summer land-sea contrast along the East Coast of Africa. *Journal of the Atmospheric Sciences*. 72, 1827-1836.
- [37] Janicot, S., Harzallah, A., Fontaine, B., et al., 1998. West African monsoon dynamics and eastern equatorial Atlantic and Pacific SST anomalies (1970-1988). *Journal of Climate*. 11, 1874-1882.
- [38] Rowell, D.P., 2001. Teleconnections between the tropical Pacific and the Sahel. *Quarterly Journal of the Royal Meteorological*. 127, 1683-1706.
- [39] Matthews, A.J., 2004. Intra-seasonal variability over tropical Africa during northern summer. *Journal of Climate*. 17, 2427-2440.
- [40] Ekwezu, C.S., Nnamchi, H.C., Phil-Eze, P.O., 2017. Projected Changes in Mean Annual Rainfall Pattern over West Africa during the Twenty First Century. *Pakistan Journal of Meteorology*. [www.pmd.gov.pk](http://www.pmd.gov.pk) (Assessed on 12th June, 2014).
- [41] Cooper, P.J.M., Dimes, J., Rao, K.P.C., et al., 2008. Coping better with current climatic variability in the rain-fed farming systems of sub-Saharan Africa: An essential first step in adapting to future climate change? *Agriculture, Ecosystems and Environment*. 126, 24-35.
- [42] Sultan, B., Janicot, S., 2003. The West African monsoon dynamics. Part II: The “preonset” and “onset” of the summer monsoon. *Journal of Climate*. 16, 3407-3427.
- [43] IPCC, 2007. *Climate Change 2007, the Fourth IPCC Assessment Report*. Cambridge University Press. Retrieve from <http://www.ipcc.ch>.
- [44] Asante, F.A., Amuakwa-Mensah, F., 2015. *Climate Change and Variability in Ghana: Stocktaking*. Climate journal. University of Ghana, Legon, Ghana. Retrieved on 24th February, 2020 from [www.mdpi.com/journal/climate](http://www.mdpi.com/journal/climate).
- [45] Owusu, K., Waylen, P., Qiu, Y., 2008. Changing rainfall inputs in the Volta basin: implications for water sharing in Ghana. *GeoJournal*. 71, 201-210.
- [46] Adjei, V., Kwantwi, B.L., 2019. Maize and Cashew Farming in the Face of Climate Change Variability in the Transitional Zone of Ghana: A Case Study of Nkoranza South Municipality. *American Journal of Environmental Sciences, USA*.  
DOI: <https://doi.org/10.3844/ajessp>
- [47] Adjei, V., Mawusi, A.A., 2020. Cashew Production as a Climate Change Adaptation and Mitigation Tool for Agriculture. *Advances in Earth and Environmental Science*. [www.unisciencepub.com](http://www.unisciencepub.com).
- [48] Dietz, T., Millar, D., Dittoh, S., et al., 2004. *Climate and Livelihood Change in North East Ghana*. A.J. Dietz, R. Ruben & A. Verhagen, (eds.), *The Impact of Climate Change on Drylands, with a Focus on West Africa*. Dordrecht/Boston/London: Kluwer Academic Publishers. Environment and Policy Series. 39, 149-172.
- [49] Adiku, S.G.K., Yangyuo, M., MacCarthy, D.S., 2013. Assessing the Potential Impact of Climate Change on Maize Production in Two Farming Zones of Ghana Using the CERES-Maize Model. *Ghana Journal policy 5 Climate Change in Ghana: Impacts on Agriculture and the Policy Implications*. Retrieved on 15th December, 2015 from [www.ieagh.org](http://www.ieagh.org).
- [50] Codjoe, S.N.A., Nabie, V.A., 2014. Climate Change and Cerebrospinal Meningitis in the Ghana Belt. *International Journal of Environmental Research and Public Health*. pp. 6923-6939.
- [51] Akudugu, M.A., Dittoh, S., Mahama, E.S., 2012. The implications of climate change on food security and rural livelihoods: experiences from Northern Ghana. *Journal of Environment & Earth Science*. 2(3), 21-29.
- [52] GFDRR., 2011. *Climate Risk and Adaptation Country Profile*. [www.worldbank.org](http://www.worldbank.org) (Assessed on 10th February, 2022).
- [53] Asumadu-Sarkodie, S., Owusu, P.A., Jayaweera, H.M.P.C., 2015. Flood risk management in Ghana: A case study in Accra. *Pelagia Research Library Advances in Applied Science Research*. pp. 196-206.
- [54] Cameron, C., 2011. *Climate change finance and aid effectiveness: Ghana Case Study*. OECD. <http://www.oecd.org/dac/environmentdevelopment/48458430.pdf>.
- [55] Akon-Yamga, G., Boadu, P., Obiri, B.D., et al., 2011. *Agricultural Innovations for Climate Change Adaptation and Food Security in Africa: The Cases of Ghana and The Gambia*. African Technology Policy Studies Network. <http://www.atpsnet.org/Files/rps11.pdf>.

- [56] Ghana Water Resources Commission, 2012. WRC. Pra River Basin - Integrated Water Resources Management Plan. Retrieve from <http://www.washghana.net>.
- [57] USDA, 2008. The Effects of Climate Change on Agriculture, Land Resources, Water Resources, and Biodiversity in the United States. U.S. Climate Change Science Program Synthesis and Assessment Product 4.3. <http://www.climatechange.gov>.
- [58] Antwi B.B., 2014. Galamsey As A Livelihood Approach In Ghana: From a Poverty Reduction Strategy to a Money-Spinning Business, Centre for Development and the Environment, University of Oslo.
- [59] Bekoe, E.O., Logah, F.Y., 2013. The Impact of Droughts and Climate Change on Electricity Generation in Ghana. *Environmental Sciences*. 1(1), 13–24.
- [60] Awotwi, A., Anornu, G.K., Quaye-Ballard, J., et al., 2017. Analysis of Climate and Anthropogenic Impacts on Runoff in the Lower Pra River Basin of Ghana. *Heliyon*. 3.  
DOI: <https://doi.org/10.1016/j.heliyon.2017.e00477>
- [61] Government of Ghana, 2007. Ghana National Water policy.
- [62] Fatawu, N.A., Allan, A., 2014. Managing the impacts of mining on Ghana's water resources from a legal perspective. *Journal of Energy and Natural Resource*. 156-165. <https://www.smenticscholar.org>.
- [63] Obuobie, E., Barry, B., 2012. Ghana. Groundwater Availability and Use in Sub-Saharan Africa: A Review of 15 Countries; Pavelic, P., Giordano, M., Keraita, B., Ramesh, V., Rao, T., Eds. International Water Management Institute: Colombo, Sri Lanka.
- [64] UPGro-African Groundwater, Ghana, 2020. UPGro - African Groundwater 2020.
- [65] Gyampoh, A.B., Idinoba, M., Amisah, S., 2014. Water Scarcity under a Changing Climate in Ghana: Options for livelihoods adaptation. *Society for International Development*. 1011-6370/08. <https://www.researchgate.net/publication/5219960>.
- [66] Minerals Commission, 2015. Artisanal and Small-scale Mining (ASM) framework. <https://www.mofep.gov.gh/sites/default/files/reports/economic/ASM.FRAMEWORK>.
- [67] Alhassan, I.A., 2014. Galamsey and the Making of a Deep State in Ghana: Implications for National Security and Development. *Research on Humanities and Social Sciences*. 2224-5766.
- [68] Baah-Ennumh, T.Y., 2010. Sustaining livelihoods in artisanal small-scale mining communities in the Tarkwa-Nsuaem Municipality (Unpublished doctoral dissertation). Kwame University of Science and Technology.
- [69] Hilson, G., 2006. Abatement of mercury pollution in the small-scale gold mining industry: Restructuring the policy and research agendas. *Science of the Total Environment*. 362(1), 1-14.
- [70] Amankwah, E., 2013. Impact of illegal mining on water resources for domestic and irrigation purposes. *ARNP Journal of Earth Sciences*. 2(3), 117-121.
- [71] Nartey, V.K., Klake, R.K., Hayford, E.K., et al., 2011. Assessment of mercury pollution in rivers and streams around artisanal gold mining areas of the Birim North District of Ghana. *Journal of Environmental Protection*. 2(9), 1227-1239.
- [72] Clifford, M.J., 2017. Assessing releases of mercury from small-scale gold mining sites in Ghana. *Extractive Industries and Society*. 4(3), 497-505.
- [73] Yeleliere, E., Cobbina, S.J., Duwiejuah, A.B., 2018. Review of Ghana's Water Resources: The Quality and Management with Particular Focus on Freshwater Resources. *Applied Water Science*. 8(3), 93.  
DOI: <https://doi.org/10.1007/s13201-018-0736-4>
- [74] Adombire, M., Adjewodah, P., Abrahams, R., 2013. Business as Usual (BAU) Scenario Information and Analysis Covering the Pra and Kakum River Basins. Nature Conservation Research Centre. Retrieve from <http://www.forest.treds.org>.
- [75] Gampson, E.K., Nartey, V.K., Golow, A.A., et al., 2014. Hydrochemical. Study of Water Collected at a Section of the Lower Volta River (Akuse to Sogakope Area), Ghana. *Applied Water Science*. 4, 129-143.
- [76] Hilson, G., 2002. Harvesting mineral riches: 1000 years of gold mining in Ghana. *Resource Policy*. 28, 13-26. <https://onlinelibrary.wiley.com>.
- [77] Duncan, A.E., 2020. The Dangerous Couple: Illegal Mining and Water Pollution—A Case Study in Fena River in the Ashanti Region of Ghana.  
DOI: <https://doi.org/10.1155/2020/2378560>
- [78] Aryee, B.N.A., Ntibery, B.K., Atorkui, E., 2003. Trends in the small-scale mining of precious minerals in Ghana: a perspective on its environmental impact. *Journal of Cleaner Production*. 11(2), 131-140.
- [79] Kyeremeh, K., 2017. Galamsey Menace: The failure of mining governance system. <https://ghanatalksbusiness.com/2017/03/galamsey-menace-failure-mining-governance-system>.
- [80] Clifford, M.J., 2017. Assessing releases of mercury from small-scale gold mining sites in Ghana. *Extractive Industries and Society*. 4(3), 497-505.
- [81] Duncan, A.E., de Vries, N., Nyarko, K.B., 2018. Assessment of Heavy Metal Pollution in the Main Pra

- River and Its Tributaries in the Pra Basin of Ghana. *Environmental Nanotechnology, Monitoring & Management*. 10, 264-271.  
DOI: <https://doi.org/10.1016/j.enmm.2018.06.003>
- [82] Hilson, G., 2001. A contextual review of the Ghanaian small-scale mining industry. *Mining, Minerals and Sustainable Development*. 76, 1-29.
- [83] Nartey, V.K., Klake, R.K., Hayford, E.K., et al., 2011. Assessment of mercury pollution in rivers and streams around artisanal gold mining areas of the Birim North District of Ghana. *Journal of Environmental Protection*. 2(9), 1227-1239.
- [84] Ahoulé, D.G., Lalanne, F., Mendret, J., et al., 2015. Arsenic in African Waters: A Review. *Water Air & Soil Pollution*. 226(302).  
DOI: <https://doi.org/10.1007/s11270-015-2558-4>
- [85] Donkor, A.K., Bonzongo, J.C.J., Nartey, V.K., et al., 2015. Heavy Metals in Sediments of the Gold Mining Impacted Pra River Basin, Ghana, West Africa. *Soil & Sediment Contamination*. 14, 479-503.  
DOI: <https://doi.org/10.1080/15320380500263675>
- [86] Carr, G.M., Neary, J.P., 2008. Water Quality for Ecosystem and Human Health, UNEP, Nairobi, Kenya. <https://www.scrip.org>.
- [87] United Nations Agency International Development. <https://www.undp.org>.

ARTICLE

# To the Question of the Assessment of Ecological Comfort of the Climate

Elena S. Andreeva<sup>1\*</sup>  Sergey S. Andreev<sup>2</sup> Anna A. Parshina<sup>2</sup>

1. Department of Life Safety and Environmental Protection, Don State Technical University, Rostov-on-Don, Russia

2. Rostov Institute of Entrepreneur Protection, Rostov-on-Don, Russia

---

ARTICLE INFO

*Article history*

Received: 28 June 2022

Revised: 21 July 2022

Accepted: 22 July 2022

Published Online: 23 August 2022

*Keywords:*

Bioclimatic indicators

Ecological comfort of the climate

Self-purification of the atmosphere

Pathogenicity of meteorological conditions

---

ABSTRACT

The article is devoted to the discussion of the advantages of assessing the environmental comfort of the climate, based on the natural features of the climate and the bioclimatic conditions of the territory. The study assessed the ecological comfort of the climate in the city of Taganrog on the basis of the developed original sequence of performing three stages of assessing the totality of bioclimatic indicators with the final calculation of the values of the integral indicator of the bioclimatic comfort of the climate. The results of the assessment showed, according to the average long-term climatic data, the presence of sub-comfortable climates with a tendency to transition to comfortable climate conditions in the warm period of the year. The cold season was distinguished by uncomfortable conditions according to long-term average climatic data. Modeling calculations of the possible risk to the health of city residents in the presence of concentrations of suspended solids in the surface air layer, together with carbon monoxide, exceeding the maximum one-time values by more than 7 times, showed that the development of possible resorptive or carcinogenic effects in these circumstances will occur in 1/3 the population of the city. The prospects for the assessment of the ecological comfort of the climate, which allow in the future to adequately calculate the magnitude of environmental risks to public health caused by pollution of the surface air layer, are shown.

## 1. Introduction

According to the authors of the study, at present, an assessment of the ecological state of a territory or a specific point object necessarily includes an analysis of all the components of the sources of pollutant release, as well as the pollutants themselves in terms of their environmental

(toxicological, carcinogenic, mutagenic) hazard. However, the natural characteristics of the territory, mainly its climatic features, which make not only no less, but often even the greatest contribution to the ecological state of the area that is formed in the complex, taking into account anthropogenic activity, remain without attention. In this

---

\*Corresponding Author:

Elena S. Andreeva,

Department of Life Safety and Environmental Protection, Don State Technical University, Rostov-on-Don, Russia;

Email: [meteo0717@yandex.ru](mailto:meteo0717@yandex.ru)

DOI: <https://doi.org/10.30564/jasr.v5i3.4845>

Copyright © 2022 by the author(s). Published by Bilingual Publishing Co. This is an open access article under the Creative Commons Attribution-NonCommercial 4.0 International (CC BY-NC 4.0) License. (<https://creativecommons.org/licenses/by-nc/4.0/>).

connection, as the analysis of a number of scientific studies shows, the environmental assessment carried out is not always objective and adequate to the conditions under consideration. In this regard, in order to eliminate the contradictions described above, in 2010 an approach was proposed based on the concept of ecological climate comfort, which allows taking into account the natural component of climatic and bioclimatic conditions and features of the study area [1].

As is known, in order to assess the biological impact of climatic conditions on human health and the state of ecological systems, already in the middle of the 20th century, a number of bioclimatic indicators were first developed and applied, which, among others, include indicators that allow assessing the total impact of groups of meteorological parameters, such as air temperature, air humidity, surface wind speed, atmospheric pressure, as well as the number of days with fogs, wind speeds of more than 6 m/s, with precipitation or lack of surface wind (calm), etc.

The concept and methodology for assessing the environmental comfort of the climate makes it possible to comprehensively take into account the environmental impact of not only bioclimate parameters, but also the level of pollution of the surface air layer of the study area [1]. In particular, based on the analysis and ranking of bioclimatic indicators in, it was found that the most informative bioclimatic indices (with an anthropocentric approach, if we focus on the impact on public health) include the following: BAP - biologically active temperature; ET - equivalent effective temperature; REET - radiation equivalent effective temperature; QS is the human heat balance; I - index of pathogenicity of the meteorological situation; KM - climatic potential of self-purification of the atmosphere [2].

Within the framework of the developed methodology for assessing the environmental comfort of the climate, it was proposed not only to carry out a phased assessment of all groups of the above bioclimatic indicators, but as a result, to calculate and analyze the value of the integral indicator of environmental comfort of the climate developed, IPBC, which allows comprehensively taking into account both natural climatic (bioclimatic) features of the study area, as well as parameters characterizing the level of pollution of its surface air layer in the first approximation [1].

## 2. Materials and Methods

To conduct this study, the authors proceeded from the concept of assessing the environmental comfort of the climate, which involves the implementation of a three-stage assessment of the parameters of the bioclimate, as well as the calculation of the integral indicator of the environmen-

tal comfort of the climate [1].

At the same time, at the first stage of the assessment, the thermal effect was considered and such parameters as ET - equivalent effective temperature were calculated; REET - radiation equivalent effective temperature; QS is the human heat balance [1]. In particular, “hard thermal impact of high or low temperatures “discomfort” could be observed at the value of the bioclimatic comfort score equal to “1”; with the value of the bioclimatic comfort score equal to “3”, “moderate thermal effects of high or low temperatures “subcomfort” were diagnosed; finally, with the value of the bioclimatic comfort score equal to “5”, comfortable thermal effects of high or low temperatures “comfort” were diagnosed.

At the second stage, the degree of pathogenicity of weather conditions (I) was assessed in the work, that is, the negative impact of a complex of meteorological conditions (including the value of surface atmospheric pressure, heliogeophysical factors, cloudiness, sudden changes in air temperature and atmospheric pressure per day). The following interpretation of the obtained results was accepted: “a high degree of pathogenicity of meteorological conditions “discomfort” could be observed with the value of the bioclimatic comfort score equal to “1”; with the value of the bioclimatic comfort score equal to “3”, the “medium degree of pathogenicity of meteorological conditions “subcomfort” was diagnosed; finally, with the value of the bioclimatic comfort score equal to “5”, a “low degree of pathogenicity of meteorological conditions “comfort” was diagnosed.

The third stage involved the evaluation of the potential for self-purification of the atmosphere (km). With the value of the bioclimatic comfort score equal to “1”, a low potential for self-purification of the atmosphere, “discomfort” was observed; with the value of the bioclimatic comfort score equal to “3”, the “average potential for self-purification of the atmosphere” subcomfort was diagnosed; finally, with the value of the bioclimatic comfort score equal to “5”, high potential for self-purification of the atmosphere “comfort” was diagnosed.

The integral indicator of bioclimatic comfort is determined as the sum of bioclimatic assessment scores obtained at three stages, according to the following formula:

$$IBK = \frac{\sum Ki * B BK}{\sum Ki} \tag{1}$$

in formula

<i>IBK</i>	–	integral indicator of bioclimatic comfort
<i>Ki</i>	–	informative coefficient
<i>B BK</i>	–	bioclimatic assessment score
<i>i</i>	–	bioclimatic index

It is important to note that the developed integral indicator <sup>[1]</sup>, with the help of which an integral assessment is carried out, including intermediate 3 stages, is universal for any study area and makes it possible to identify such characteristics of climatic comfort as: comfort; discomfort and sub-comfort. This takes into account the important influence of natural, natural meteorological factors on health and life, as well as the possibility of reducing the pollution of the troposphere due to its potential for self-purification. Interpretation of the given integral index of IPBC practically repeats those described above, that is: with the value of the integral score of bioclimatic comfort equal to “1”, “discomfort” is observed; with the value of the integral score of bioclimatic comfort equal to “3”, “subcomfort” is diagnosed; finally, with the value of the bioclimatic comfort score equal to “5”, the “comfort” of the environmental conditions of the climate is noted.

Reference data on the climate of the south of the European part of Russia, as well as a number of synoptic maps that are in the public domain, were used for the calculations.

### 3. Results

The assessment of the integral indicator of bioclimatic comfort on the example of the city of Taganrog, Rostov Region, showed, on the whole, quite comfortable environmental conditions of the climate (higher than “subcomfort”). So, for the warm season, the calculated value of the integral indicator of bioclimatic comfort within the city of Taganrog was 4.4 points, that is, according to the average long-term climatic data, a transition from “subcomfort” to “comfort” was established, which is higher than the values of the considered integral indicator of bioclimatic comfort for the neighboring city of Rostov-on-Don (IPBK values were 3.2 points, “subcomfort”). The cold season for both the city of Taganrog and Rostov-on-Don was characterized by uncomfortable conditions, not exceeding the

IPBC value of 1.2 - 1.0 points, respectively (Table 1).

From the data in the Table 1, it can be seen that for the city of Taganrog, the climatic conditions, especially in the warm season of the year, are distinguished by environmental comfort. In order to understand this situation, consider the geographical characteristics of the city’s environs. So, as you know, the city is located in the north-eastern part of the Miusky Peninsula, which juts out into the Sea of Azov. In the east, the territory of the city is limited by the Sambek River, and in the southeast and south it is washed by the waters of the Taganrog Bay of the Sea of Azov. The western border of the city runs along the Mius River, which ends with the Mius Estuary, connecting with the Sea of Azov 36 km from it. In fact, the city is located within the triangular cape of the Miusky Peninsula, surrounded by water from almost all sides of the shallow and well-heated Sea of Azov or its Taganrog Bay, as well as the Miusky Estuary.

It seems that these circumstances not only have a warming, but also a moisturizing effect on the climate of the adjacent territory. In addition, the proximity to the system of the Azov-Black Sea basin determines the intensive dispersion of impurities, including anthropogenic impurities in the lower air layer of the urban environment of Taganrog, since different environments (land-sea) with different physical characteristics cause heterogeneous atmospheric pressure fields and, as a result, significant changes in the values of the horizontal baric gradient. Anthropogenically caused impurities in the surface layer and the breeze circulation that is formed in this area have a very favorable effect on the dispersion. In addition to the coefficient of self-purification of the atmosphere, KM, within the framework of this study, the meteorological indicator of atmospheric pollution, MPA, developed in was also calculated and evaluated, the values of which recently also steadily show the predominance of dispersion conditions over the accumulation of impurities in the surface layer of the atmosphere <sup>[3-7]</sup>.

**Table 1.** Comparative analysis of the indicators of the integral assessment of the environmental comfort of the climate for the cities of Taganrog and Rostov-on-Don

No.	Station	I stage of bioclimatic assessment				II stage	III stage	Meaning I BK, points
		BAT	REET	ET	Qs	I	Km	
<i>warm climate season of the year</i>								
1.	Rostov-on-Don	20.6	19.8	9.4	-0.6	12.4	0.9	3.2
2.	Taganrog	21.2	20.6	10.3	-0.6	9.2	0.4	4.4
<i>cold climatic season of the year</i>								
3.	Rostov-on-Don	5.0	-0.4	-14.9	-1.6	25.9	1.3	1.0
4.	Taganrog	6.1	0.9	-13.3	-1.5	24.7	1.4	1.2

## 4. Discussion

It seems to the authors that the very favorable conditions for the environmental comfort of the climate of the city of Taganrog in the warm season of the year are explained, on the one hand, by a significant warming of the air in the warm season, which, however, is compensated by the moistening and reducing the heat load by the influence of the Sea of Azov. It is the breeze circulation in the warm season that reduces the likelihood of dry days with calm, when an intensive accumulation of impurities in the lower layer is possible. More precipitation falls in July, during the warm season of the year, which also contributes to an increase in the self-purification coefficient of the atmosphere.

The discomfort of winter conditions within the city is explained, apparently, not only by possible breakthroughs of the Arctic air masses both in the rear of the Atlantic cyclones and in the form of spurs of the Arctic High. But, also with an increased probability of calm weather (1/3 of all studied cases of calm weather was observed in winter - in early spring, in the first quarter of the year), which were more often set at night, contributing to the accumulation of impurities in the lower atmosphere. In addition, the minimum amount of precipitation in autumn and winter reduces the self-cleaning ability of the atmosphere within the city.

According to the authors, the results obtained are not only of theoretical significance, expanding the limits of knowledge about the biological aspects of the impact of climate on the human body and its environment, but also of undoubted practical value, making it possible to apply the findings to planning the modes of work and rest of the population. In this regard, it seems very promising to further consider at the next stage of research the role of anthropogenic factors that affect the level of pollution of the surface air layer, since the increase in the optical turbidity of the air layer at a level of 2 m from the surface, as well as the appearance of a number of toxic and carcinogenic substances in the air of the urban environment can cause very significant environmental risks to public health. So, for example, within the framework of this study, an assessment of a possible health risk in the presence of concentrations of suspended solids in the surface air layer together with carbon monoxide exceeding, say, the values of the maximum single maximum permissible concentration by more than 7 times showed that the development of possible resorptive or carcinogenic effects in these circumstances will occur in 1/3 of the population of the city of Taganrog.

## 5. Conclusions

Thus, as a result, of the assessment of the environmen-

tal comfort of the climate, as well as the calculated values of the possible environmental health risk, including carcinogenic health risk, the following results were obtained, which made it possible to formulate the main conclusions of the study:

1) Natural characteristics, among which climatic and bioclimatic features play a leading role, the cities of Taganrog are extremely favorable. The territory of the city is washed by the waters of the warm and shallow Sea of Azov, which has a warming and moisturizing effect, and also determines the specifics of the local circulation of air masses.

2) The assessment of the ecological comfort of the climate in the territory of Taganrog showed, according to the average long-term climatic data, the presence of sub-comfortable climates with a tendency to transition to comfortable climate conditions in the warm period of the year. The cold season was distinguished by uncomfortable conditions according to long-term average climatic data.

3) Modeling calculations of a possible health risk in the event of the presence in the surface air layer of concentrations of suspended solids together with carbon monoxide exceeding, say, the values of the maximum one-time maximum permissible concentration by more than 7 times showed that the development of possible resorptive or carcinogenic effects in the indicated circumstances will occur in 1/3 of the population of the city of Taganrog.

## Author Contributions

All authors of this article took an equal part in writing it: they formulated the idea, carried out calculations, wrote the text, and took care of the design of the article.

## Conflict of Interest

There is no conflict of interest.

## Funding

This research received no external funding.

## References

- [1] Andreev, S., Popova, E., 2015. Estimation of climatic comfort of coastal territory on the example of city of Tuapse. *Bulletin of St. Petersburg University, Series Geology and Geography*. 4, 145-150.
- [2] Golovina, E., Rusanov, V., 1993. Some questions of biometeorology. S.-P. Russian Hydrometeorological Institute. pp. 90.
- [3] Selegey, T., Filonenko, N., Lenkovskaya, T., 2015. On the method for determining the meteorological potential of atmospheric pollution. *Atmospheric and*

- Ocean Optics. 8(8), 725-729.
- [4] Abiye, O., Akinoba, O., Sunmonu, L., et al., 2016. Atmospheric ventilation corridors and coefficients for pollution plume released from an Industrial Facility in Ile-Ife Suburb Nigeria. *African Journal of Environmental Science and Technology*. 10(10), 338-349.  
DOI: <https://dx.doi.org/10.5897/AJEST2016.2128>.
- [5] Gassmann, M., Mazzeo, N., 2000. Air pollution potential: Regional study in Argentina. *Environ man- age*. 25(4), 375-382.  
DOI: <https://doi.org/10.1007/s002679910>
- [6] Viswanadham, D., Santosh, K., 1989. Air pollution potential over South India. *Bondary-Layer Meteorology*. 48(3), 299-313.  
DOI: <https://doi.org/10.1007/BF00158330>
- [7] Yu, M., Cai, X., Xu, C., et al., 2018. A climatological study of air pollution potential in China. *Theoretical and Applied Climatology*. 1-12.  
DOI: <https://doi.org/10.1007/s0070-4-018-2511-8>
- [8] Lewis, D., Mertens, K., Stock, J., 2020. Weekly Economic Index. Retrieved from FRED, Federal Reserve Bank of St. Louis. <https://fred.stlouisfed.org/series/WEI>. (Accessed 26 May 2020).



 **BILINGUAL PUBLISHING CO.**  
Pioneer of Global Academics Since 1984

Tel.: +65 65881289  
E-mail: [contact@bilpublishing.com](mailto:contact@bilpublishing.com)  
Website: [ojs.bilpublishing.com](http://ojs.bilpublishing.com)

2630-5119



03

9 772630 511225